INFORMATION TO USERS

This manuscript has been reproduced from the microfilm master. UMI films the text directly from the original or copy submitted. Thus, some thesis and dissertation copies are in typewriter face, while others may be from any type of computer printer.

The quality of this reproduction is dependent upon the quality of the copy submitted. Broken or indistinct print, colored or poor quality illustrations and photographs, print bleedthrough, substandard margins, and improper alignment can adversely affect reproduction.

In the unlikely event that the author did not send UMI a complete manuscript and there are missing pages, these will be noted. Also, if unauthorized copyright material had to be removed, a note will indicate the deletion.

Oversize materials (e.g., maps, drawings, charts) are reproduced by sectioning the original, beginning at the upper left-hand corner and continuing from left to right in equal sections with small overlaps.

ProQuest Information and Learning
300 North Zeeb Road, Ann Arbor, MI 48106-1346 USA
800-521-0600

UMI®

DISSERTATION

INSIGHTS ON HURRICANE INTENSITY

Submitted by

John Persing

Department of Atmospheric Science

In partial fulfillment of the requirements

for the degree of Doctor of Philosophy

Colorado State University

Fort Collins, Colorado

Summer 2002

ProQuest Information and Learning Company
300 North Zeeb Road
P.O. Box 1346
Ann Arbor, MI 48106-1346

COLORADO STATE UNIVERSITY

May 21, 2002

WE HEREBY RECOMMEND THAT THE DISSERTATION PREPARED UNDER OUR SUPERVISION BY JOHN PERSING ENTITLED INSIGHTS ON HURRICANE INTENSITY BE ACCEPTED AS FULFILLING IN PART REQUIREMENTS FOR THE DEGREE OF DOCTOR OF PHILOSOPHY.

Committee on Graduate Work

Michael Kirby

William M. Gray

Wayne Schubert

Michael T. Montgomery

Adviser

Department Head

ABSTRACT OF DISSERTATION

INSIGHTS ON HURRICANE INTENSITY

The motivation of this thesis is to obtain greater understanding of the controls on hurricane intensity. The results from three different hurricane models are presented: 1) a Geophysical Fluid Dynamics Laboratory Hurricane Prediction System simulation of Hurricane Opal (1995) using a reality-based, three-dimensional representation of the atmosphere; 2) the Emanuel (1995a) highly-simplified, axisymmetric hurricane model; and 3) the Rotunno and Emanuel (1987) axisymmetric, cloud-resolving, nonhydrostatic, grid model.

From the Opal simulation, we conclude that the popularly identified features of the environment of the storm (ocean eddies, trough-interaction, jet entrance regions) are not able to explain the modulations of intensification found in the simulation; although vertical shear is a strong candidate for the eventual weakening of the storm. This points to a thermodynamic interpretation of intensification. The Emanuel (1995a) model was designed to test a hypothesis for largely thermodynamic development of a hurricane. While confirming steady state intensity predictions of the Emanuel (1995b) maximum potential intensity theory (E-MPI) to within 5 meters per second, sensitivities of the model to purely numerical parameters argue against use the of this model as an operational forecast model.

With the Rotunno and Emanuel (1987) model, E-MPI can be greatly exceeded. Since this model should be faithful to many of the approximations of E-MPI theory, the remaining assumptions of E-MPI theory can be considered in turn. The model produces a significant flux of heat from the eye to the eyewall, allowing the modeled eyewall to ascend against a slight static stability, and this behavior is the key violation of E-MPI theory. The stabilization is a measure of the transfer of heat to the eyewall, and by accounting for this second source of heat, an ad hoc modification of E-MPI can explain most of the "superintensity" of the modeled storm.

We provide evidence that this active interaction between the eye and eyewall may operate in real hurricanes from published observations and in more-realistic, three-dimensional simulations of hurricanes. We propose that a new MPI should be developed to include this influence on hurricane intensity.

John Persing
Department of Atmospheric Science
Colorado State University
Fort Collins, Colorado 80523
Summer 2002

ACKNOWLEDGEMENTS

- Michael T. Montgomery for his guidance as advisor and his ability to improvise to my interests.
- Bob Tuleya for supplying data from the GFDL Hurricane Model and his collaboration on that aspect of this research.
- Rich Rotunno for supplying the Rotunno and Emanuel (1987) hurricane model and for valuable discussions clarifying thought and presentation of those results.
- Kerry Emanuel for supplying the Emanuel (1995a) hurricane model and MPI formulation.
- Scott Braun and Hugh Willoughby for use of data to supplement the argument presented in this thesis.
- Bill Gray, Wayne Schubert, and Michael Kirby for serving on my committee and for useful discussions.
- Tom Cram, Janice Enagonio, Paul Reasor, Sam Grandlienard, Parks Camp, Dave Nolan, Rick Taft, and John Fulton for useful discussion and assistance.
- Graeme Stephens, Denis O'Brien, Lance Bosart, John Gyakum, Dave Randall, Matt Eastin, and Scott Hausman for other useful insights.
- For support during various aspects of this research, the Office of Naval Research via Grant N00014-93-1-0456 P00006, the National Science Foundation via Grant ATM-0101781, the National Aeronautics and Space Administration Fourth Convective and Moisture Experiment via Grant NAG5-11140, and Colorado State University.

DEDICATION

Dedicated to my wonderful fiancee, Melissa, and to God, whose glorious creation I am pleased to study.

CONTENTS

LIST OF FIGURES

LIST OF TABLES

Chapter 1

INTRODUCTION

Until recently, improvements in hurricane forecasting have focused primarily on track. The obvious benefit of an accurate track forecast is the selection of proper risk areas for emergency response. Hurricane intensity forecasting in contrast has not improved to the same degree as track (DeMaria and Kaplan 1999). Landsea (1993) showed that over 80% of the destruction in the United States due to tropical systems was due to the small number of very intense systems ($V_{max} > 50$ m s^{-1}). Better intensity forecasting has been identified as a target to improve forecasts of damaging winds of landfalling tropical cyclones (Marks et al. 1998).

The largely axisymmetric nature of tropical storms can be recognized (Simpson 1952): a spiraling inflow of low level air directed toward a small ($\sim$ 60 km diameter), circular convecting "eyewall", often bounding a central eye with suppressed convection and reduced cloudiness. Complementary with such an observation is the non-axisymmetric nature of tropical storms: spiral rain bands, convective asymmetries in the eyewall, asymmetric outflow aloft, mesovortices, and imposed environmental winds. The problem is further complicated noting the large range of spatio-temporal scales that are interacting: an intensely rotating, convecting vortex on the mesoscale ($\sim$ 50 km) with external influences such as winds, moisture, temperature, and surface heterogeneities (including land/sea differences) that affect the storm from the mesoscale to the synoptic scale ($\sim$ 1000 km).

1.1 Known physical influences on hurricane intensity

The existence of hurricanes in tropical waters implicates a role for warm ocean temperatures (Gray 1968) to provide energy to a storm. Empirical relationships between sea surface temperature (SST) and storm intensity have been discovered (Merrill 1988; DeMaria and Kaplan 1994a) and these ideas have been confirmed by theory (more in Section 1.2.1). This points to the necessity of a favorable thermodynamic setting.

The importance of external influences (other than thermodynamics) is evident in the skill that can be added to empirical forecasts (based on multi-linear regression) by adding environmental variables (DeMaria and Kaplan 1999). Chief among these is vertical shear, whose hypothesized influence has ranged from the ventilation of the storm's upper-level warm core (leading to a rise in surface pressure; Gray 1968) to the induction of convective asymmetries in the eyewall that are followed by asymmetries in the upper level potential vorticity and equivalent potential temperature fields (Frank and Ritchie 2001). Ultimately, though, large vertical shear is seen to be a negative influence on intensity.

Molinari et al. (1998) argued that a superposition of an upper-level potential vorticity (PV) anomaly of small horizontal scale over the center of a nascent tropical cyclone spurred the initial intensification in Tropical Storm Danny (1985). Molinari and Vollaro (1990) diagnosed the approach of eddy angular momentum flux toward the center of Hurricane Elena (1985) and used Eliassen's (1951) balanced vortex model to show how such eddy fluxes can place the upper troposphere out of balance and induce a preference for ascent near the center of the developing hurricane. Wu and Cheng (1999) suggested the importance of eddy angular momentum fluxes, but showed in their examination of Typhoons Flo (1990) and Gene (1990) in the Western Pacific that the upper-level PV features did not get close enough to the storm to promote a strong superposition interaction.

Motivated by the observational analysis of Bosart and Bartlo (1991), Montgomery and Farrell (1993) showed how an interaction with an upper-level trough of a type often associated with subtropical situations can lead to the genesis of tropical storms by acting upon a column of air with an approximately moist neutral profile. Using a dataset enhanced with satellite-derived winds, the recent work of Bosart et al (2000) (hereafter, B00) has shown the occurrence of divergence aloft associated with a jet entrance region coinciding with rapid intensification episodes in Hurricane Opal (Atlantic basin, 1995). Also noted in B00 was the influence of a warm ocean eddy in the Gulf of Mexico in the intensification of Hurricane Opal. It was found in B00 that the eddy flux convergences aloft are too far away to explain the axisymmetric outflow at upper levels. By correlating observed divergence with episodes of deep convection (inferred from satellite imagery), B00 suggested that the divergence aloft (attributed to the jet entrance region) spurred mesoscale convective events in the vicinity of Opal, which then led to intensification of the storm, perhaps augmented by either a vorticity redistribution process (Montgomery and Kallenbach 1997; Montgomery and

Enagonio 1998) or through exchanges of angular momentum modified by convection (Krishnamurti et al. 1998).

In addition to these macroscale processes, microscale influences are known to influence hurricane intensity. Oceanic responses to the presence of the hurricane are imperfectly modeled at this time. One can consider the possible impacts of ocean spray on enthalpy exchange (Fairall et al., 1994; Andreas and Emanuel 2001) and modification of the near-surface ocean heat content by wind-induced mixing of the ocean (Shay et al 1998; Bender and Ginis, 2000; Jacob et al 2000). While these oceanic effects are important, we believe that the atmospheric controls are still not well-enough understood, and thus the atmosphere is the focus of our efforts in this thesis.

1.2 Tools for understanding

1.2.1 Maximum intensity principles

Among many possible tools for hurricane intensity forecasting is to determine the maximum possible intensity of a storm for given atmospheric and oceanic conditions. It is now customary in the hurricane community to call this intensity the maximum potential intensity (MPI). If an MPI principle can be found, then the manifold of possible intensities of the hurricane can be constrained. Camp (1999) provides an in-depth summary of all the known approaches for constructing an MPI theory.

As implied above, empirical MPI's (DeMaria and Kaplan 1994a; Merrill 1988) have been discovered. It is important to first note that the difference between currently observed storm intensity and the empirical MPI is the leading predictor in DeMaria and Kaplan's multi-linear prediction scheme (DeMaria and Kaplan 1999). In order to be useful, a theoretical MPI principle must bear some resemblance to the result of this empirical MPI. An underestimate by theory of any historical storm means that theory is deficient. A gross overestimate by theory technically satisfies the objective of presenting a maximum but is hardly useful. Optimistically, though, such an overestimate presents an opportunity to expose missing physics in the theory that nature is eager to activate to limit hurricane intensity (Camp and Montgomery 2001).

One theoretical approach, first investigated by Miller (1958) and extended recently by Holland (1997) considers the reduction of surface pressure available in the vertical profile of the storm due to warming by moist adiabatic ascent and dry adiabatic descent, which is strongly tied to

the convective available potential energy (CAPE) of the environment. Camp and Montgomery (2001) argued for only a minor role for CAPE in determining the maximum intensity, based on the findings of Rotunno and Emanuel (1987). Camp and Montgomery (2001) also found Holland (1997) to grossly overestimate historical storm intensities, so it fails to provide a useful MPI. The other accepted approach is that first introduced in Emanuel (1986) (which is similar to the approach of Kleinschmidt 1951) employing a frictional boundary layer beneath a conditionally neutral outflow layer. Within this view, the energy for the storm comes from enhanced sea-to-air exchanges of enthalpy in the hurricane boundary layer due to enhanced wind speeds. The Emanuel (1986) theory and subsequent modifications (improved eye parameterization, Emanuel 1995b; inclusion of dissipational heating, Bister and Emanuel 1998) will be referred to here simply as E-MPI. Camp and Montgomery (2001) argue that "[E-MPI] is the closest to providing a useful calculation of maximum intensity."

E-MPI has been tested against tropical cyclone observations in the North Atlantic and western North Pacific basins (Emanuel, 2000), where the MPI was only rarely exceeded by observations and it is suggested that the number of storms that reach their MPI is small. While such an analysis strictly speaking cannot "prove" the worth of the energetically-based MPI theory, it is certainly a necessary condition. Because of these successes, E-MPI theory has gained much acceptance in the community (B00; AMS Council 2000; Bengtsson 2001) and can be considered a paradigm.

Even within the maximum intensity framework, the instantaneous intensity of observed tropical cyclones is uniformly distributed between some minimum and an empirical maximum intensity (DeMaria and Kaplan 1994a; Emanuel 2000). This suggests that it is important to understand the life-cycle of tropical cyclones and the influences that act to uniformly distribute storm intensity between those limits.

While there can be much value in an MPI theory, one should note possible limitations of any energetically-based limit. As an example, it has been noted that a simple energetic argument based on latent heat release used to describe the intensity of tornadoes often underestimates the wind speeds in observed tornadoes by roughly half (Bluestein et al., 1993). Fiedler (1994) used an axisymmetric model to describe two processes for exceeding this limit: a supercritical end-wall vortex and a drowned vortex jump. The end-wall vortex is basically an extension of the frictional boundary layer up the axis of rotation. It exists when the inflow (and up-flow) is accelerated

to the point that axial, compensating subsidence from aloft is not allowed to reach the surface; rather a transition from supercritical to subcritical flow aloft marks the interface between rising and subsiding air. The drowned vortex jump occurs due to an unbalanced "overshoot" in the surface inflow layer allowing parcels to achieve a much smaller radius with only slight reduction in circulation. The results were extended by Fielder (1998) to three dimensions showing the role of transient axial flow to boost the pressure deficit associated with suction vortices (Fujita 1971). In simple terms, vortex dynamics allow the system to exceed simple energetic limits.

1.2.2 Numerical modeling

The hurricane presents interactions from the convecting scale ($\sim$ 5 km) to the mesoscale ($\sim$ 50 km) to the broader synoptic scale ($\sim$ 1000 km). This represents a computational challenge that is gradually falling to improvements in computer technology.

There are three basic modeling schools for dealing with such a large computational problem: 1) axisymmetric simulation, 2) statistical prediction, and 3) three-dimensional simulation.

- Early efforts in modeling tropical storms took advantage of the reduced dimensionality of axisymmetry to propose conceptually simplified models small enough to integrate on extant computers (e.g., Ooyama 1969). The successes of this approach lead to the first complete representations of the intensification cycle of a hurricane that appeared realistic.

- Statistical approaches (e.g., DeMaria and Kaplan 1994b) based on observable large scale parameters and state of the tropical cyclone implicitly assume a simplified, axisymmetric description of both the storm and the environment. The practical use and success of such techniques at forecast offices (DeMaria and Kaplan 1999) suggest that the simplified description of the storm/environment system is to some degree correct. The success of the technique, though, is only partial, therefore the simplified description of the hurricane and the abstraction of the storm physics implied through the statistical reduction technique is incomplete.

- Application of fully, three-dimensional mesoscale models to the hurricane problem began with (Kurihara and Tuleya 1974), a modern version of which has been applied with some success (Kurihara et al. 1995, 1998) in an operational setting to hurricane forecasting. This approach

permits many of the asymmetric features noted in Section 1.1, subject to the constraints of model resolution and the representation of convection. Higher resolution modeling studies have also been performed (e.g., Zhang et al. 2000; Chen and Yau 2001; Braun 2002), although not yet in an operational setting. These efforts encounter the problem of specifying an initialization for the model, since the hurricane vortex cannot presently be observed completely enough to populate the finely-scaled grid mesh that new computer capabilities allow with all the asymmetries present in the observed storm.

1.2.3 Balanced models

An additional tool for understanding hurricane intensity is the use of balanced models to diagnose aspects of storm evolution. Many of the modeling approaches of Section 1.2.2 invoke varying degrees of balance, often for the very practical objective of reducing the number of variables and equations needed to allow for faster computer run-times. Of note, hydrostatic balance is frequently used (e.g., Kuirhara et al. 1998), and gradient wind balance is often used in axisymmetric models (Ooyama 1969; Emanuel 1995a). In contrast to these techniques valuable to computer integration are balanced models specifically designed to interrogate particular aspects of storm evolution. These are not frequently evolved in an operational forecast setting, but are useful to diagnose important features in hurricanes.

Balanced models (following the presentation of Shapiro and Montgomery 1993) act as dynamical filters removing the "fast manifold" gravity waves in favor of the "slow manifold" of advecting dynamics (Leith 1980). This filter of the dynamics serves to reduce the dimensionality of the problem. In a three-dimensional setting, using a small Rossby number expansion, the quasi-geostrophic set of equations can be found (Charney 1948). A generalization is available by retaining first-order Rossby number terms in the vertical vorticity and divergence equations to find the "balanced equations" (Lorenz 1960; Charney 1962). Shapiro and Montgomery (1993) present the asymmetric balance equations, which describe small disturbances on a translating symmetric vortex.

Eliassen (1951) showed a form of balance in axisymmetric geometry that can describe secondary circulations of vortices given known heat and momentum forcings and applied this result to the general circulation. Shapiro and Willoughby (1982) demonstrate application of Eliassen's model to hurricanes. It can be shown that the asymmetric balance equations reduce to Eliassen's model in

the axisymmetric limit (Shapiro and Montgomery 1993; Möller and Shapiro 2002). Eliassen's model has been used to diagnose the impacts of environmental forcings on the axisymmetric hurricane vortex (Molinari and Vollaro 1990; Bosart et al. 2000; Möller and Shapiro 2002). Asymmetric balance inversion was used by Möller and Jones (1998) to construct the balanced wind and height fields knowing the potential vorticity distribution of a hurricane and by Möller and Shapiro (2002) to diagnose the effect of specific environmental features on a hurricane.

1.3 Outline

Chapter 2 applies the output of an operational forecast product of the third school of Section 1.2.2, the Geophysical Fluid Dynamical Laboratory Hurricane Prediction System (Kurihara et al. 1998), as a first step in an examination of the processes that influence real hurricanes for a specific case: Hurricane Opal (1995). The underlying premise is that since the atmosphere and hurricane are not fully observed on a mesoscale, a model simulation that is initialized by an operational data assimilation system and is able to resolve an interaction between the hurricane and its environment on the mesoscale resolution of the model can serve as a surrogate for reality, so long as the model simulation performed well. Chapter 3 provides a review of E-MPI theory, which will be referenced extensively in subsequent sections. Chapter 4 examines some purely numerical influences on a model of the first school by Emanuel (1995a). This research is in part motivated by the potential deployment of a coupled ocean-atmosphere version of the same model (Emanuel 1999) to operational forecasting. Chapter 5 presents another model of the first school, showing another sensitivity of modeled intensity to numerical parameters. From this we will be able to suggest how the hurricane is able to access a second source of heat to aid intensity through an *ad hoc* modification of E-MPI. Chapter 6 will provide some context for these results.

Chapter 2

MODELED INTENSITY CHANGE IN HURRICANE OPAL (1995)

This chapter examines hurricane intensity change in the Geophysical Fluid Dynamics Laboratory (GFDL) Hurricane Prediction System model (hereafter, GFDL model) (Kurihara et al. 1995, 1998) for the case of Hurricane Opal (Atlantic basin, 1995). The case presented is of particular interest because of the rapid, and unforecasted, rate of intensification of the storm. The model provides an opportunity to study the interaction of an intensely rotating, convecting vortex in a reality-based, numerical representation of a synoptic-scale troposphere. This study falls between the broad-scale examination of Molinari and Vollaro (1989, 1990) and the study of the internal responses of a hurricane in higher resolution models (Liu et al 1997, 1999; Zhang et al. 2000; Braun and Tao 2000). The presented model simulation mimics well the observed intensity trend of the storm. Thus we believe the GFDL model is well-positioned to model the response of a hurricane-like vortex to the observed, large-scale effects that are represented in the initialization. These results have been presented in Persing et al. (2002).

2.1 The GFDL model

Opal reached hurricane intensity off the northwest coast of the Yucatan Peninsula in the southern Gulf of Mexico at 1200 UTC 2 October 1995, according to the "best track" summary produced by the National Hurricane Center (NHC) (United States). After drifting slowly westward over the next twenty-four hours, Opal began to traverse the Gulf of Mexico moving north-northeast around 1200 UTC 3 October 1995, intensifying from 80 kts to 130 kts by 1200 UTC 4 October 1995, then weakening prior to landfall on the Florida panhandle (Fig. 2.1, heavy, solid line).

For this study, the GFDL model was initialized at 1200 UTC 3 October 1995 and output was extracted at a three-hour interval until 36 hours (0000 UTC 5 October 1995). Forecasts from the 1997 version of the model, more fully described by Kurihara et al. (1998), are used here. The

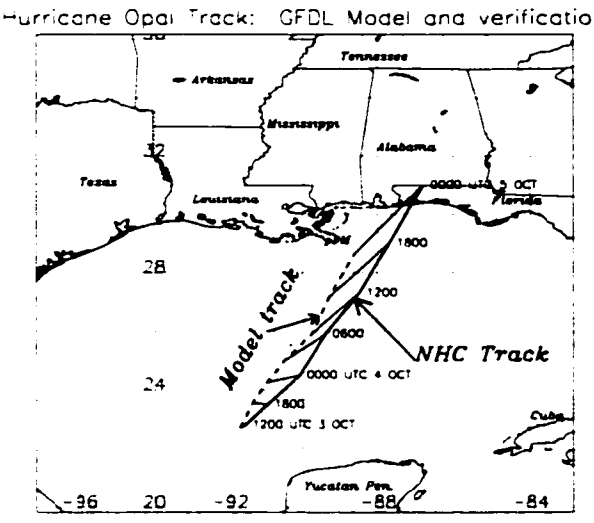

FIGURE 2.1: The "best track" (heavy, solid) of Hurricane Opal and model forecast track (dashed). Thin solid lines connect model forecasts and verifications at each time and are a measure of error. The letter "M" near (29N, 89W) denotes the mouth of the Mississippi River.

model is integrated in a terrain-following sigma coordinate system comprised of 18 vertical levels with dense coverage at lower levels (Table 2.1). Grid points are spaced within three interacting, grid domains: 1) a fixed, coarse (75° × 75°) domain of 1° grid spacing covering North America and the adjacent Pacific and Atlantic Oceans, and 2) two movable, finer mesh domains of 1/3° and 1/6° grid spacing that are centered on the moving hurricane. The model output used here is simply the data fields from all three meshes interpolated to an intermediate grid mesh of 1/3° for the entire 75° × 75° fixed domain. This is a compromise dataset to allow output from the model over a complete forecast domain covering all of North America and the adjacent waters (examined, but not shown here) while still minimizing disk and computer costs during analysis. Spatio-temporal consistency of the vertical motion field as analyzed gives credence to our analysis of the coarse convective response shown below. Our focus here is on the large-scale forcings which are well-resolved at 30 km. The National Center for Environmental Prediction (NCEP) analysis provides the initialization fields for the GFDL model, whereupon the vortex in those fields is filtered out and a new vortex is introduced based upon the observed location and intensity of the tropical storm. The new storm is introduced by a controlled spinup process (Kurihara et al. 1993, 1995, 1998). This version of the GFDL model has a fixed surface temperature and does not model any ocean interactions (for an example of a coupled-GFDL-ocean simulation, see Bender and Ginis 2000).

TABLE 2.1: GFDL Model σ-levels for integration and p-levels (mb) used in this anaylsis.

σ-level	p-level
0.9950	1000
0.9815	988
0.9605	967
0.9204	925
0.8563	860
0.7772	780
0.6881	690
0.5935	600
0.4974	500
0.4248	425
0.3748	375
0.3248	325
0.2747	275
0.2234	225
0.1746	175
0.1244	125
0.0740	75
0.0207	20

The simulation of Opal is initialized at 1200 UTC 3 October 1995 beginning with an initial minimum surface pressure of 951 mb, then deepening to 917 mb over 24 hours (Fig. 2.2). After 24 hours, the central surface pressure weakens only slightly, until after 36 hours (not shown) when the storm weakens considerably after landfall. The initialization routine "fits" the observed wind structure. Given the approximation due to the grid spacing, a deeper initial central pressure is needed to fit the observed winds. The surface pressure trace presented here is based on a diagnostic report from the model at a one-hour interval, not the three-hour interval full-data fields presented below. Comparison with an even higher temporal resolution pressure trace contained within the report (not shown) verifies that this one-hour pressure dataset tracks the important changes in intensity in the storm. The time rate of change of central pressure (Fig. 2.3) will be used to identify intensifying stages in the storm. The peak winds at the lowest model level ($\sim$ 50 m) are used for comparison with the observed maximum winds at 10 meters (Fig. 2.4) in light of

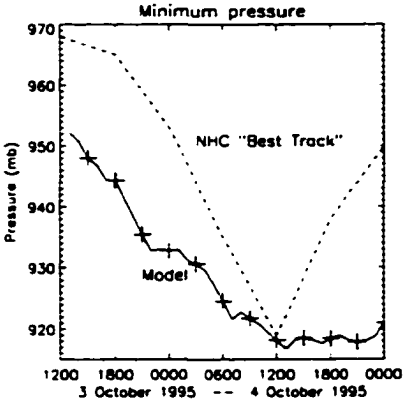

FIGURE 2.2: Minimum simulated storm pressure (mb) (solid) and that from the NHC "Best Track" (dotted). The crosses denote times where complete data fields are analyzed for this chapter.

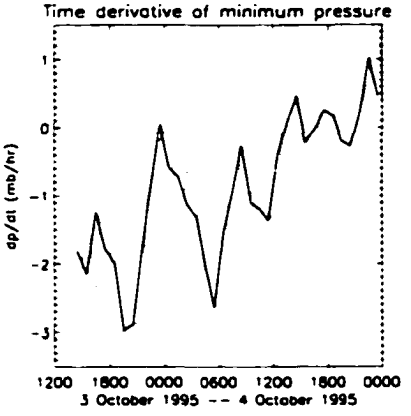

FIGURE 2.3: Time rate of change of minimum pressure (mb h^{-1}) computed from the sample of pressures at one-hour intervals (dashed) and a three hour running average of the same (solid).

recent dropsonde observations (Franklin et al. 2000; Black and Franklin 2000).[1] As expected, the initialization procedure provides for an accurate initial wind, but the model is less responsive than the observed storm, reaching a 51 m s^{-1} maximum. The strongest winds observed in the free atmosphere reach 79 m s^{-1}. The magnitude of variations in peak winds and central pressure are not as pronounced as in the observed storm, but on the basis of these results it is concluded that the phase of intensification for Opal is captured by this simulation. In particular, two instances of rapid intensification beginning at 1800 UTC 3 October and 0400 UTC 4 October are interesting in light of two such instances found by B00 at 0000 UTC and 1000 UTC 4 October 1995.

[1]Recent improvements in modeling the boundary layer in the GFDL hurricane model (subsequent to the present study) improve the wind-pressure relationship and better match the vertical structure noted in dropsonde observations.

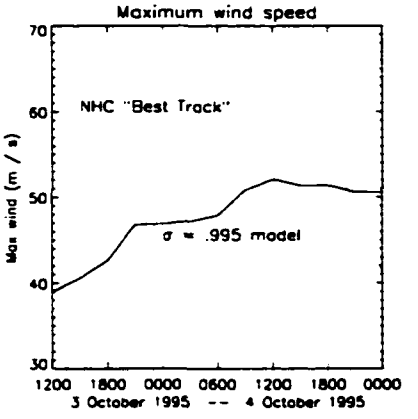

FIGURE 2.4: Maximum wind speeds simulated in the lowest model level (solid) and that from the NHC "Best Track" (dotted).

Two possible explanations for the intensification before (and weakening after) 1200 UTC 4 October (Bosart et al. 2000; hereafter B00) are modifications of the maximum potential intensity (MPI) determined from large-scale thermodynamic parameters and the passage of the eyewall over a warm core ocean eddy (WCE). The current simulation is not able to address the latter theory since sea surface temperatures (SSTs) are invariant in time and do not resolve any signature resulting from the WCE. There is a systematic bias in this version of the GFDL model to fill central surface pressures of hurricanes slowly during the decaying stage, possibly as a result of an unmodeled ocean interaction (Bender and Ginis 2000). The model hurricane tracks $\sim$ 100 km to the west of the observed storm, making landfall at the mouth of the Mississippi River in Louisiana (Fig. 2.1). The track errors do not greatly affect the underlying environment because the storm remains over the ocean for the same amount of time as observed and the ocean has no spatial variations in thermal content. Noting this, track errors of the storm relative to the unresolved WCE are not important. Errors of this size, though much smaller than the scale of the upper-level trough, could impact whether the trough is beneficial to intensification (Molinari et al, 1998), but the guarded success of the intensity of the model storm might suggest that the trough interaction in this simulation is representative.

2.1.1 Data processing

To reduce the size of the dataset to a level where the relevant variables could be considered simultaneously through a graphical user interface, a minimal dataset was created by interpolating the rectilinear GFDL model data to a storm-centered, cylindrical coordinate system. The storm center is located to the nearest tenth of a grid square ($\sim 1/30°$) at each time step using the minimum of the surface pressure field. A cylindrical grid is then defined with an outer radius of $\sim$ 1000 km, a radial grid spacing approximating the original grid spacing ($\sim 1/3°$ or 33 km), and 60 azimuthal grid points. The grid points in the rectilinear grid are unequally spaced in real space due to spherical geometry. A simple linear correction is applied in projecting the grid points to x- and y-coordinates centered on the storm that accounts for more than 90% of the position error of grid points considering the limited domain and the low latitudes in question. A full consideration of the spherical geometry would be needed for a much larger analysis grid or at much higher latitudes. A bicubic interpolator is used for horizontal interpolations from rectilinear to cylindrical coordinates. In the present analysis, the vertical coordinate of the cylindrical grid is pressure, with vertical levels (Table 2.1) selected to approximate the original vertical resolution in sigma coordinates. The data fields are linearly interpolated in the vertical from sigma to pressure coordinates and a mask is identified where grid points fall below the ground or above the top sigma level.

2.2 An illustration of hurricane/trough interaction

Figure 2.5 illustrates a single absolute vertical vorticity iso-surface at three times.[2] Colors are used for different vertical layers. The hurricane is evident as a nearly vertical tower of relative vorticity at the center of the analysis domain (the apparent offset is an aspect of the projection and low surface pressures at the center). A complex of stationary vorticity blobs (Fig. 2.5a) associated with the mountains of Mexico disappears from the foreground (Fig. 2.5b, c) as the analysis domain translates with the hurricane to the north-northeast. As the trough (and its cyclonically curved winds and vorticity) and the center of the hurricane approach one another, an increase of positive

[2]Potential vorticity, while exhibiting many of the same features as vertical vorticity in the mid- to lower-troposphere, is more difficult to display because it exhibits high values in the stratosphere which would sit in the foreground and obscure tropospheric features.

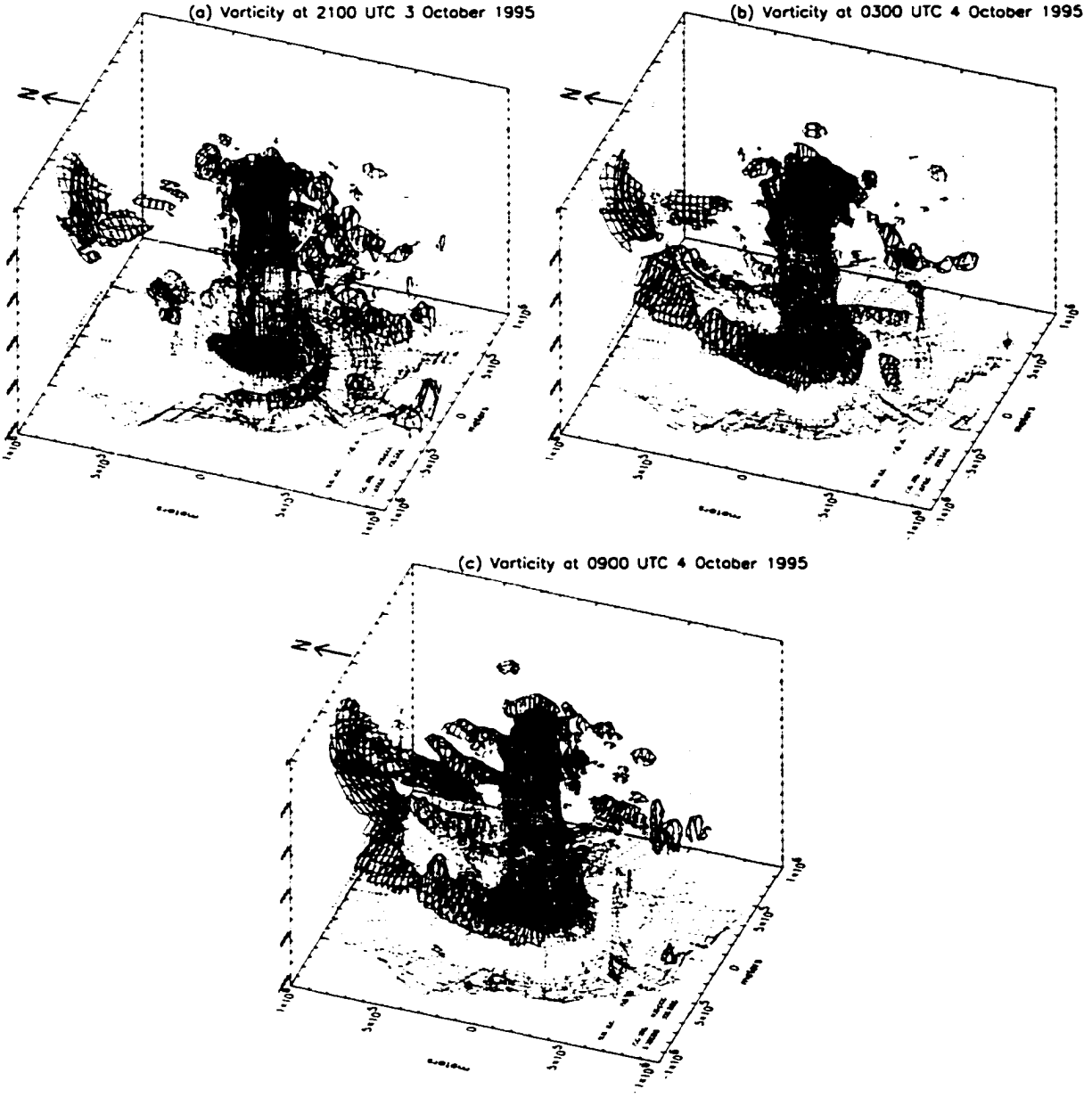

FIGURE 2.5: The 1.15×10^{-4} s^{-1} iso-surface of absolute vertical vorticity at (a) 2100 UTC 3 October 1995, (b) 0300 UTC 4 October, and (c) 0900 UTC 4 October. Colors denote vertical layers. Red - 1000 to 800 mb. Yellow - 800 to 600 mb. Green - 600 to 400 mb. Blue - 400 to 200 mb. Purple - above 200 mb. Gray represents the ground. Distances are in meters.

vorticity signature is evident to the north and west of the domain as time goes on (most evident in Fig. 2.5c). Middle-level vorticity at around 400 km distance from the center of the storm becomes more prevalent to the north and west of the storm and acquires a more filamented-character with time (Figs. 2.5b, c). Low level vorticity (in red) is organized in bands and shifts from an early preference south and east of the storm (Fig. 2.5a) to the north and west (Figs. 2.5b, c) and are generally located below regions of upward vertical motion (Figs. 2.16b, c compared with Figs. 2.5b, c).

The environmental flow is obviously affected by the presence of the storm. The presence of the trough northwest of the storm (Fig. 2.5c) is believed to influence the storm in several ways. First, it imposes an increased vertical shear across the storm. Second, it potentially provides an enhancement of the upper-level circulation of the storm through fluxes of eddy angular momentum (to be defined precisely below). These potential influences will be evaluated in turn below.

2.2.1 Shear

Following the technique of Bender (1997), an environmental wind can be defined by averaging the model winds in an annulus between 75 and 250 km radius on each pressure level. A measure of shear can then be defined by subtracting this environmental wind between two levels. The 850-200 mb shear defined in this manner is shown in Fig. 2.6. This measure follows closely other full tropospheric measures of shear, e.g. within a 600 km averaging radius found in DeMaria and Kaplan (1994b) and a 500 km averaging radius from B00.[3] Figure 2.7 shows the variation of 850-200 mb shear measures to variations in outer radius for the special case of having the inner radius of the annulus vanish (i.e., a filled circle). As can be seen, all averaging circles of more than 150 km radius (large enough so that asymmetric "core" effects near the storm contribute little to the sample) capture approximately the same signal, although the signal is most accentuated for radii between 200 and 400 km. Defining an annulus by using a non-zero inner radius (not shown) excludes the core and alters the computation only slightly.

---

[3]Following present operational practice at forecast offices and for comparison with the cited papers, the shear is expressed in terms of $m\ s^{-1}$ as the magnitude of the vector difference between two levels. A proper shear measure would divide through by an approximate depth between the two levels, about 10 km.

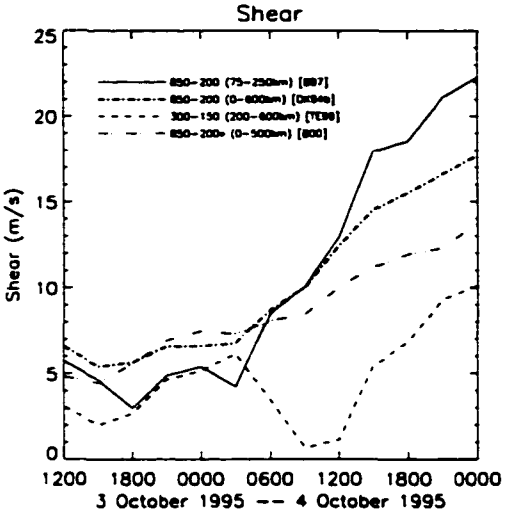

FIGURE 2.6: Vertical wind shear measures. The solid line is based on Bender (1997), the dash-dotted line on DeMaria and Kaplan (1994b), the dashed line on Titley and Elsberry (1999), and the dash-triple-dotted line on Bosart et al (2000). The later is starred to reflect the fact that it is computed as a difference between two layer averages (950 to 700 and 350 to 150 mb).

Interpretation of this result is complicated in the model simulation by sharp vertical shears in the environmental wind found in narrow vertical layers.[4] This suggests that the determination of shear will be sensitive to the selection of analysis layers. One test is presented in Figure 2.8 where the upper analysis level is varied from 250 to 150 mb. Use of a lower analysis level captures an early modulation near the 250 mb level in upper level winds, but use of the 150 mb level is sensitive (with a lag and with less magnitude) only to the later onset of shear. The environmental wind on each pressure level is presented in Fig. 2.9, which most closely resembles Bender's Fig. 12 (Bender 1997) for a simulation of a storm sheared from the rear. The component of storm-relative environmental wind in the direction of storm motion (Fig. 2.9a) gradually changes from front-to-rear at the surface to rear-to-front peaking around 250 mb, above which the imposed wind rapidly switches to front-to-rear again. The component of environmental wind perpendicular to storm motion (Fig. 2.9b) strengthens to over 5 m s^{-1} after 1200 UTC 4 October 1995 in a limited layer near 200 mb. The role that an environmental wind that changes direction with height can have on storm intensity is not clear. This layer strongly affects the 850-200 mb shear measure (Fig.

[4]The tropopause is generally found at 125 mb, if the tropopause is defined as the point of rapid increase in vertical gradient of potential temperature.

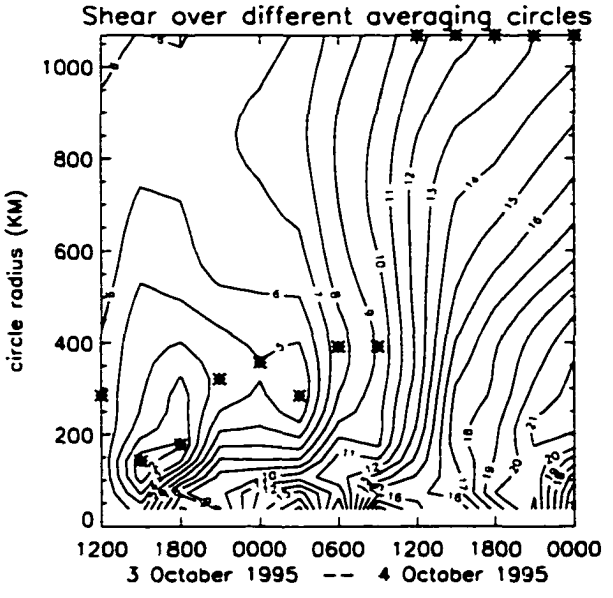

FIGURE 2.7: Vertical wind shear (m s^{-1}) across the 850-200 mb layer testing sensitivity to the exterior radius of the averaging circle. Stars denote the shear measure at each analysis time with a minimum value.

2.8, solid), but moderately affects the other two shear measures defined above and below 200 mb. Variations in the storm-parallel component of environmental wind strongly influence the 850-250 mb shear measure prior to 1200 UTC 4 October and accounts for the larger magnitude of this measure relative to the 850-200 mb measure. Opal stops intensifying at 1200 UTC 4 October, and after this time the storm can be considered strongly sheared with values approximately 13 m s^{-1}. This shear can be attributed to the southward and eastward progression of the jet stream (not shown) in response to the synoptic-scale trough. For context, a conventional hodograph plot of the environmental flow for a strengthening and weakening stage is shown in Fig. 2.10a and Fig. 2.10b, respectively. In the latter figure, the narrow layer of left-to-right shearing (relative to storm motion) can be seen.

The variations in environmental shear appear coincident with changes in the intensification rate within the GFDL model, despite the use of a moist convective adjustment parameterization whose responsiveness to increased shear is not clear and despite the coarse resolution (15 km) of the model integration. Two distinct events of lowered shear between 1500 and 1800 UTC 3 October and at 0300 UTC 4 October are coincident or slightly precede intensification events (Fig. 2.3). The eventual end to intensification, while not weakening as the observed storm did, is associated with

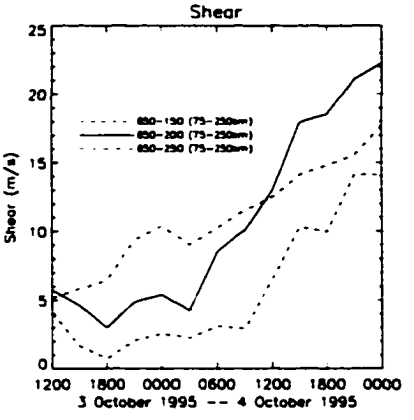

FIGURE 2.8: Vertical wind shear measures testing sensitivity to selection of analysis layers.

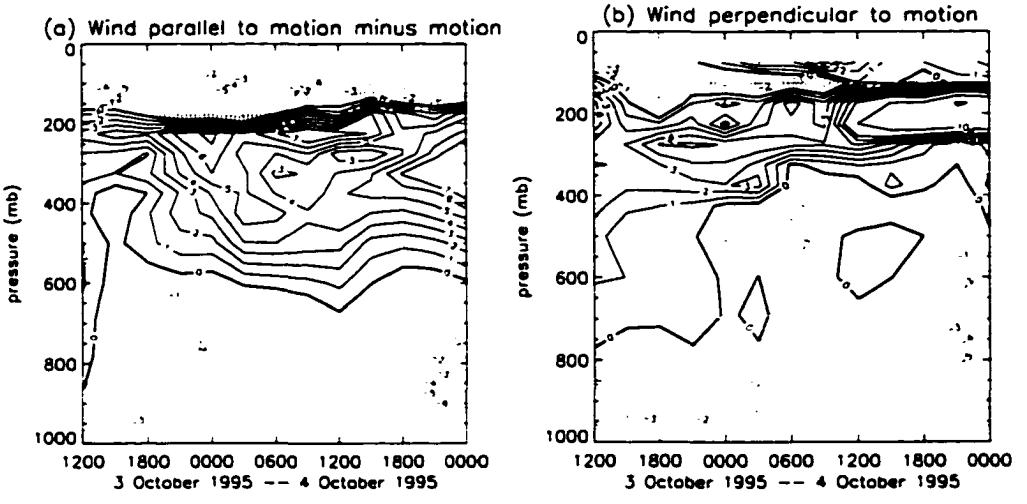

FIGURE 2.9: The mean component of the environmental wind (m s^{-1}) (using an averaging annulus of radii 75 and 250 km) (a) in the direction of storm motion with the storm motion subtracted, and (b) in the direction perpendicular to storm motion with winds from left to right (roughly from west to east) being positive. Contours are at $\pm 1, 2, 3, 4, 5, 6, 7, 10,$ and15 m s^{-1}.

both a long-term trend for increasing environmental shear (Fig. 2.6) and with a sudden shift in the character of environmental flow (Fig. 2.7) such that a minimum in analyzed shear at intermediate radii ($\sim$ 300 km) is no longer present.

2.2.2 Mean tangential momentum budget

A mean tangential momentum budget is constructed by casting the equations of motion into cylindrical coordinates, subtracting the storm motion vector from the wind, and finding azimuthal means (and asymmetries) of all quantities. Denoting the tangential wind by v, the radial wind u, and the vertical p-velocity by ω, the tendency of the mean tangential wind can then be written as

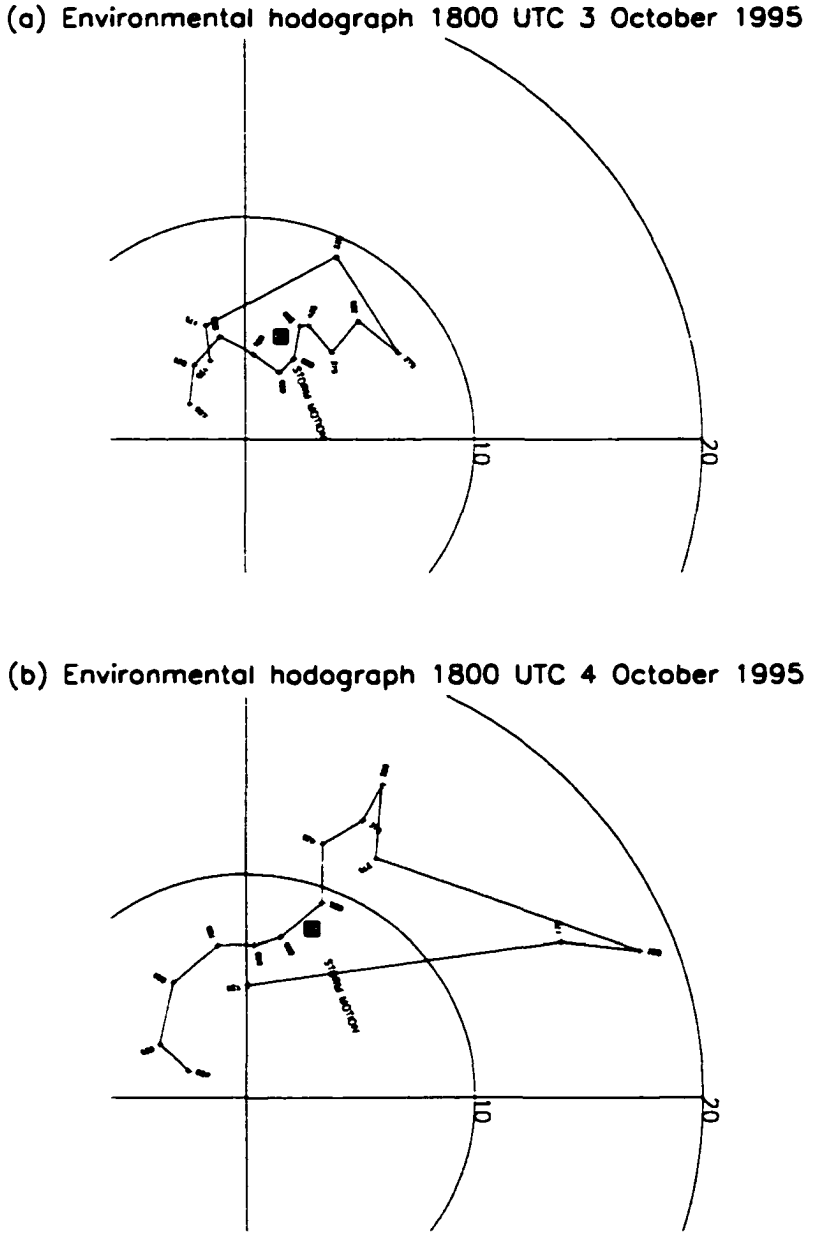

FIGURE 2.10: Hodographs of the environmental wind within an averaging annulus of radii 75 and 250 km at (a) 1800 UTC 3 October 1995 and (b) 1800 UTC 4 October 1995. The circles represent vector magnitudes of 20 and 10 m s^{-1}. The storm motion vector is displayed with a crossed box.

the sum of four terms, plus a friction term:

$$\underbrace{\frac{\partial \overline{v}}{\partial t}}_{\substack{\text{tangential}\\ \text{wind}\\ \text{tendency}}} = \underbrace{-\overline{u'\zeta'}}_{\substack{\text{eddy radial}\\ \text{vorticity}\\ \text{flux}}} + \underbrace{-\overline{u}\overline{\zeta}}_{\substack{\text{mean radial}\\ \text{vorticity}\\ \text{flux}}} + \underbrace{-\overline{\omega'\frac{\partial v'}{\partial p}}}_{\substack{\text{eddy}\\ \text{vertical}\\ \text{advection}}} + \underbrace{-\overline{\omega}\frac{\partial \overline{v}}{\partial p}}_{\substack{\text{mean}\\ \text{vertical}\\ \text{advection}}} + \text{Friction} \tag{2.1}$$

where ζ is the vertical absolute vorticity, overbars represent azimuthally averaged quantities, and primed quantities are deviations from that average. The friction term is computed using

$$\text{Friction} = p_{\text{sfc}}^{-1}\left[-\sin\theta\,({}_H F_x + {}_V F_x) + \cos\theta\,({}_H F_y + {}_V F_y)\right] \tag{2.2}$$

where p_{sfc} is the surface pressure, θ is the counterclockwise azimuth angle from east, ${}_H F_x$ and ${}_H F_y$ are components of the frictional force due to lateral stress, and ${}_V F_x$ and ${}_V F_y$ are components of the frictional force due to vertical stress (explained in detail in Kurihara and Tuleya 1974). Left out of this budget is the small beta term ($\beta r \sin\theta \overline{(u' + c_r)}$) where c_r is the radial component of the storm motion vector. With asymmetries on the order of 5 m s^{-1}, simple scale analysis suggests this term can provide for a 5 m s^{-1}d^{-1} tendency beyond 600 km radius, but in practice the in-phase relationship delays the importance of this term to further radii.

The tangential wind budget is then computed for a time of rapid intensification (1800 UTC 3 October 1995) and a pause in intensification (0000 UTC 4 October). The temporary pause still occurs within the long-term trend for intensification of Opal within the model and occurs before the onset of shear at later times in the simulation (Figs. 2.3, 2.9). The resulting tendencies in the r-p-plane are displayed in Figs. 2.11 and 2.12, respectively. At the intensifying time, the total mean tangential wind tendency computed from the budget (Fig. 2.11f) shows a vertically coherent tendency for spin-up at the eyewall from just above the ground to 320 mb, while the non-intensifying total budget tendency (Fig. 2.12f) has no such coherent structure, alternating between positive and negative tendency with height. At different vertical levels, different terms contribute to produce this coherent maximum in total tendency at the time of intensification. At that time, 1) the lowest levels ($\sim$ 850 mb) show a less negative eddy vorticity flux (Fig. 2.11a vs. 2.12a) and a stronger eddy vertical advection (Fig. 2.11c vs. 2.12c) relative to the non-intensifying time, 2) from 600 to 400 mb the eddy vertical advection is less negative (Fig. 2.11c vs. 2.12c) and mean vorticity flux

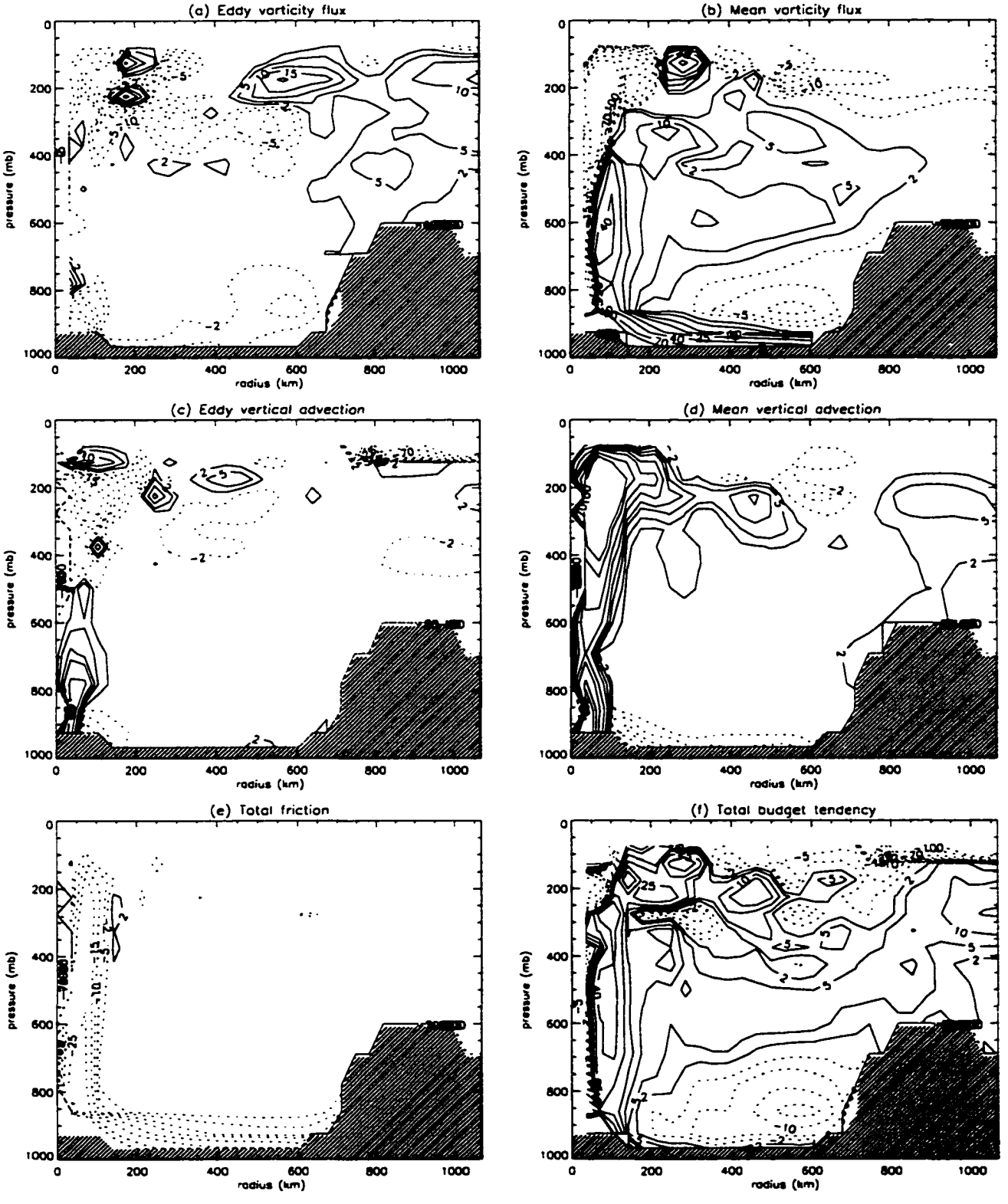

FIGURE 2.11: The terms of the mean tangential wind budget equation at 1800 UTC 3 October 1995. (a) Eddy vorticity flux. (b) Mean vorticity flux. (c) Eddy vertical advection. (d) Mean vertical advection. (e) Total friction. (f) Total of the five terms. The contours used are ±2, 5, 10, 15, 25, 40, 70, and 100 m $s^{-1}d^{-1}$. Dashed contours represent negative tendency for mean tangential wind.

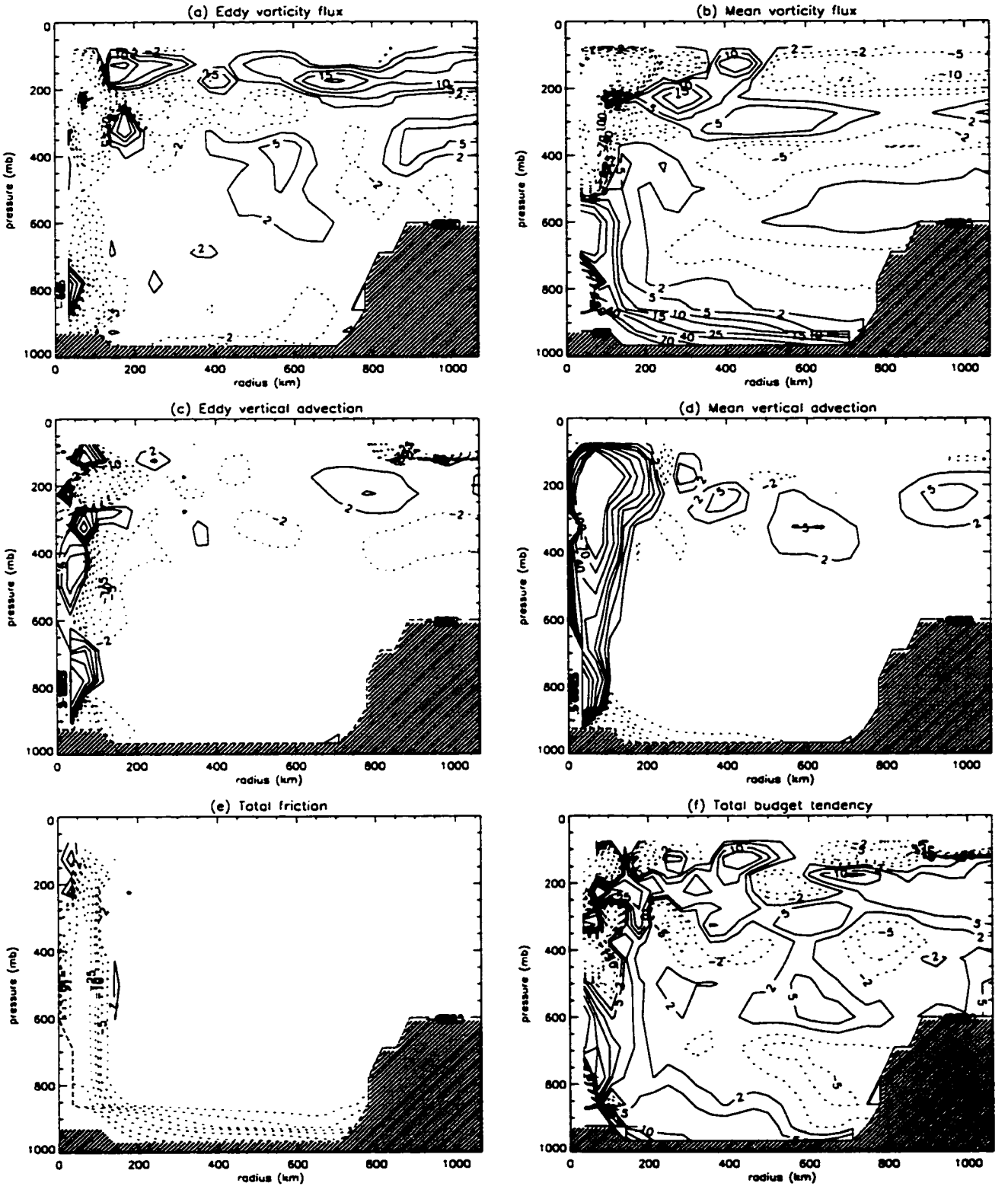

FIGURE 2.12: The terms of the mean tangential wind budget equation at 0000 UTC 4 October 1995. (a) Eddy vorticity flux. (b) Mean vorticity flux. (c) Eddy vertical advection. (d) Mean vertical advection. (e) Total friction. (f) Total of the five terms. The contours used are ±2, 5, 10, 15, 25, 40, 70, and 100 m $s^{-1}d^{-1}$. Dashed contours represent negative tendency for mean tangential wind.

becomes a strong positive (Fig. 2.11b vs. 2.12b), 3) above 400 mb the mean vertical advection is up to 40 m s^{-1} d^{-1} larger (Fig. 2.11d. vs 2.12d, difficult to discern in the figures presented here, but noticeable in difference plots) and the eddy vorticity flux is less negative (Fig. 2.11a vs. 2.12a), and 4) the friction is weaker throughout the eyewall by about 10 m s^{-1} d^{-1} (Fig. 2.11e vs. 2.12e). Many of these properties (greater vertical extent of positive tendency plus a reduction of negative eddy vorticity flux and enhancement of mean vorticity flux and mean vertical advection aloft) are consistent with a greater vertical extent of convection, suggestive of the Titley and Elsberry (1999) hypothesis, but examination of the vertical motion field (not shown) at these levels is less than convincing. Other features observed in the total budgets of mean tangential wind tendency are: 1) the apparent spin-down tendency in the boundary layer at intensification (Fig. 2.11f), and a spin-up at non-intensification (Fig. 2.12f), and 2) the enhanced middle troposphere spin-up (Fig. 2.11f) 200 to 800 km radius from the storm as a result of enhanced mean vorticity flux (Fig. 2.11b) at intensification. Composite averages (not shown) of multiple intensifying and multiple weakening times show that tendencies near the center of storm are robust, but in the far field there is more variation.

The eddy vorticity flux at 200 mb is presented as a function of radius and time in Fig. 2.13. Of note is the region of positive eddy vorticity fluxes exterior to 400 km radius, with negative values within. Titley and Elsberry (1999) proposed a pre-conditioning phase where eddy vorticity fluxes aloft provide a large-scale cyclonic environment at 200 mb that preceded rapid intensification of Typhoon Flo (1990). They hypothesize that a more cyclonic environmental aloft will lower the shear above a cyclonic vortex. During their analyzed rapid intensification phase, the eddy vorticity fluxes are weak and largely negative. In the Opal simulation considered here, the initialization is too late to test the pre-conditioning hypothesis, but throughout the simulation the eddy vorticity fluxes are more characteristic of the pre-conditioning phase of Titley and Elsberry (1999). In that phase, they showed eddy vorticity fluxes peaking at intermediate radii (400 to 1200 km, here 400 to 800 km) with values of $\sim$ 20 m $s^{-1}d^{-1}$, similar to that found in Fig. 2.13. It is found though in the GFDL Opal simulation that the mean eddy vorticity flux exhibited vertical structure, with much of the signal to be found above 200 mb (Figs. 2.11a, 2.12a), so the choice of level may vary substantially from storm to storm. There is no evidence of large-scale cyclonic circulation at this

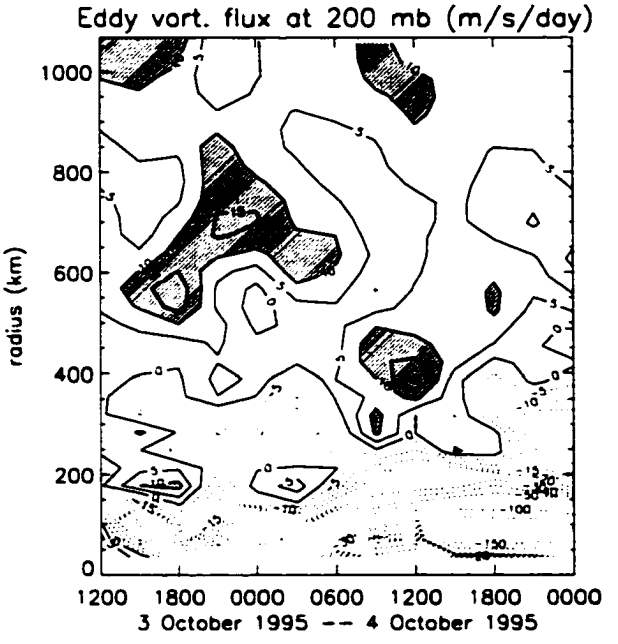

FIGURE 2.13: Eddy vorticity flux (m $s^{-1}d^{-1}$) at 200 mb as a function of radius and time. This is computed as an average of the 175 and 225 mb layers and azimuthal means are displayed. Shaded areas denote a greater than 10 m $s^{-1}d^{-1}$ tendency.

level (Fig. 2.14), with cyclonic circulation confined to within approximately 400 km, comparable with the rapid intensification phase of Typhoon Flo (Titley and Elsberry 1999).

There is a suggestion for inward propagation of eddy vorticity flux in Fig. 2.13 with enhanced values (> 10 m s^{-1} d^{-1}) appearing outside of 600 km radius before 0300 UTC 4 October 1995, then inside of 500 km radius around 1200 UTC 4 October. Molinari and Vollaro (1989) proposed such a signature for trough interaction in the development of Hurricane Elena. Given the track errors of this simulation, it is difficult to conclude that this process did not contribute to the intensification of the real storm, but the influences of eddy momentum forcings on the model storm can be examined within the Eliassen (1951) balanced vortex formulation, similar to examinations by Molinari and Vollaro (1989) and subsequent papers.

Our computation uses a pseudo-height vertical coordinate (Hoskins and Bretherton 1972; see also Section 5.4), requiring re-interpolation of the dataset from the original rectilinear, σ-coordinate to pseudo-height with a fixed 400 m vertical grid spacing, then interpolation to a cylindrical grid. The linearity of the elliptic partial differential equation for the mean transverse streamfunction driven by heat and momentum forcing allows us to consider the total balanced response as a superposition of separate source mechanisms for forcing over separate, arbitrary, mutually-exclusive

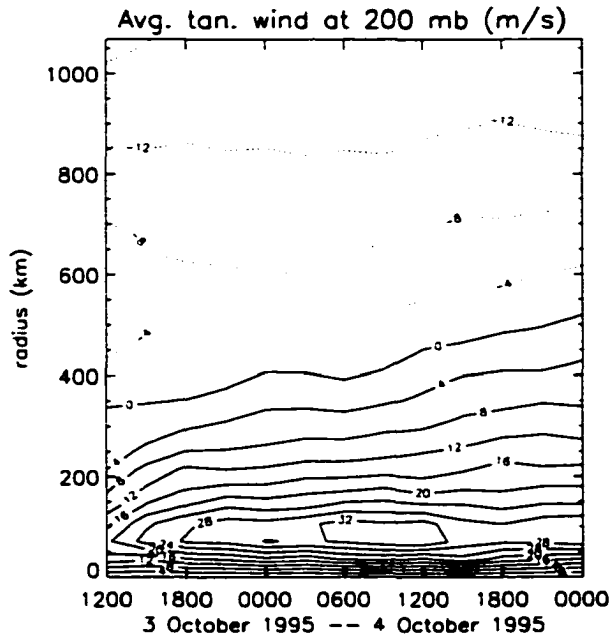

FIGURE 2.14: Azimuthal mean tangential wind (m s^{-1}) at 200 mb as a function of radius and time.

subdomains. To a first approximation, the mean secondary circulation and the attending mean tendency terms in the tangential momentum and heat budgets arise to counteract the mean diabatic heating in the eyewall and surface drag in the boundary layer so that thermal wind balance of the vortex is maintained (Willoughby 1979; Shapiro and Willoughby 1982). Consistent with the recent balanced diagnosis of this storm by Möller and Shapiro (2002), we have found that the mean diabatic heating rate associated with the latent heat release in the eyewall accounts for the mean tendency terms in the tangential momentum budget (not shown). Moreover, the variability in the mean terms appears to be governed by variability in the heating rate. Further discussion of this quantitative calculation is presented in Möller and Shapiro (2002).

We use the Eliassen model to examine the influence of the trough on the storm by taking the azimuthal mean static stability and primary circulation to define the vortex, considering all heat forcings to vanish, and considering the eddy flux of vorticity as the only momentum forcing. We confine the forcing to that plausibly associated with the trough by having all the eddy vorticity fluxes interior to 400 km radius vanish. The resulting secondary circulations and net tangential wind tendency (the original eddy flux forcing plus that inferred from the response of the balanced vortex) for intensifying and non-intensifying phases are shown in Fig. 2.15. Net tendencies largely remain outside 400 km radius and the induced secondary circulations at the eyewall are very weak

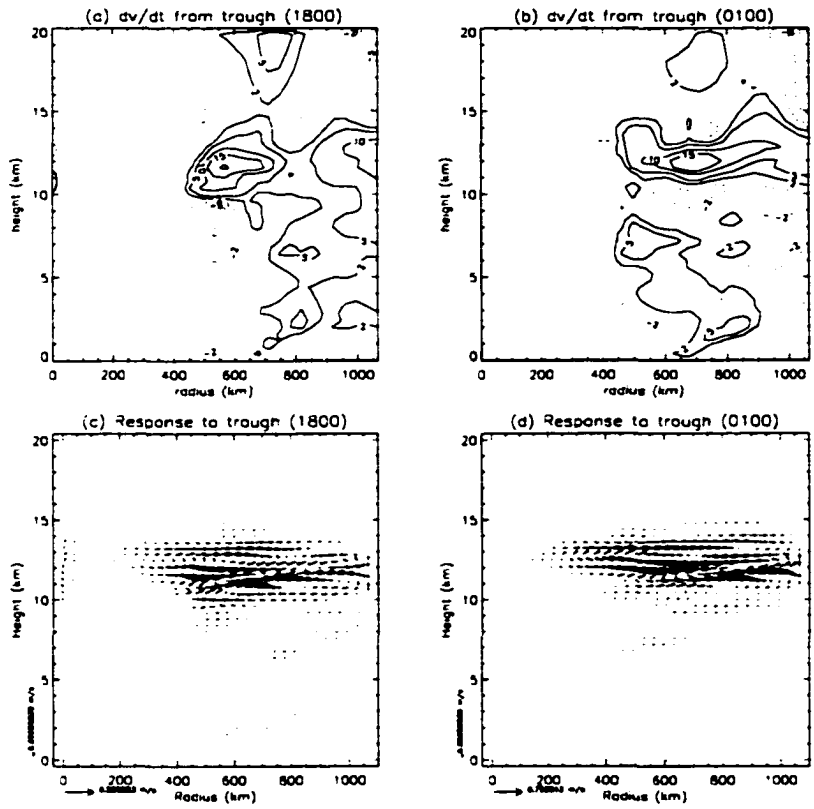

FIGURE 2.15: The tendency ($\partial/\partial t$) of mean tangential wind due to eddy vorticity fluxes exterior to 400 km radius and from the resulting Eliassen balanced vortex response of the same for a) 1800 UTC 3 October and b) 0100 UTC 4 October 1995. Also shown are the corresponding secondary circulations resulting from the same forcings respectively in panels c) and d). Maximum vector components are noted on either side of the origin.

($w \lesssim 1$ mm s^{-1}). According to this calculation the eddy flux forcing by the trough has only a negligible influence on the storm during both intensifying and non-intensifying phases. A second computation setting the static stability within the eyewall to a low value (one-half the value derived from the model basic state, 1×10^{-4} s^{-2}), acknowledging the ease of vertical motions there because of the convective feedback (Emanuel et al. 1987; Montgomery and Farrell 1993), produces nearly identical circulations and forcing. Based on these calculations, the hypothesized benefit of trough interaction does not appear to be supported in this simulation.

2.2.3 Upper-level divergence

Operational surface analyses performed by the National Center for Environmental Prediction (NCEP) (United States) show a surface trough over Louisiana, Mississippi, and Alabama from

1200 UTC 3 October to 0000 UTC 4 October 1995, moving the feature eastward after that (not shown). The surface trough is associated with heavy rain and thunderstorms. The GFDL simulation reproduces aspects of this feature, with upward motions evident over the same region (Fig. 2.16a-c, marker A). The convective line is the northern end of a long ($\sim$ 2000 km), deep (up to 600 mb), southerly fetch of moist air. Opal then traverses this warm maritime air mass as it heads north. Generally associated with this feature is an enhancement in relative vorticity (Fig. 2.17a, d, g, marker A) at the 925 mb level slightly to the west of its position. A vertically-stacked vorticity structure extends to the southwest from the mouth of the Mississippi River at 0300 UTC 4 October (Fig. 2.17g, h, i, marker B). Enhancement of 200-300 mb mean layer divergence (Fig. 2.18) (to $\sim 5 \times 10^{-5}$ s^{-1}) in this vicinity (markers A on all panels and B on panel c) is generally co-located with the vertical velocity pattern at lower levels, especially over land. These upper-level divergences correspond roughly with the same computation of B00 (their Figs. 6-8) using satellite-enhanced data assimilation procedures, except in the near vicinity ($\sim$ 300km) of the hurricane center. Near 1800 UTC 3 October (close to Fig. 2.18a), both analyses show a broad maximum over Alabama (marker A) with similar magnitude, and extension of positive divergence toward the eastern Gulf of Mexico and Florida (marker D). The GFDL forecast, however, produces an approximately stationary positive divergence maximum over the southern tip of Texas (Fig. 2.18a-c, marker C) that the satellite-based analysis did not capture. At 0000/0300 UTC 4 October, the satellite-based analysis pulls the former divergence maximum (marker A) further northeast from Alabama to Tennessee (extending to marker E in Fig. 2.18 b). There is less of this tendency in the GFDL forecast (Fig. 2.18b, perhaps as a result of the limited analysis domain presented here), but both analyses show divergence values around 2×10^{-5} s^{-1}. At 0900/1200 UTC 4 October, both analyses pick up on a north-south aligned convergence feature (Fig. 2.18c, marker F) over eastern Texas with a peak in divergence (marker B) near the mouth of the Mississippi River, and weaker divergences extending to the northeast. Noting this correspondence between the GFDL model-derived and satellite-wind enhanced divergence fields away form the storm, the GFDL model output may be able to test the hypothesis advanced by B00 (p. 347) that *this divergence feature helped "trigger the areal expansion of deep eyewall convection" in the first stage of intensification,* beginning in their analysis at 1500 UTC 3 October.

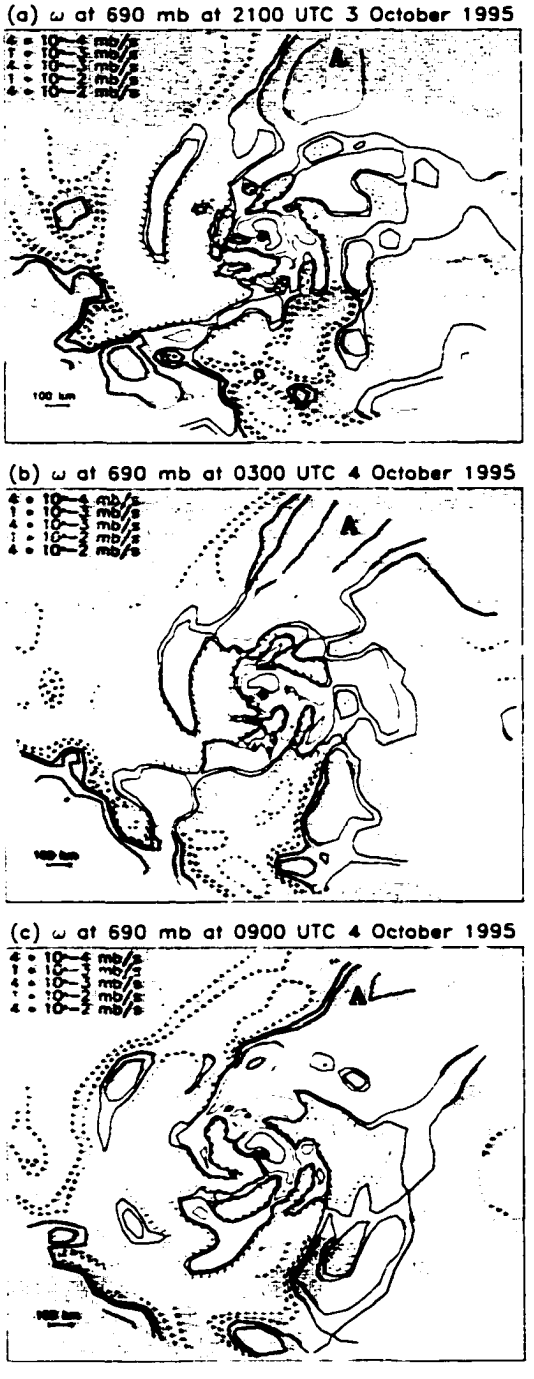

FIGURE 2.16: Vertical velocities, $\omega = dp/dt$, in terms of mb s^{-1} at (a) 2100 UTC 3 October 1995, (b) 0300 UTC 4 October, and (c) 0900 UTC 4 October. The magnitudes of contours are listed in the legend. The sense of the contours are reversed, so that solid contours are upward (negative dp/dt) motions, and dashed are downward (positive dp/dt) motions. The crosshairs mark the center of the storm. The letter "A" is referred to in the text.

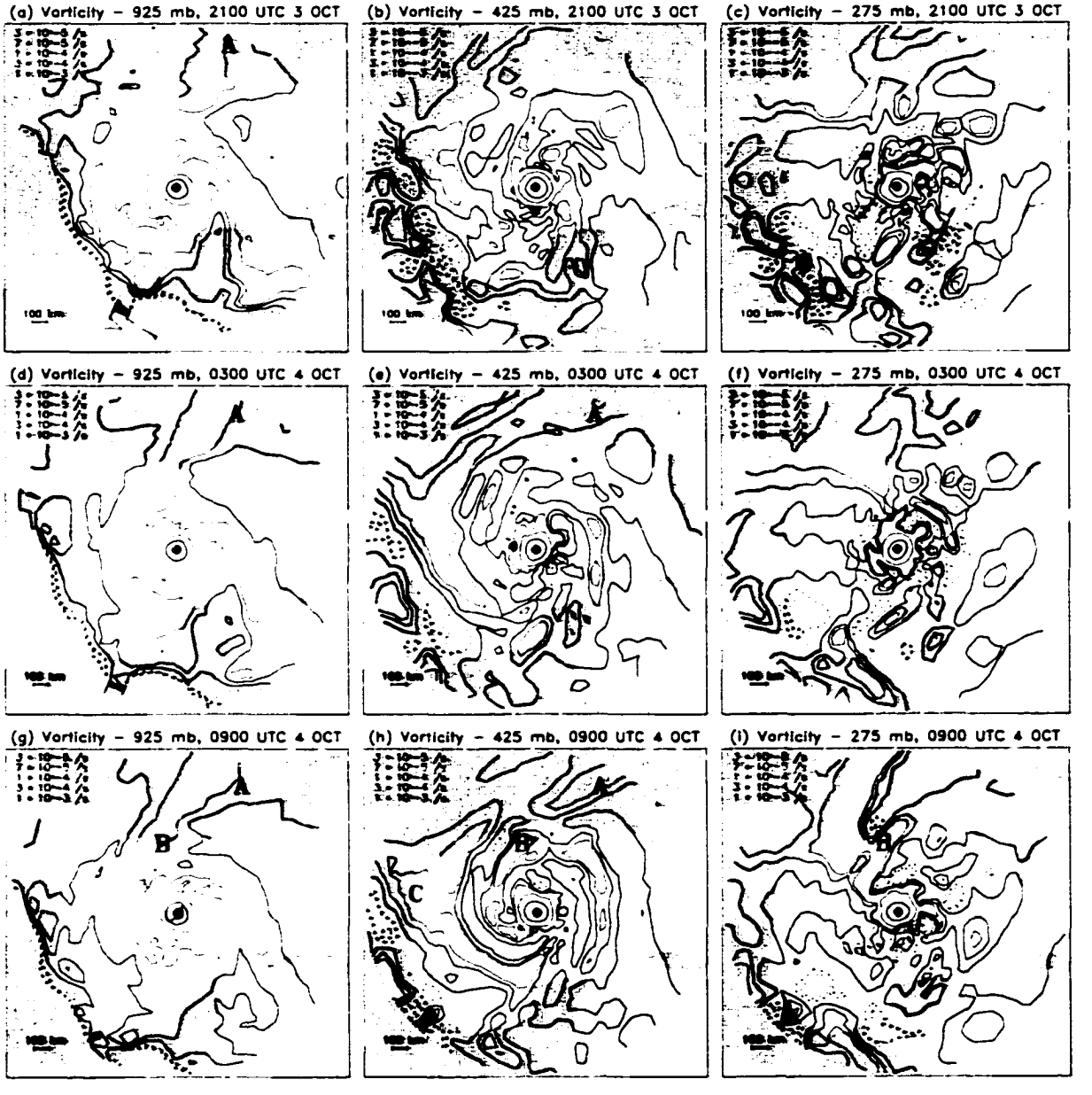

FIGURE 2.17: Absolute vertical vorticity at 1800 UTC 3 October 1995 at (a) 925 mb, (b) 425 mb, and (c) 275 mb, at 0300 UTC 4 October at (d) 925 mb, (e) 425 mb, and (f) 275 mb, and at 0900 UTC 4 October at (g) 925 mb, (h) 425 mb, and (i) 275 mb. The magnitudes of contours are listing in the legend. Dashed contours are negative. The crosshairs mark the center of the storm. Letters "A", "B", and "C" are referred to in the text.

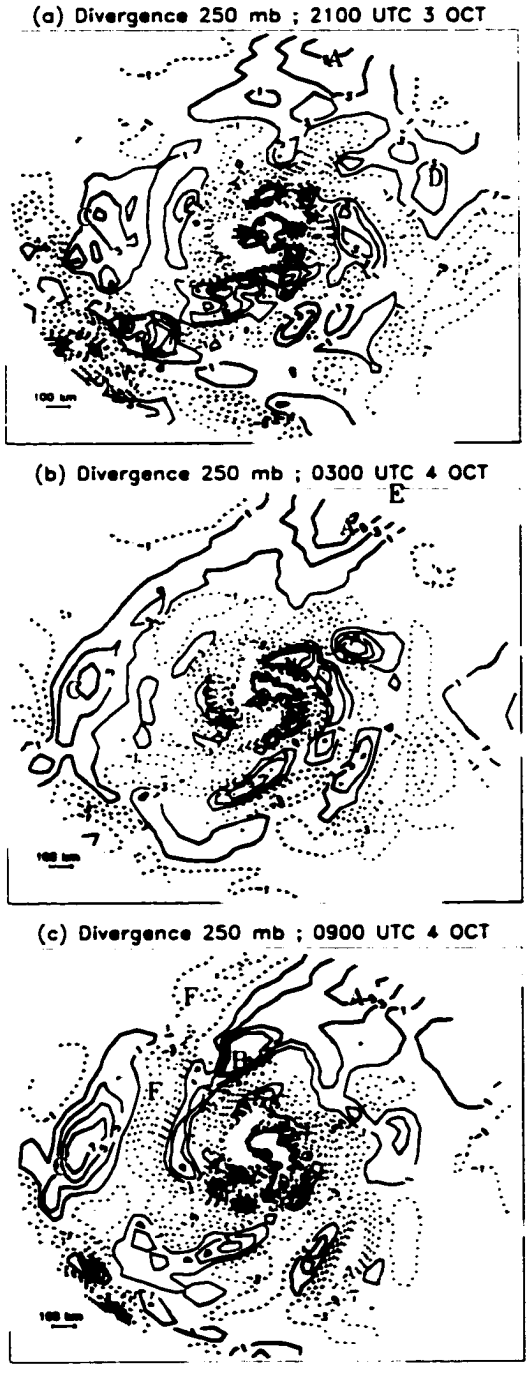

FIGURE 2.18: Divergence of the horizontal wind averaged between the 225 and 275 mb layers at (a) 2100 UTC 3 October 1995, (b) 0300 UTC 4 October, and (c) 0900 UTC 4 October. The contours displayed are $\pm(1,3,5,7) \times 10^{-5}$ s^{-1}, with only the leading digit shown. Dashed contours are convergent. The crosshairs mark the center of the storm. Letters are referred to in the text.

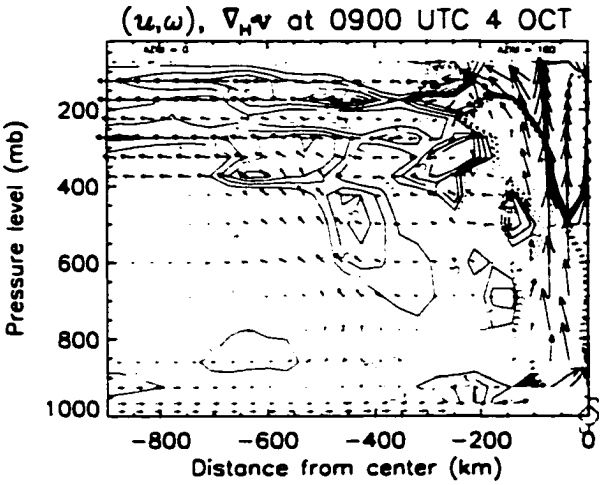

FIGURE 2.19: Vertical cross-section of radial and vertical winds and divergence at time 0300 UTC 4 October and the left edge is at 10° azimuth (just east of north). The hurricane center is at the right of the cross-section. The maximum vector represents approximately 26.4 minutes of translation, i.e. 89 m s^{-1} radially and 524 mb h^{-1} vertically. The contours of divergence are at $\pm (1, 3, 5, 7) \times 10^{-5}$ s^{-1}. Dashed contours are convergent.

In the GFDL analysis, the divergence co-located with the trough (from $\sim 5 \times 10^{-5}$ s^{-1} in Fig. 2.18 to a varying degree in all three panels , markers A and B (on panel c), north and west of the storm, peaking at $\sim 7 \times 10^{-5}$ s^{-1} in panel c) is never contiguous with the much stronger divergence ($\sim 1 \times 10^{-3}$ s^{-1}) associated with the hurricane itself at this level (small crosshairs at the center of each panel). From examination of the vertical structure of the divergence and radial/vertical flow (Fig. 2.19), we can see that the divergence and outflow pattern associated with the hurricane emerges above 200 mb. Furthermore, the most significant divergence features to the north (i.e., to the left of Fig. 2.19) are evident at lower levels. These lower-level divergence features appear to mark the upper boundary of a region of upward motions far removed from the center of the hurricane, associated with the convective line over Louisiana. The degree of correspondence between the upper level divergence pattern and the upward motions of the convective line suggests that the upper-level divergence is primarily responsible for (or primarily a reflection of) the convection over Louisiana. Given the assumption that the GFDL model reasonably simulated this aspect of the hurricane, it does not appear that the divergence aloft in the vicinity of the jet entrance region promoted extra lifting in the eyewall. In plan-view plots of the eddy quantities that contribute to the mean tangential wind budget (not shown), there is no noticeable contribution to storm intensification via the convective line.

2.2.4 Simulated vertical motions

Noticeable in the plan-view plots of vertical motions (ω, Fig. 2.16) is the systematic tendency for peak upward motions to lie just to the north of the storm (in front of the moving storm center). Also of note is the trend with time for downward motions in the southwest sector of the storm. To summarize these tendencies and to expose other trends in near-storm vertical motion, an analysis is performed on each azimuth from the center of the storm in the r-p-plane to find the peak upward motion (PUM) and peak downward motion (PDM) within the analysis grid. The analysis is limited to the first eight radial grid points (to $\sim$ 250 km) and is representative of the grid-scale (coarse-grain) response of storm vertical motions in the model near the hurricane. Taken together, the PUMs (and PDMs) define a set of 60 elements computed on each of the 60 azimuths. Figure 2.20 presents a summary of these samples as a function of time.

The mean PUM remains (Fig. 2.20b) about -0.07 mb s^{-1} (1 m s^{-1}) through most of the simulation, but the mean altitude of PUM (Fig. 2.20f) gradually descends from 400 to 600 mb with greater intensification episodes (1800 UTC 3 October and 0600 UTC 4 October, see Fig. 2.3) loosely associated with lower altitudes of mean PUMs and higher variance of PUM (i.e., enhanced convective asymmetry; Fig. 2.20d). The final episode of high PUM variance is not associated with storm intensification and occurs after the onset of strong shear (Fig. 2.6). Given the near constant mean in PUM, an increase in PUM variance is associated with an increase of extreme values of PUM (Fig. 2.20b, dotted). Generally, lower-altitude and more extreme upward motions may intensify the circulation of the storm through enhanced vortex stretching. If the third of the sample of PUMs (20 elements) that have the most extreme value is considered, there appears to be a transition after the onset of shear such that the altitude of these PUMs falls below that of the single strongest PUM (Fig. 2.20f, dashed vs. dotted). Observations of a weakening, sheared hurricane (Reasor et al. 2000) show a localized increase combined with a lowering of altitudes of upward motions, so this signal can be associated with both enhanced intensification (as realized in this model) and imposed shearing (both in the model and in theory). Both the extreme and mean PDMs (Fig. 2.20a) increase gradually throughout the simulation, although of an order of magnitude smaller than the PUMs. While the altitude of mean and extreme PDMs (Fig. 2.20e) show mixed trends through the simulation, of note is the inward migration of extreme PDMs toward

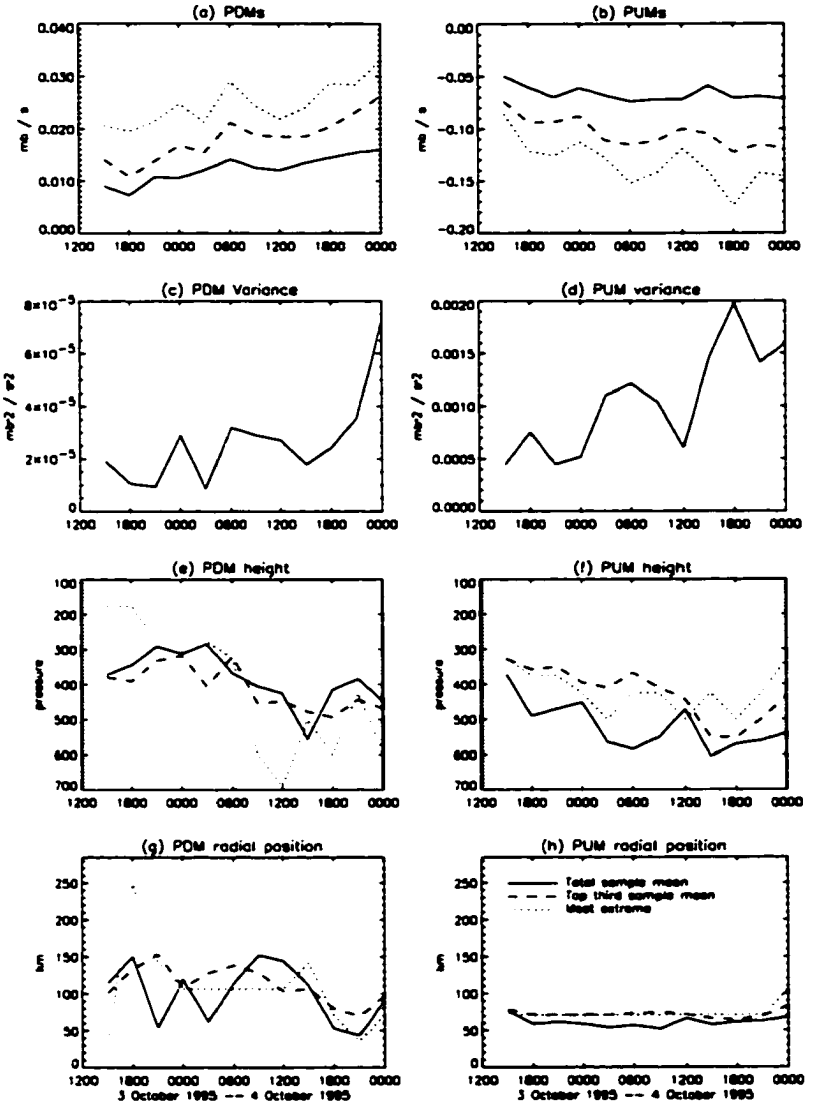

FIGURE 2.20: Statistics derived from the samples of PDMs and PUMs (see text), displayed as a function of time. Solid lines refer to the complete sample, while the dashed lines refer to the most extreme one-third of events and the dotted lines refer to the most extreme vertical motions. (a) PDM magnitude in mb s^{-1}, (b) PUM magnitude in mb s^{-1}, (c) Variance of PDM, (d) Variance of PUM, (e) Pressure level of PDM, (f) Pressure level of PUM, (g) Radial position of PDM, and (h) Radial position of PUM, plus legend.

the center of the storm (Fig. 2.20g), particularly after 1500 UTC 4 October when the storm has stopped intensifying. These latter PDMs exist at the same radius as the PUMs (Fig 2.20h), lying within the eyewall.

The vertical motion pattern observed in Fig. 2.16 is typical of the downshear enhancement of upward motion shown by observations (Reasor et al. 2000) and modeling studies (downshear and to the left in Frank and Ritchie 1999). This pattern is present more or less throughout the simulation,

without predictive value for the model storm. The PUMs highlight variations in convection during intensification, pauses during intensification, and highly sheared phases. Combined with PDM variance and radius, the different phases can be identified. The variations of the most intense sub-sample (here the most extreme third is used) appear to have the best diagnostic value.

2.3 Discussion

Studies of the role of environment in rapid hurricane intensification fall basically into two classes: 1) studies where given a benign (i.e., non-hostile), uniform environment, the hurricane reaches maximum intensity ("hostile environment" theories), and 2) studies where an environmental influence is advected into the proximity of the hurricane core to promote intensification ("stimulating environment" theories). Both classes rely on the ability of convection to aid intensification through middle-level inflows that conserve angular momentum or through stretching of the ambient vorticity field at low levels.

2.3.1 "Hostile environment" theories and modeling

Shear-based theories relate storm intensification to a reduction of vertical shear. Increased shear is hypothesized to ventilate a pocket of warm air aloft away from the eye of the hurricane, leading to an increase in surface pressure (Gray 1968), or to tilt a balanced vortex such that the thermal field consistent with it is altered and affects the stability of convection (DeMaria 1996; Jones 1995). Using 850-200 mb shear as a traditional measure of shear across a hurricane (Fig. 2.6), the Opal simulation shows a low value of shear (< 10 m s^{-1}, the threshold identified by B00) throughout the period of intensification (to 1200 UTC 4 October 1995, Fig. 2.2). Figure 2.9 though provides a more complicated picture. The mean flow at 850 mb is less than 2 m s^{-1} in both components of the flow, so most of the variability in shear is determined by the environmental winds aloft. Interestingly, 200 mb lies above the level of greatest storm-relative winds prior to 1200 UTC 4 October 1995 (i.e., through the period of intensification). Therefore, if a slightly different shear measure is selected (e.g., 850-250 mb) Hurricane Opal would appear to be highly sheared, with values approaching 10 m s^{-1} near 0000 UTC 4 October 1995 (Fig. 2.8). So while the shear environment prior to 1200 UTC 4 October 1995 was more beneficial to storm intensification than after that time, it should not be called an especially benign shear environment. The details of the

imposed environmental winds appear to be important. Between 2100 UTC 3 October and 0900 UTC 4 October, the perpendicular component is weak through the model atmosphere, with values confined between -3 and 5 m s^{-1}. After this time, a very strong left-to-right component of the mean wind up to 15 m s^{-1} is felt above 250 mb. A Green function technique is used to find the horizontal streamfunction and velocity potential at a particular level by respectively inverting the vorticity and divergence fields from that level. After the subsequent computation of rotational and divergent winds, it is found that the primary component of the introduced shear aloft is in the residual wind field (i.e., the difference between the total wind and the combined rotational and divergent wind). Such a residual wind field would be due to the presence of vorticity or divergence sources outside the analysis domain of 1000 km radius. Examination shows that this residual wind takes the form of a broad scale deformation flow with a col point in the vicinity of the hurricane. The onset of perpendicular shear is coincident with a shift of the col point to the east off of the center of the hurricane. The component of shear parallel to storm motion (with the storm motion subtracted) (Fig. 2.9a) is initially small, but soon after initialization (after 1800 UTC 3 October) the storm is sheared from the rear with an inflow of air at low levels from the front end (north end) of the storm, yet Opal still intensifies for the next 18 hours. A shear theory that seeks a simple numerical value between two levels is incomplete if it does not address particular arrangements of shear (twisting shear, shear relative to storm motion, shear confined in thin layers, etc.) and the role of a such complications to the intensity problem is not clear.

The maximum potential intensity (MPI) theory of Emanuel (1995b) is applied by B00 (their Fig. 21) to Hurricane Opal, suggesting that the lowering of MPI at later times interrupts the intensification of Opal. The modeling approach of Emanuel (1999) is an extension of this MPI theory, by including ocean interactions. The approach encapsulates the uniform, axisymmetric response of a hurricane to variations of surface heat exchanges with the ocean and to the thermodynamic profile of the ambient atmosphere. This type of forecast is dependent on an accurate track forecast. The influence of vertical shear is not accounted for in the Emanuel model and at times is used to explain inaccuracies in the forecast. Emanuel (1999) explains the initial intensification of Opal by the translation of the storm away from a pool of relatively cool surface water at the southern end of the Gulf of Mexico (B00). The cold pool developed as a result of frictionaily forced upwelling of the ocean caused by the surface winds of Opal as it stalled just west of the Yucatan Peninsula for

two days (Bender and Ginis 2000, their Fig. 7). The current simulation is not able to address this because the cold pool is not present in the initialization. Figure 1 in Emanuel (1999) summarizes several of his Opal simulations, where the best forecast (with a pronounced maximum followed by a weakening prior to landfall) includes the effects of sea surface temperature plus the effects of the warm core ocean eddy (WCE). Without the effects of the WCE, the Emanuel model intensifies Opal more slowly, reaching peak intensity at landfall. Emanuel's conclusion is that variations in surface fluxes controlled the variations in intensity of Opal. The GFDL simulation also weakens Hurricane Opal (slightly) prior to landfall, but the sea surface temperatures in the model vary by only 1 K across the Gulf of Mexico and the WCE is not present. In the GFDL model, the onset of large vertical shear is coincident with end of the intensification of Opal. We are left with two computer models that can successfully produce the modulation of the intensity of Opal, yet for apparently different reasons. This is not to minimize the importance of the WCE, but rather to point out a modulation of intensity due to atmospheric sources not present in the Emanuel model.

2.3.2 "Stimulating environment" theories

Montgomery and Kallenbach (1997) showed how vorticity asymmetries excited near the eyewall of a hurricane tend to symmetrize via sheared vortex Rossby waves. By their Fig. 8, the wave-mean flow interaction leads to an acceleration of mean tangential winds near the original asymmetry, and a slowing of the mean tangential winds exterior to the acceleration region. Such a wave-mean flow momentum transfer would be realized in the mean tangential wind budget as oppositely signed forcings in the eddy vorticity flux term. The present study has found that near the storm center negative eddy vorticity fluxes slow the mean vortex circulation at both lower and upper levels at every time step (although with variations in magnitude at different times). It may be that, at the model resolution presented here, the negative forcings on mean tangential winds, which by theory occur at outer radii, are simply more apparent. However, within the present dataset the eddy vorticity flux is found to be dominated by the signature induced by the shear, with negative radial winds at the front end of the storm at low levels and negative radial winds at the back end of the storm aloft. Once this shear-induced eddy vorticity flux signature is quantified, the possible roles of smaller scale (< 100 km) asymmetries may be addressed as in Möller and Shapiro (2002).

Beyond the inner core of the hurricane, vorticity asymmetries are also thought to aid intensification of a tropical cyclone (Challa and Pfeffer 1990; Molinari and Vollaro 1990). Because a vorticity asymmetry reflects that the hurricane is out of symmetric gradient wind balance, the vortex will try to restore balance by generating a secondary circulation. If a positive flux of eddy vorticity is introduced aloft, then balance can be restored by an outward wind at that level, which is associated with a negative tendency on mean tangential winds. Since it is introduced aloft, the secondary circulation is completed by enhanced inflow below this level and enhanced lifting at radii interior to the asymmetry aloft. Positive eddy vorticity fluxes are analyzed in the present analysis exterior to 400 km radius from the center of Hurricane Opal. Plan views of the eddy vorticity flux confirm their strong relationship with vorticity asymmetries aloft (i.e., Fig. 2.5). These results could suggest the importance of a reduction of scale of the vorticity features by a symmetrization process (Carr and Williams 1989), which is more favorable for ascent without the negative impact of an increased shear (Molinari et al. 1998). The results of section 2.2.2 indicate that this is not important for Opal in terms of enhanced lifting, yet it still may prove important in terms of reducing the negative impact (i.e., vertical shear) of vorticity features of large horizontal scale.

2.4 Conclusions

Hurricane Opal traversed the Gulf of Mexico and intensified very rapidly. While the shear environment may not have been hostile to storm development, it was not especially benign either, so this is not an ideal candidate for low shear intensification. The model hurricane nonetheless appeared to intensify as much as it could consistent with thermodynamic parameters of the problem (as illustrated by B00) up to a time defined by the onset of intense cross-vortex flows aloft. We suggest that the trough played a minimal role in intensification, supporting the model simulation of Emanuel (1999) (ref. their Fig. 1) where no effects of the trough are included in his axisymmetric model.

Different mechanisms are proposed, though, for the *weakening* of Opal by Emanuel (a decrease in ocean heat content) and by this paper (an increase in shear), which raises a scientific dilemma. We propose that the sensitivity of both storm intensification and weakening in the model may be tested by removing the trough from the initial data fields, re-initializing the model, and then analyzing the model output.

Chapter 3

E-MPI THEORY REVIEWED

3.1 Foundations

The energetically-based MPI (E-MPI) considered here is that first presented by Emanuel (1986) and updated with an improved representation of the eye in Emanuel (1995b, hereafter E95b) yielding a minimum surface pressure that depends on the ratio of exchange coefficients of enthalpy and angular momentum. Camp and Montgomery (2001) provided a summary of E-MPI and its physical basis. Bister and Emanuel (1998) updated E-MPI to include the effects of dissipational heating in the boundary layer, but since the model results presented below do not include this process the theory of E95b will be considered.

The basic functional form of E-MPI is

$$V_{max} = V_{max}(T_s, T_{out}, \mathcal{H}; p_{amb}, f, r_0) \tag{3.1}$$

where the maximum tangential wind V_{max} is a function of the SST (T_s), the outflow temperature T_{out} (defined precisely in Section 5.2 below), and the surface relative humidity $\mathcal{H}$ which is assumed to have the same value at the eyewall and in the environment. E-MPI is also a weak function of the ambient surface pressure p_{amb}, latitude through the Coriolis parameter f, and the size of the vortex where r_0 is the radius at which surface tangential winds vanish. In dimensional terms, Eq. 16 of E95b becomes

$$V_{max}^2 = \frac{C_k}{C_D}\left(\frac{\chi_{si}^* - \frac{1}{4}\gamma^* r_0^2 f^2}{1 - \frac{1}{2}\frac{C_k}{C_D}\gamma^*}\right) \tag{3.2}$$

where C_k/C_D is the ratio of the boundary layer exchange coefficients of enthalpy and momentum and is taken to be unity throughout this paper. The entropy variable χ has the units of energy per unit mass (i.e., squared velocity) and is defined by

$$\chi = (T_s - T_{out})(s - s_{bi}) \tag{3.3}$$

where $s = c_p \ln \theta_e$ is the moist entropy, s_{bi} is the initial ambient boundary layer value of moist entropy, c_p is the specific heat of dry air at constant pressure, and θ_e is the equivalent potential temperature (Holton 1992) which is conserved in pseudo-adiabatic ascent. In (3.2) the parameter

$$\gamma^* = A\frac{1-\mathcal{H}}{1-\mathcal{H}A} \tag{3.4}$$

where

$$A = \frac{T_s - T_{out}}{T_s} + \frac{\chi^*_{si}}{R_d T_s(1-\mathcal{H})} \tag{3.5}$$

and χ^*_{si} is saturation χ evaluated at the ocean surface and at ambient surface pressure; R_d is the gas law constant of dry air. Equations (3.2) - (3.5) are a closed expression for V_{max} and are largely insensitive to large and reasonable variations in r_o and p_{amb}. Figure 3.1 shows one solution as a function of T_s and T_{out} for $\mathcal{H} = 80\%$, $p_{amb} = 1015.1$ mb, $f = 5 \times 10^{-5}$ s^{-1}, and $r_0 = 400$ km.

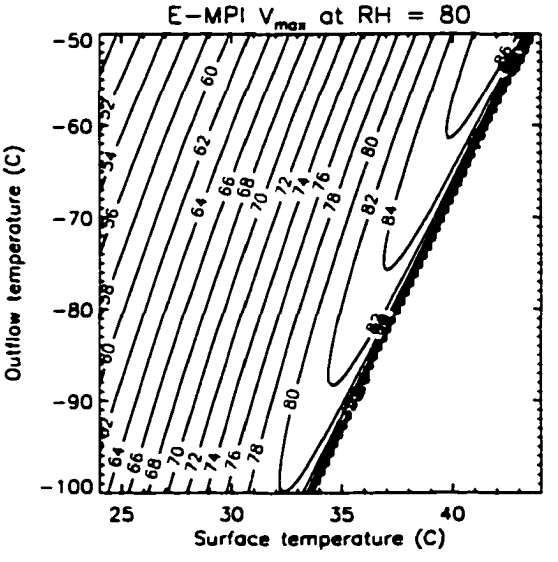

FIGURE 3.1: E-MPI as a function of T_s and T_{out}.

3.2 Boundary layer balance

Evaluation of $\mathcal{H}$ is problematic in the diagnosis of Rotunno and Emanuel (1987) model output (see Appendix C). Relative humidity is introduced into the derivation to both estimate the vertical entropy gradient between the boundary layer and the ocean surface and to join the solution at the eyewall with that in the environment (where values might be known in practice prior to cyclogenesis

from either climatology or routine data acquisition). By appealing to an earlier step in the derivation of E-MPI (Eq. 13 from E95b), we can find a "local" definition for tangential velocity at the top of the boundary layer as a function of radius:

$$V^2(r) = \frac{C_k}{C_D}\left[\chi_s^*(r) - \chi_b(r)\right]. \tag{3.6}$$

Here χ_s^* is the saturation entropy at SST, which is a function of radius because of the radial variation in surface pressure, and χ_b is the local entropy variable at the top of the subcloud layer and is taken to be representative of the full depth of a well-mixed boundary layer. Thus the squared velocity is proportional to the vertical difference of entropy across the boundary layer. This expression should be valid for the eyewall of a steady-state storms where $\chi_b(r)$ is maintained by a balance between loss due to radial advection in the inflow and gain from the ocean surface; and angular momentum is maintained as a balance between loss to friction to the ocean and spin up due to inward flux of environmental angular momentum. The expression is only valid at high cyclonic wind speeds and at small radii such as that found near the eyewall. Eq. (3.6) could not serve as a practical MPI (cf. Eq. 3.2) since the parameters cannot be determined before a storm forms; it nevertheless serves as a diagnostic of the accuracy of many assumptions (see Appendix C for a summary) used in deriving E-MPI.

Chapter 4

SOME SENSITIVITIES IN THE EMANUEL HURRICANE MODEL

This chapter examines sensitivities to changes in resolution in the Emanuel 1995a (hereafter, E95a) hurricane model (E95a model). This model was used in E95a to verify the theoretically predicted, energetically-based, maximum potential intensity (E-MPI) for a hurricane (Emanuel 1995b, hereafter E95b: see Chapter 3) that has an analogy to the classical Carnot cycle (e.g., Emanuel 1988). After coupling this atmospheric model with a sequence of simplified column ocean models, Emanuel 1999 (E99) showed that this approach can be successfully applied in "hindcast" mode to historical storms, provided that the forecast storm track can be supplied as input. While there are some notable failures in E99, to which many complicating factors can be invoked such as shear that would fall out of the scope of the proposed model, there are many remarkable successes detailed. The E95a model then, when coupled to an ocean model as presented by E99, presents an obvious opportunity to deliver a new product to hurricane forecast offices. The approach here is to test sensitivities in the E95a/E99 model that might affect its role as a candidate operational forecast model.

4.1 Model description

The model used for this study is the axisymmetric, three-layer hurricane model described by Emanuel (1989: hereafter, E89) with further modifications described by E95a. The model is formulated with a grid spacing in the radial is fixed in terms of potential radius

$$\frac{f}{2}R^2 = rV + \frac{f}{2}r^2. \tag{4.1}$$

where r is the physical radius, f is the Coriolis parameter, and V is the tangential wind. For fixed f, potential radius has a monotonic, one-to-one relationship with absolute angular momentum

$$M = \frac{f}{2}R^2. \tag{4.2}$$

The description of the atmosphere in the vertical is reduced to just three levels: 1) the top of the sub-cloud layer (hereafter subscripted with b) which is assumed to represent the entire boundary layer, 2) the middle troposphere (subscripted m), and 3) the tropopause level (subscripted t). At level b, momentum (through evaluation of r_b), entropy, saturated entropy, streamfunction, updraft mass flux, and downdraft mass flux are evolved. At level m, only entropy is evolved. At level t, only momentum is evolved. The entropy variable χ is defined by (3.3). Further details of the model can be found in E89 and E95a. For this presentation, we focus primarily on the low-level momentum field described by (4.1) and the deep convective mass flux

$$G \equiv \int_0^r \sigma \omega_c r' dr' \tag{4.3}$$

where σ is the cloud fraction and ω_c is the vertical p-velocity of the convecting clouds. The interpretation of G as a radial flux of mass in the boundary layer needed to satisfy the requirements of convection or as the radial integral of the vertical mass flux of convection are complementary.

4.2 Experimental configuration

The E95a model was kindly provided to us by K. Emanuel complete with a working set of adjustable parameters (summarized in Table 4.1) which we use as a "default" configuration. The drag coefficient is found using

$$C_D = C_{D_0} + c|V|. \tag{4.4}$$

Table 4.2 compares the default configuration with the configurations used in other studies using variations of the E89 model. The E95a model differs from the E89 model (as detailed in E95a) primarily in its convective parameterization, but also in the addition of momentum diffusion in the upper troposphere, the handling of radiational cooling, and the lack of downward advection of entropy from upper to lower troposphere. Schade and Emanuel (1999; hereafter SE99) couples the E95a model to a three-dimensional ocean model, allowing the surface flux of entropy under the hurricane to suffer the negative feedback caused by wind-induced mixing in the ocean of deeper, cooler waters to the surface (see multiple citations within SE99). To approximately represent the same feedback of SE99, E99 couples the E95a model with a series of one-dimensional ocean models that are spaced out along the path of the hurricane.

TABLE 4.1: Parameters for the default model run.

	Variable	Value
T_s	Sea Surface Temperature	27.0 C
T_{out}	Outflow Temperature	-70.0 C
$\mathcal{H}$	Ambient Relative Humidity	0.80
p_0	Ambient Surface Pressure	1013.0 mb
f	Coriolis Parameter	5×10^{-5} s^{-1}
C_{D0}	Surface Drag Coefficient	1×10^{-3}
$\frac{C_k}{C_D}$	Ratio of Exchange Coefficients	1.0
c	Wind Dependence of Surface Fluxes	3^{-5} s m^{-1}
$\frac{l}{\Delta R}$	Normalized Mixing Length	0.03
τ_{rad}	Radiative Time Scale	8.0 hr
	Cap on Radiative Cooling	2.0 K d^{-1}
τ_c	Convective Time Scale	1.0 hr
Λ	Entropy Detrainment into Lower Troposphere	0.35
Δp_b	Boundary Layer Depth	50 mb
r_m	Initial Radius of Maximum Winds	60 km
r_0	Initial Radius of Zero Winds	400 km
V_m	Initial Maximum Wind	15 m s^{-1}
$\mathcal{H}_m$	Initial Lower Tropospheric Humidity	0.60
(NR)	Number of Radial Nodes	50
$\Delta\tau$	Time Step	30 s
R_o	Radius of the Outer Wall	1200 km

TABLE 4.2: Comparisons of the present default configuration with other studies using variations of the E89 model. Parenthetical values denote the explored range of each paper for each parameter.

Variable	present study	E89	E95a	E99	SE99
(NR)	50 (25 - 200)	24 (12 - 30)	30	50	48
R_o (km)	1200	1500	1000	1000	2000
implied resolution (km)	24.0	62.5	33.3	20.0	41.7

The different simulations presented in this chapter and in Appendices A and B are summarized in Table 4.3. Model variables are interrogated at a nearly fixed interval in time of one-tenth of a day ($\sim$ 8600 s).[1] When the radial resolution is varied, the time step is varied proportionately to anticipate a CFL criteria. It is not necessarily assured that such a criterion is valid, but further

[1]The time step in the model can vary as the peak wind speed develops, necessitating an approximate output interval. The time step referred to in the rest of the paper is the initial or "basic" time step.

TABLE 4.3: Simulations presented.

Simulation name	Differences from default
Default	The default configuration.
DoubleRes	$(NR) = 100$
QuadRes	$(NR) = 200$
SensExp	See Table 4.4.
Hypercane	$T_s = 33.86$C, $T_o = -102.15$C, $p_0 = 1015$mb
DoubleResConv	$(NR) = 100$, suppressed convection outside of the eyewall
SecEyewall1	at 5 simulation days, force $r(P_{\text{index}} = 9) = r(P_{\text{index}} = 10) - 1$ km
SecEyewall2	at 5 simulation days, force $r(P_{\text{index}} = 10) = r(P_{\text{index}} = 9) + 1$ km

tests using successively smaller time steps for a sample integration (Simulation *DoubleRes*) showed very similar results.[2] The exception to this rule is the set of simulations *SensExp* which use a single time step sufficiently small to model the entire set.

4.3 Results

4.3.1 Two types of model behavior

Pseudo steady-state behavior

Summary information (peak winds, minimum central pressure, and radius of peak winds as a function of time) for Simulation *Default* is shown in Fig. 4.1. The behavior of the model is similar to the "control run" of E95a (Fig. 2 of that paper), with an early weakening in vortex maximum winds followed by an intensification, then a nearly steady state. The early weakening of the model storm was noted by E89 and E95a, which proposed the importance of saturating the mid-levels on the mesoscale at the nascent eyewall. The surface radii of each potential radius grid point as a function of time is displayed in Fig. 4.2 as an alternate way of summarizing the simulation. This is equivalent to tracing contours of angular momentum through time. Closely spaced angular momentum contours (i.e., potential radius grid points) imply a large radial gradient in tangential

[2] Another version of Simulation *DoubleRes* using double precision arithmetic was indistinguishable from the single precision version of *DoubleRes* out to 20 simulation days, after which time both simulations were no longer identical but had similar behavior. All simulations shown in this chapter are single precision.

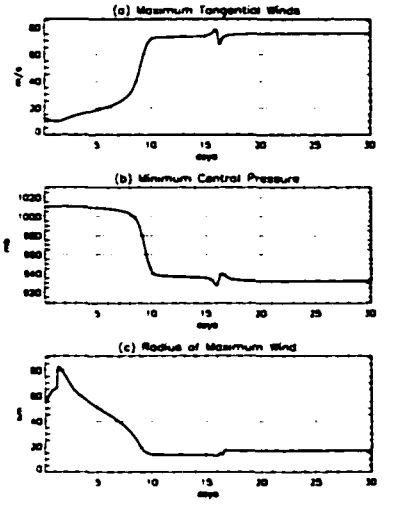

FIGURE 4.1: (a) Peak tangential winds, (b) minimum central pressure, and (c) radius of peak winds as a function of time for Simulation *Default*.

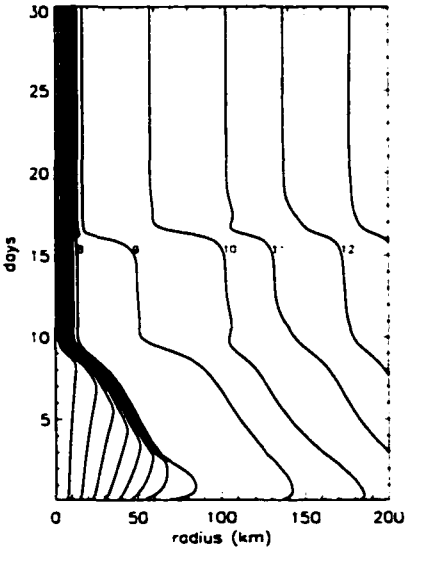

FIGURE 4.2: Surface radial positions of each model grid point (R-coordinate, i.e. contours of constant angular momentum) as a function of time for Simulation *Default*. Numbers within the plot label well-spaced grid points by index number, with the zeroth index being the invariant boundary grid point at $r = 0$.

wind, as can be seen from the definition of potential radius R (4.1). The developing eyewall of the hurricane is evident by the closely spaced grid points that move in from approximately $r = 70$ km at day 2 to $r \leq 20$ km at day 10. By comparing Figs. 4.2 and 4.1c., we can see that the radius of maximum winds (RMW) tracks closely the radius of the outer-most grid point of this "bundle" of grid points. This location is also commonly the location of peak convective activity in the model, therefore the outer-most position of the bundle will be used here to characterize the eyewall.

The evolution at the top of the planetary boundary layer of the radius of a model R-grid point (r_b) can be described in non-dimensional terms using tildes (generally following the convention of E89 and E95a) as

$$\frac{\partial \tilde{r}_b^2}{\partial \tilde{\tau}} = \tilde{G} + \tilde{\psi}_{\text{Ekman}} - \tilde{\psi} - \tilde{D}_b \tag{4.5}$$

where τ is time in (R, z, τ)-coordinates, G is the deep convective mass flux, ψ_{Ekman} is the streamfunction contribution due to inflow in the boundary layer, ψ is the streamfunction in the absence of convection, and D_b is the diffusion term. Equation (4.5) is in large part the same as Eq. A2 of E95a, but ψ has been broken into two components, the mid-troposphere streamfunction ψ and the deep convective mass flux G, which is somewhat in line with the definitions provided in E89 and closely matches the coded representation. While D_b is necessary to prevent total collapse of the eyewall (E89), the primary balance at pseudo steady state (Fig. 4.3) near the eyewall is between the inward horizontal requirement for mass from exterior radii to maintain deep convection ($G < 0$) and the loss of angular momentum due to friction ($\psi_{\text{Ekman}} > 0$). At larger radii, where the surface wind speeds (and thus frictional losses of angular momentum) are weaker, the environmental return flow (ψ) is the important supply of mass for the boundary layer.

Non-steady behavior

Summary information for Simulation *DoubleRes* is shown in Fig. 4.4, along with the surface radii of each R-grid point as a function of time in Fig. 4.5. The model behaves differently with a doubling of the resolution. With increased resolution, the time at which the most intense winds is reached is delayed (day 13 vs. day 10), the maximum winds and minimum central pressure become less intense with time, the RMW expands, and these simple model characteristics become noisy. The radii of model grid points during contraction is similar between both simulations (Figs. 4.2 and 4.5 before day 10), with an early outward movement followed by a smooth concentration

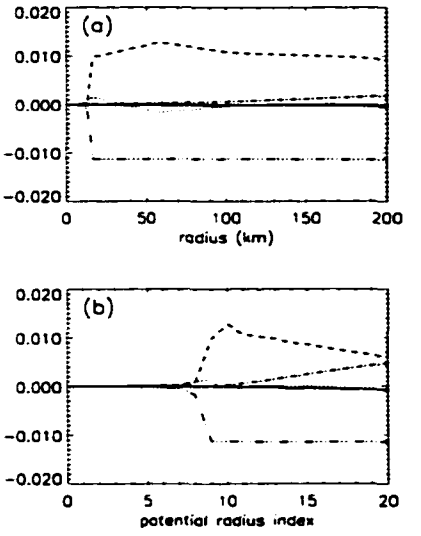

FIGURE 4.3: Budget of surface angular momentum at pseudo-steady state, shown for Simulation *Default* at day 19. Shown are the total budget (heavy, solid line), G (dash, triple dot), ψ_{Ekman} (dashed), ψ (dash, dotted), and D_b (dotted). (a) Plotted versus physical radius r. (b) Plotted versus potential radius grid index.

and contraction of grid points that form the eyewall. The contraction of the eyewall grid points is mimicked by similar inward motions of environmental grid points. Another phenomenon is the apparent "pairing" of environmental grid points, for example grid points labeled 9 and 10 prior to day 10 in Simulation *Default* (Fig. 4.2) and of grid points 17-18, 19-20, and 21-22 in Simulation *DoubleRes* prior to day 12. This pairing behavior is so robust that pairing reestablishes itself after events occur that disrupt earlier pairings. For example, during contraction in Simulation *Default* (Fig. 4.2), grid point 10 is paired with grid point 9, but between 10 and 15 days grid point 10 pairs with grid point 11. Similar behavior is seen in Simulation *DoubleRes* with grid point 21.

Non-steady behavior was noted by E95, noting the appearance of "multiple eyewalls when the initial relative humidity of the troposphere is high" and the gradual outward expansion of the eyewall with time, as shown here in Simulation *DoubleRes* (Fig. 4.4c). We note here that this is associated with a gradual weakening of peak tangential winds in the storm and accumulation of angular momentum in the eyewall (Fig. 4.5) as environmental grid points augment the bundle of eyewall grid points. The pairings of grid points in the environment are associated with enhancements in tangential wind and vorticity between the two grid points, as can be seen from (4.1). The radius, r, changes only slightly between the two grid points in the pair, but R, increases by a fixed amount, therefore V may increase. Profiles of tangential wind and vorticity for Simulation

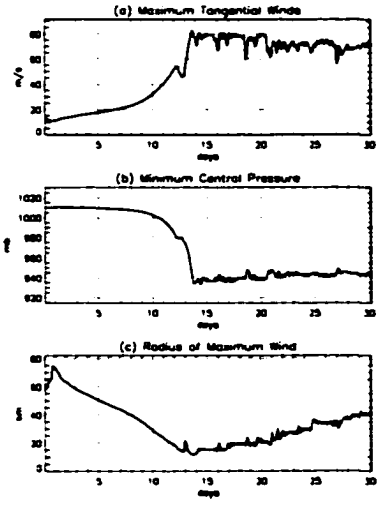

FIGURE 4.4: (a) Peak tangential winds, (b) minimum central pressure, and (c) radius of peak winds as a function of time for Simulation *DoubleRes*.

DoubleRes (Fig. 4.6) and contours of vorticity versus radius and time (Fig. 4.7) verify this interpretation, although in terms of tangential wind the effect is subtle. These pairings can further be interpreted as "secondary eyewalls", as seen by the enhancements of deep convective mass flux located at the grid point at the outer edge of each vorticity enhancement (Figs. 4.8 and 4.9). The deep convective mass flux displayed here is derived from G in (4.5), except that the radial gradient is taken (to measure the local effect on this integrally defined quantity) and is divided by the area between two adjacent grid points (to provide a density measure).[3]

A further doubling of NR (Simulation *QuadRes*) leads to a model storm that does not contract and intensifies slowly (Fig. 4.10). The peak tangential wind in the storm is ~ 20 m s^{-1} less than that of Simulations *Default* or *DoubleRes*. A typical profile of tangential winds and vorticity from this simulation (Fig. 4.11) indicates a nearly wind-free eye with a sharp transition to the strong winds of the eyewall (much like Simulation *DoubleRes*). In terms of two-dimensional nondivergent vorticity dynamics in the horizontal plane (e.g., Michalke and Timme 1967; Schubert et al. 1999), such an arrangement is likely unstable, leading to a redistribution of eyewall vorticity throughout the eye. Emanuel (1997) suggests the importance of the radial redistribution of angular momentum in

[3]The latter operation does not greatly change the character of the display, but is included to help aid the interpretation of the variable.

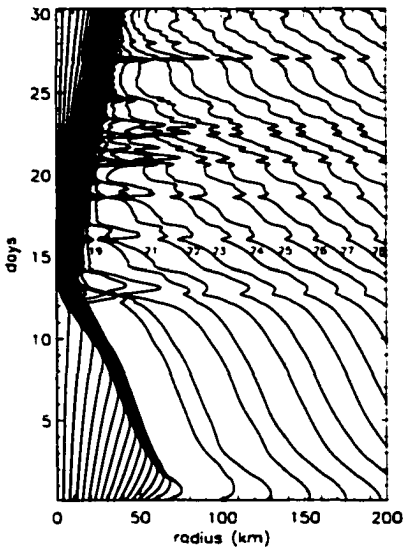

FIGURE 4.5: Surface radial position of each model grid point (R-coordinate, i.e. contours of constant angular momentum) as a function of time for Simulation *DoubleRes*. Numbers within the plot label well-spaced grid points by index number, with the zeroth index being the invariant boundary grid point at $r = 0$.

the eye for enhancing pressure falls within a hurricane. This in part makes the inclusion of subgrid-scale diffusion mandatory in the E95a model since it is axisymmetric and is unable to resolve the horizontal instability. The diffusion as modeled, though, will act on the scale of the grid separation (which is quite small in the eyewall) rather than the scale of eye itself, as shown in Schubert et. al (1999).

Regime transitions

Emanuel (1995a) suggests that it is possible to realize the non-steady model behavior by increasing the initial relative humidity of the troposphere. As we have shown, this type of model behavior can also be realized by changes in horizontal resolution. This subsection explores the identifiability and existence of these two types of behavior (pseudo-steady and non-steady) as a function of a numerical parameter (model resolution) and of a physical parameter (sea surface temperature: SST: see Table 4.4). All other input parameters are the same as in Table 4.1, except for the time step, which, as mentioned in Section 4.2 is selected to be a sufficiently small value (10 s).[4]

[4]The outflow temperature is also held constant, despite the strong observed relationship with surface temperature noted by DeMaria and Kaplan (1994a).

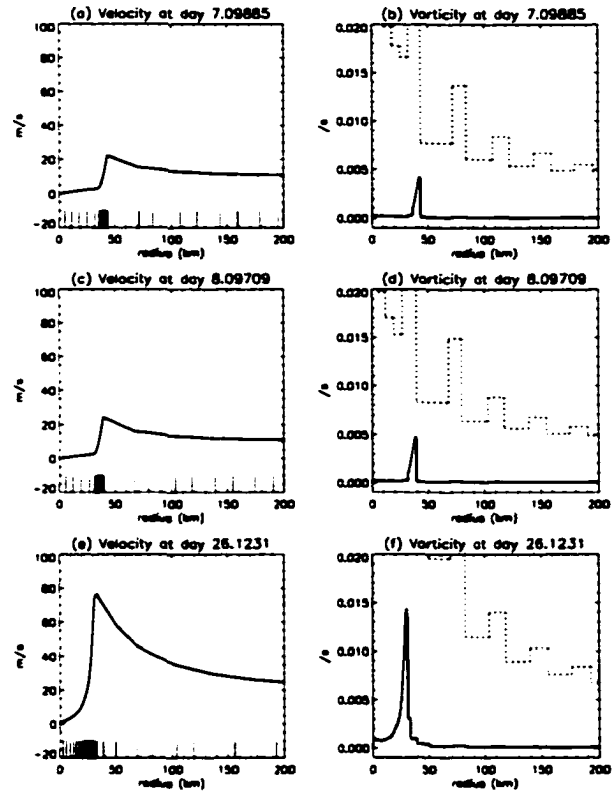

FIGURE 4.6: Profiles of tangential wind and vorticity for Simulation *DoubleRes* at 7, 8, and 26 simulation days. The positions of radial grid points are overlaid as ticks in (a), (c), and (e). The vorticity is computed as the circulation between adjacent grid points divided by the area of the annulus between these grid points. The same vorticity curve multiplied by 100 is overlaid with the dotted line in (b), (d), and (f).

Two measures suggest themselves from Section 4.3.1 to distinguish the two different regimes: the variance of V_{max} and the variance of RMW during the last 10 simulation days. While the "steady" behavior shown above for Simulation *Default* displays an occasional "anomaly", the variance of the two suggested variables tend to be much smaller than that for the non-steady simulation (Fig. 4.12). There do exist two identifiable regimes of model behavior in terms of low-variance and high-variance regimes, and that the transition between these regimes has a dependence on both model resolution and SST. Direct inspection of the evolution of surface radii of model grid points (Fig. 4.13) for a subsample of *SensExp* provides a complicated picture, but generally supports the interpretation that the two regimes identified with variance measures are the same regimes identified in Section 4.3.1. By variance measures, we would identify the $NR = 42$ and 58 simulations to be "steady" regime simulations at 26.5 C SST. The $NR = 42$ simulation has an anomaly after the initial contraction of the eyewall, similar to that in Fig. 4.2 for Simulation *Default*. The

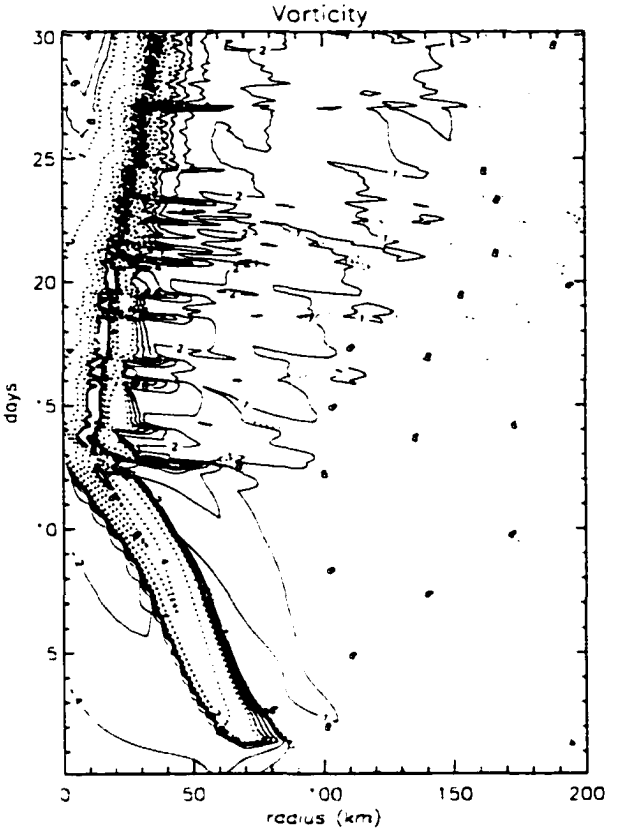

FIGURE 4.7: Surface vorticity as a function of radius and time for Simulation *DoubleRes*. The value of vorticity is computed from the circulation as in Fig. 4.6, with the value simply applied to the midpoint between the two grid points. The heavy, solid contours are [1, 2, 4, 6, 8] $\times 10^{-2}$ s^{-1}. The heavy, dotted contours are [1, 2, 4, 6, 8] $\times 10^{-3}$ s^{-1}. The light, solid contours are [1, 2, 4, 6, 8] $\times 10^{-4}$ s^{-1}. The light, dotted contours are [1, 2, 4, 6, 8] $\times 10^{-5}$ s^{-1}.

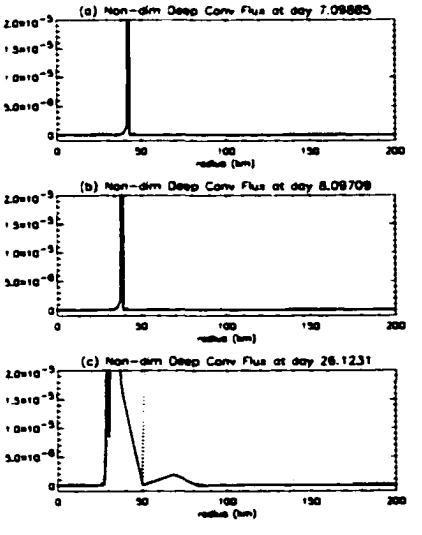

FIGURE 4.8: Profiles of the non-dimensional deep convective mass flux for Simulation *DoubleRes* at 7, 8, and 26 simulation days. The same curve multiplied by 100 is overlain with the dotted line.

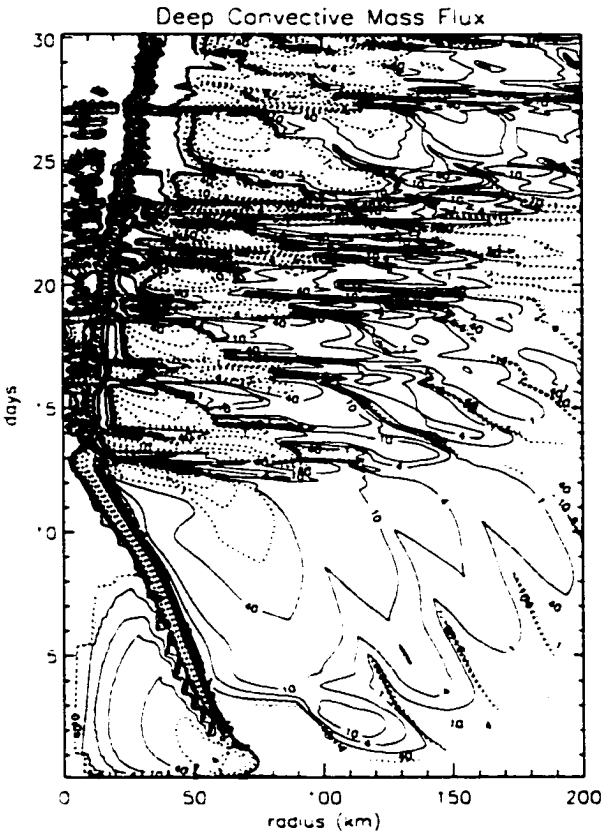

FIGURE 4.9: Non-dimensional deep convective mass flux (normalized by area) as a function of radius and time for Simulation *DoubleRes*. The heavy, solid contours are [1, 4, 10, 40] $\times 10^{-5}$. The heavy, dotted contours are [1, 4, 10, 40] $\times 10^{-7}$. The light, solid contours are [1, 4, 10, 40] $\times 10^{-9}$. The light, dotted contours are [1, 4, 10, 40] $\times 10^{-11}$.

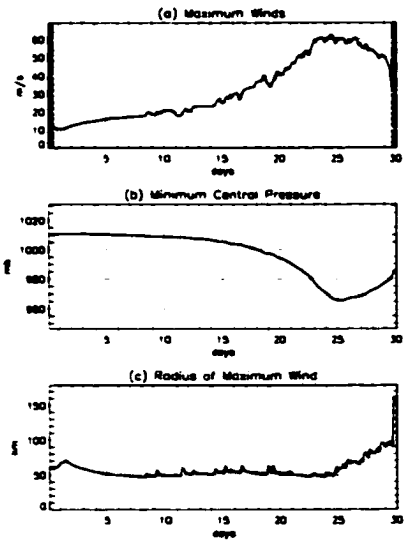

FIGURE 4.10: (a) Peak winds, (b) minimum central pressure, and (c) radius of peak winds as a function of time for Simulation *QuadRes*.

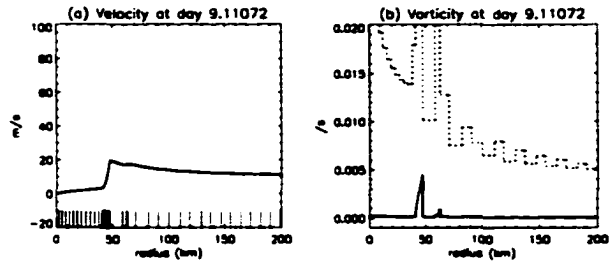

FIGURE 4.11: Profiles of (a) tangential winds and (b) vorticity at 9 simulation days from Simulation *QuadRes*.

TABLE 4.4: The values of altered parameters used in *SensExp*.

sea surface temperature (T_s; C)	25.0, 26.0, 26.5, 26.9, 27.0, 27.1, 27.5, 28.0, 29.0
number of radial nodes (NR)	25, 28, 30, 32, 34, 36, 38, 40, 42, 44, 45, 46, 47, 48 49, 50, 51, 52, 53, 54, 55, 56, 58, 60, 62, 64, 66, 68 70, 72, 75, 80, 85

$NR = 58$ simulation is an example of a "steady" regime simulation without an anomaly. We would identify the $NR = 60$ simulation as the first simulation in the "non-steady" regime, followed by the $NR = 62$, 64, and 75 simulations also within the "non-steady" regime. At $NR = 60$, the vortex goes through an initial smooth contraction, followed by steady behavior until day 27. The evolution that occurs at this time bears some similarities to the "anomaly" in the $NR = 42$ simulation in that environmental grid points are newly associated with the primary eyewall "bundle", that the eyewall shifts outward as a result of this event, and that all the exterior environmental grid points shift inward to maintain a somewhat fixed separation from each other and from the eyewall. For the $NR = 60$ case, though, more than one environmental grid point is newly associated with the eyewall bundle. In $NR = 62$ and 64 simulations the onset of non-steady behavior has a similar form and occurs at an earlier time in the simulation as NR increases. For this reason, we cannot discount that a similar onset will occur at lower resolution if the simulation were carried out to a

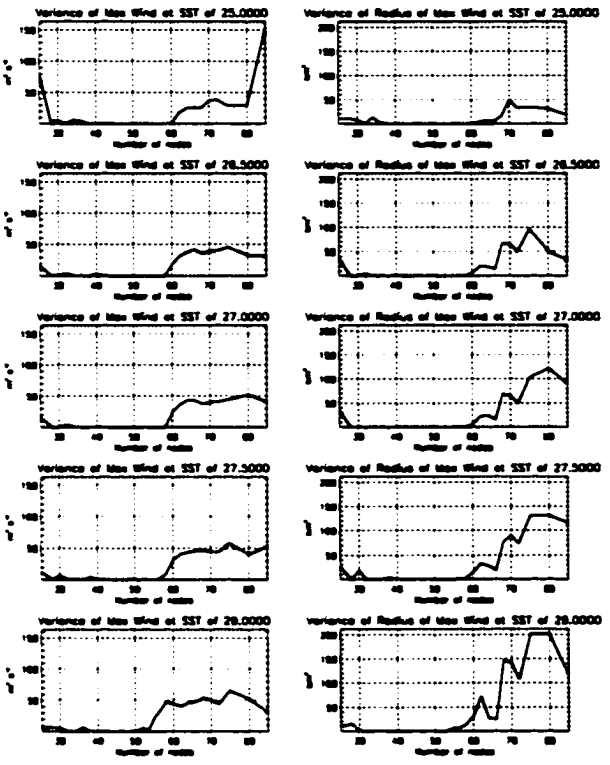

FIGURE 4.12: Variances of maximum tangential winds and of radii of maximum tangential winds from day 20 to day 30 for a sample of simulations in *SensExp*.

long enough time.[5] Examination of the $NR = 75$ simulation shows that onset here still maintains the similar form occurring at earlier time, but also that the "similar form" is becoming constrained in the radial direction as NR increases. For example, the last "wiggle" on day 28 of the $NR = 60$ simulation near $r = 180$ km can now be identified with a similar "wiggle" on day 15 of the $NR = 75$ simulation near $r = 150$ km. For a given SST, the peak in maximum tangential winds shows a sensitivity of between 10 and 15 m s^{-1} (Fig. 4.14) simply as a function of regime transition. E-MPI for the 27 C SST cases is 74.8 m s^{-1}, so the apparent level storm intensities seen in the non-steady regime ($NR > 60$) and at moderate resolution in the steady regime ($NR \sim 40$) exceed this by 5 m s^{-1} or about 10 kts. While these two selections of resolution might appear natural because

[5] A similar behavior as resolution is increased occurs in the "steady" regime with the timing of anomalies. A very long simulation of Simulation *Default*, though, shows no further anomalies until the ultimate demise of the vortex after day 80. This demise of the vortex has similar qualities to the last couple days of Simulation *QuadRes*. The model failed shortly after day 80.

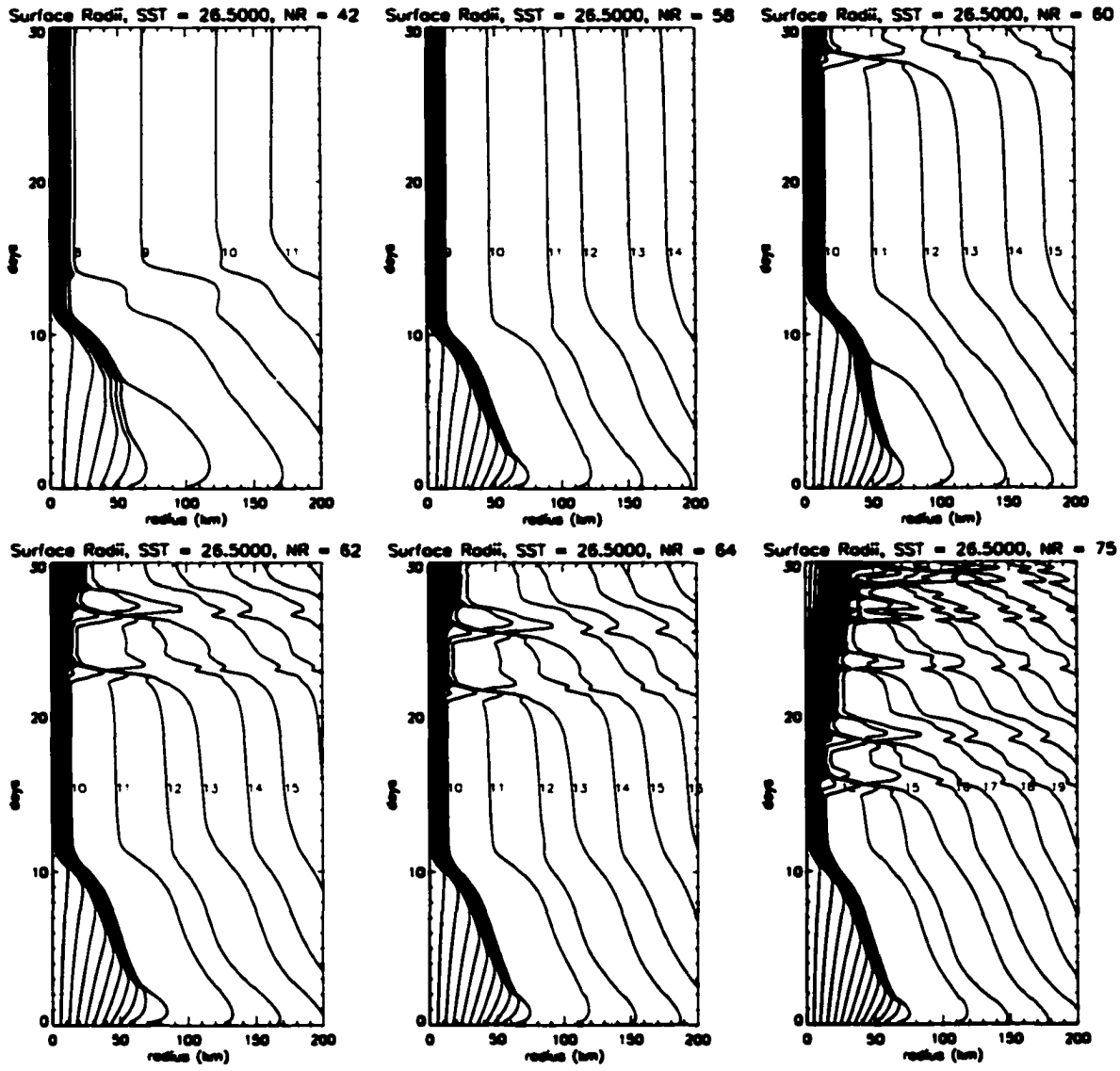

FIGURE 4.13: Surface radii of model grid points from the *SensExp* at 26.5 C SST and for 42, 58, 60, 62, 64, and 75 grid point simulations.

they exist in areas of numerical consistency, they are also those selections of resolution that are in greatest disagreement with E-MPI.

4.3.2 Environmental deep convection

It was noted by E89 that high precipitation efficiency convection would occur after a certain time in the simulation outside the eyewall and would "lead to an expansion and weakening of the wind field." As noted in Section 4.3.1, there exists deep convection outside of the eyewall associated

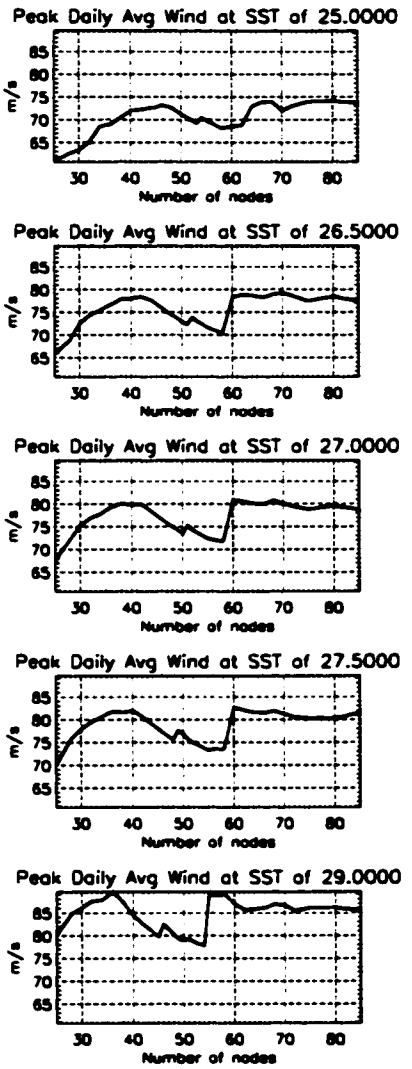

FIGURE 4.14: The peak in each simulation of the daily running means of maximum tangential winds for a sample of simulations in *SensExp*.

with the secondary eyewalls. In addition, there is the development of deep convection at further radii at later times in both Simulation *Default* and Simulation *DoubleRes* (Figs. 4.15 and 4.16). Unlike Fig. 4.9, because of the large range in radii, the radial grid point number is used on the abscissa, and because of the large dynamic range in values of deep convective mass flux when it is normalized by area, it is displayed here without that normalization. The meaning of such a convective flux without the normalization is then (from Eq. 4.5) as an amount of differential forcing between two grid points of the square of the boundary layer radius of the grid points, i.e.,

$$\frac{\partial}{\partial \bar{\tau}} \frac{\partial \bar{r}_b^2}{\partial \bar{R}} \sim \frac{\partial \bar{\psi}}{\partial \bar{R}} - \frac{\partial \bar{G}}{\partial \bar{R}}. \tag{4.6}$$

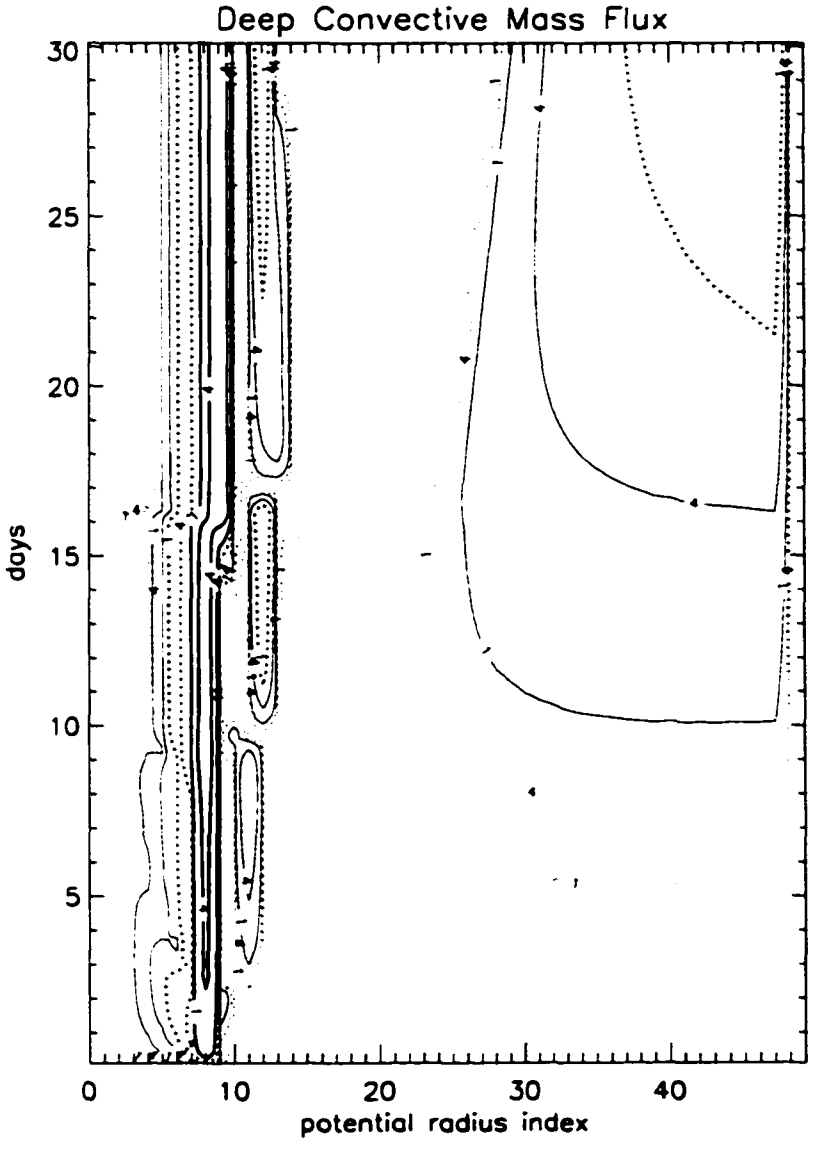

FIGURE 4.15: Non-dimensional deep convective mass flux as a function of grid point index in the radial direction and time for Simulation *Default*. The heavy, solid contours are [1, 4] $\times 10^{-3}$. The heavy, dotted contours are [1, 4] $\times 10^{-4}$. The light, solid contours are [1, 4] $\times 10^{-5}$. The light, dotted contours are [1, 4] $\times 10^{-6}$.

Therefore, the existence of a positive value of this forcing will (once the minus sign is applied) either draw every exterior grid point inward or be balanced by descending air implied by ψ. Since the outer most grid point is at a fixed radius and the forcing occurs directly up to the grid point interior to the outer boundary, this forcing requires compensation by broad-scale descent, yet it is not immediately obvious why the presence of a hurricane should require convection at a great distance from the hurricane.

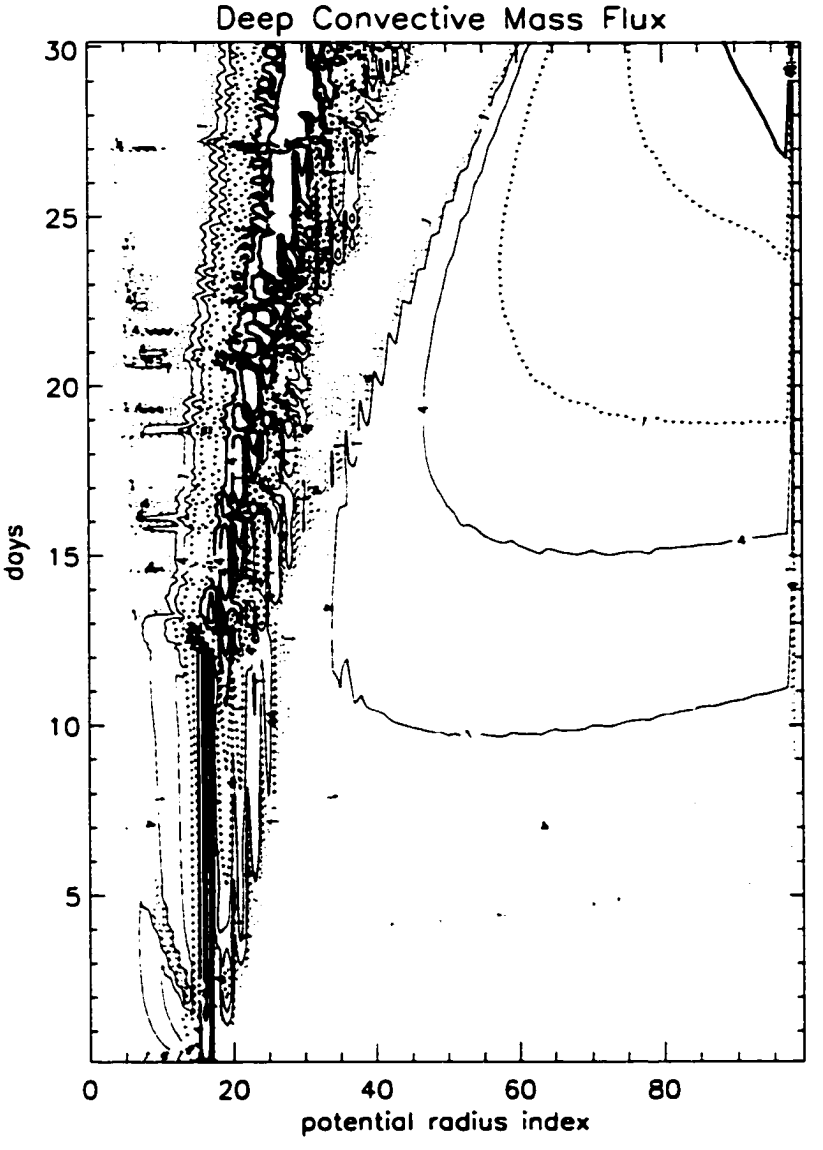

FIGURE 4.16: Non-dimensional deep convective mass flux as a function of grid point index in the radial direction and time for Simulation *DoubleRes*. The heavy, solid contours are [1, 4] $\times 10^{-3}$. The heavy, dotted contours are [1, 4] $\times 10^{-4}$. The light, solid contours are [1, 4] $\times 10^{-5}$. The light, dotted contours are [1, 4] $\times 10^{-6}$.

If convection is artificially suppressed everywhere exterior to the eyewall, Simulation *DoubleRes* will become nearly-steady after the initial contraction, as is shown in Simulation *DoubleResConv* (Figs. 4.17 and 4.18). The process for suppressing convection was indiscriminate between the secondary eyewall features in the near vicinity ($r < 200$ km) of the eyewall and the broad region of convection noted at very far distance, therefore the effects of the two apparently distinct phenomena cannot be separated in this experiment. There is one "anomaly" within Simulation *DoubleResConv* near day 21 that is more similar to that within Simulation *DoubleRes* than in Simulation *Default*,

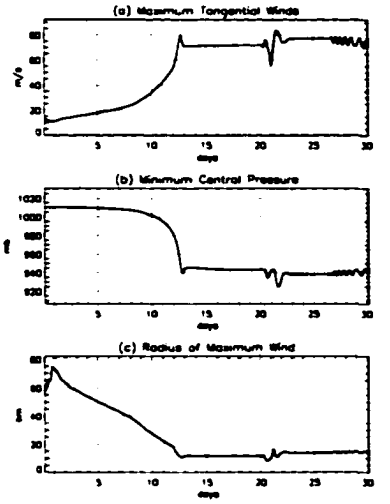

FIGURE 4.17: (a) Peak tangential winds, (b) minimum central pressure, and (c) radius of peak winds as a function of time for Simulation *DoubleResConv*.

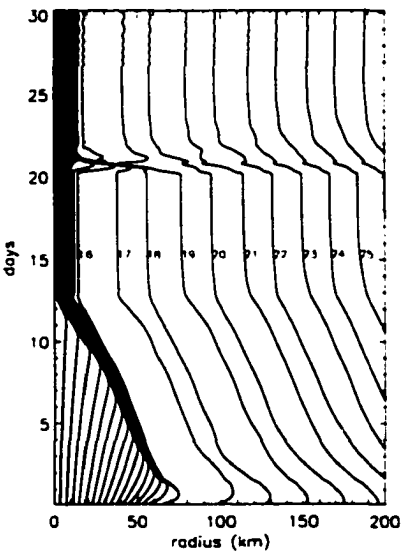

FIGURE 4.18: Surface radial positions of each model grid point (R-coordinate, i.e. contours of constant angular momentum) as a function of time for Simulation *DoubleResConv*. Numbers within the plot label well-spaced grid points by index number, with the zeroth index being the invariant boundary grid point at $r = 0$.

because two environmental grid points are newly absorbed into the eyewall. This is not an onset of non-steady behavior in Simulation *DoubleResConv* as it is in Simulation *DoubleRes*, implying that the non-steadiness is caused by a feedback with convection outside of the eyewall. A wavelike pattern is apparent after day 26, but we are not prepared to speculate upon its nature. By comparing Figs. 4.17 and 4.1, we can see that the effect of suppressing convection outside of

	DoubleRes	$l \times 2$	$l/2$
5th day V_{max}	17.8 m s^{-1}	15.9	19.6
10th day V_{max}	32.6 m s^{-1}	23.2	27.3
intensification rate day 0 to 5	0.88 m $s^{-1}d^{-1}$	0.50	1.24
intensification rate day 5 to 10	2.96 m $s^{-1}d^{-1}$	1.46	1.54
onset of non-steadiness	12.3 days	11.4	12.7
V_{max} at onset	54.8 m s^{-1}	27.6	34.6

TABLE 4.5: Results from experiments with modified diffusive mixing length. The onset of non-steadiness is defined as the time when the monotonic increase in storm maximum tangential winds is interrupted.

the eyewall on the pseudo-steady state storm is quite small in V_{max} ($\sim$ 5 m s^{-1}) and minimum central pressure ($\sim$ 10 mb).

4.3.3 Modifications of diffusion

It was noted by E89 that "the model is not particularly sensitive to the length scale used in the ad hoc eddy viscosity" in the model integrations, but E89 did note that there is an effect on the timing of intensification. Curiously, the effect of the length scale l was not monotonic in E89, with the intermediate (default) value selected for l leading to the most rapid intensification, while a value of mixing length either larger or smaller both lead to a delay in intensification. A similar result is found here with Simulation *DoubleRes*, where the default value for l provided for a quicker intensification than with $l \times 2$ or $l/2$. Based on the results of Section 4.3.1, we can interpret Simulation *DoubleRes* as being a case where the onset of non-steady behavior occurs before the initial "smooth" contraction of the vortex is complete (Fig. 4.5; day 12). Table 4.5 shows the results of a sensitivity test versus mixing length on a set of outputs from the model that may be useful in making an operational hurricane forecast. The onset of non-steadiness between the three simulations is nearly the same, within about a day of each other, but by this time Simulation *DoubleRes* has twice as fast V_{max} as when the l is doubled and is significantly stronger than when the l is halved. It is pointed out in E89 that the "crude deformation-based mixing" is "far from realistic", but we have to agree that it is to the credit of the E89/E95 model that the eventual maximum tangential winds and central pressure are reasonably insensitive to the choice of a tunable parameter within the diffusion scheme. However, the application to a forecast problem would require accuracy of the forecast on a given day, thus a physical justification for the selection of the diffusion is required.

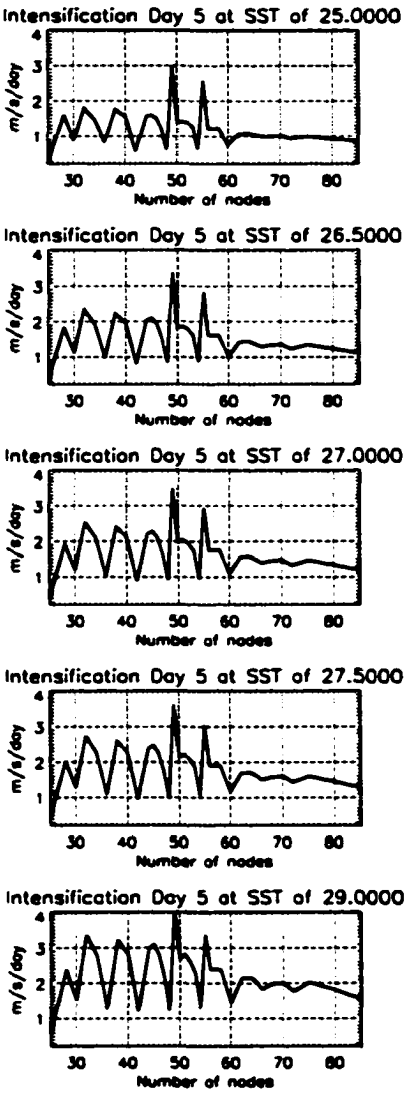

FIGURE 4.19: Intensification during 5 day of simulations from *SensExp*. Intensification is determined from the average of one-day intensification rates from day 3.5 to 4.5 to day 4.5 to 5.5.

4.3.4 Sensitivity to the initial vortex

The intensification rate on the 5th simulation day from *SensExp* is shown in Fig. 4.19. Note that a pattern appears as a function of model resolution that is largely independent of SST. For example, the peak intensification rate for day 5 occurs at $NR = 49$ at all SST. The sensitivity displayed here is strongly influenced by the specification and sensitivity to resolution of the initial vortex. From Fig. 4.20, we can infer intensification rate from the slope (versus time) of the eyewall bundle since RMW is found there while any given grid point has a fixed angular momentum. The intensification rate appears to be slowed by the proximity of the first environmental grid point to

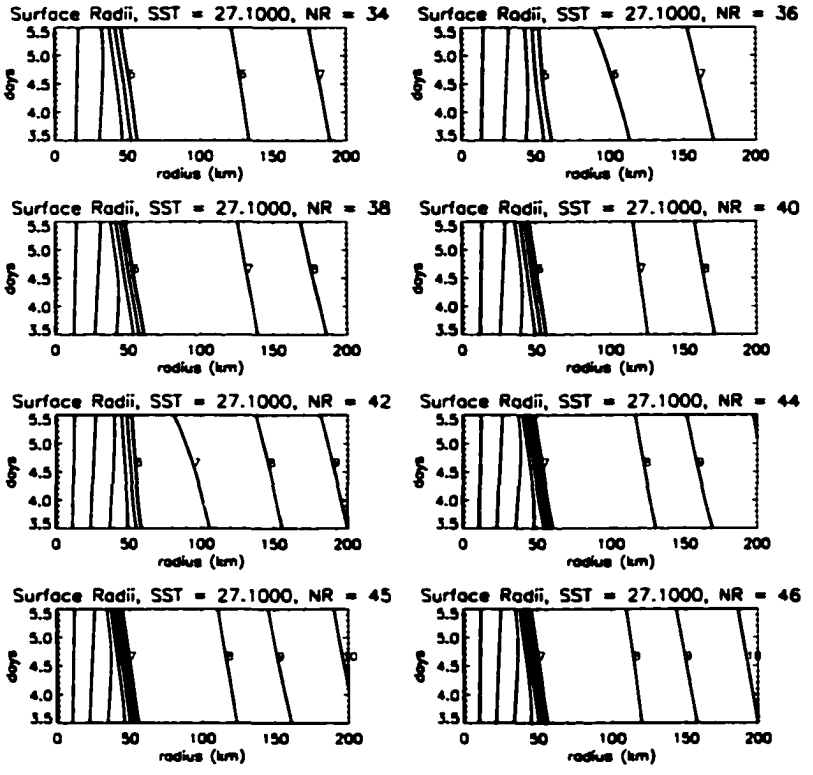

FIGURE 4.20: Surface radial positions for model grid points as a function of time from day 3.5 to 5.5 for a sample of simulations from *SensExp*.

the eyewall. Viewed as a function of increasing resolution, just before an additional grid point is about to be initialized inside the initial RMW, the first environmental grid point is closest to the eyewall. For example, at $NR = 40$, intensification is 2 m $s^{-1}d^{-1}$ with grid point 6 at the outer edge of the eyewall and grid point 7 about 70 km exterior to the eyewall. The situation is much the same at $NR = 44$, except that the last eyewall grid point and first environmental grid point are increased by one. At $NR = 42$, however, the intensification is less than 1 m $s^{-1}d^{-1}$ and the first environmental grid point is approaching the eyewall, approximately 40 km exterior to the eyewall. At resolutions greater than $NR = 60$, the impact of this sensitivity is less evident, but still apparent.

4.4 Conclusions

We have shown two different types of behavior in the E95a model that is largely a function of model resolution. Transition between steady and non-steady behavior can be associated with a

10 to 15 m s^{-1} change in modeled storm intensity. Intensification rate on a given date can vary strongly with the mixing length and model resolution.

These behaviors of the model would each argue against deployment of the E95a/E99 model for operational forecasting. Is the more appropriate view of a hurricane under uniform, benign environmental conditions that of a constant intensity, RMW, and eyewall angular momentum or of gradual expansion of the eye, slow spin down, and gradual accumulation of environment angular momentum? While real hurricanes do not persist under such conditions for many days, as in these simulations, it is important to run the model to access the correct regime of behavior. Is a model forecast error up to 15 m s^{-1} acceptable in a forecast setting, absent a definitive choice of behavior for the model, mixing length, or resolution?

Despite many remarkable properties of the E95a model, namely the ability to spin up a hurricane in the absence of any convective instability in the environment and the near confirmation of E-MPI (± 5 m s^{-1}), we cannot recommend deploying the E99 model for operational forecasting until the issues raised above are addressed. The RE87 model can play a role in this investigation, as well as the E99 model. The E99 model could be deployed as a forecast aid in a very cautionary manner, though, mindful of the exposed sensitivities. The most effective application might be in applying the model in an ensemble fashion to examine the relative sensitivity of hurricane intensity to varying degrees of track error. Fully three-dimensional simulations (such as the GFDL Hurricane Prediction System examined in Chapter 2) would take a large amount of computer time relative to the E99 model. In this operating mode, one might be more encouraged by relative differences between different elements in the ensemble rather than the absolute storm intensity implied by these results, and be alert to track errors that might lead to more rapid intensifications and thus threats to land and to marine interests.

Chapter 5

HURRICANE SUPERINTENSITY

In Chapter 4, we saw that with minor changes in numerical parameters of the simple E95a axisymmetric hurricane model the modeled storm intensity may change by upward of 10 m s^{-1}. In Chapter 3, we reviewed a concept for predicting the equilibrium intensity of hurricanes. Since E-MPI theory is constructed in an axisymmetric context, whatever any reservations one might have in applying it to real storms, it *should* be well-positioned to model the equilibrium, steady-state intensities of axisymmetric model hurricanes. Many simulations using the E95a model did exceed the MPI. But as we will see shortly, the behavior of the RE87 model at high resolution is to *greatly* exceed E-MPI. This repeats the finding of Hausman (2001) using an entirely different axisymmetric model. Because the model behaves for one set of parameters in close adherence of the assumptions of and the result of E-MPI, we have an opportunity to examine the new physics that allow high-resolution simulations to exceed E-MPI. This chapter will expose the role of entropy addition from the eye to the eyewall in allowing the model storm to exceed E-MPI.

5.1 The RE87 model reviewed

The Rotunno and Emanuel (1987; RE87) hurricane model is an axisymmetric, two-dimensional, non-hydrostatic, cloud-resolving version of the Klemp and Wilhelmson (1978) formulation originally developed for the study of cumulus clouds and supercell dynamics. This was kindly provided to us by R. Rotunno of the National Center for Atmospheric Research. The model is integrated on a staggered C-grid using a fixed radial and fixed vertical grid spacing. There is no ice in the model and explicit convection is used with a fixed precipitation fall-speed of 7 m s^{-1}. Subgrid-scale turbulence is performed using a Smagorinsky (1963) formulation modified to allow a variable mixing length, a function of the local stability using a Richardson number formulation following Lilly (1962). Radiation is crudely represented by Newtonian cooling that attempts to restore the local potential

temperature to that found initially in the ambient environment. In the numerical experiments presented here the radiational heating/cooling rate is capped at 2 K day^{-1}. Sponge layer damping occurs above the model tropopause ($z > 19.4$ km). The outer boundary at $r = 1500$ km is open. Surface interaction is through a standard bulk aerodynamic parameterization. The surface drag coefficient C_D is represented by a linear function of wind speed using Deacon's formula (Roll, 1965). The surface enthalpy exchange coefficient C_k is set equal to the drag coefficient ($C_k/C_d = 1$). The u- and w-fields are computed using a "fast" time step to handle sound waves. All of these processes are unchanged from that described in RE87. The initial thermodynamic sounding of the environment is created by a procedure described in RE87 as a modification of the Jordan (1958) sounding so that it is neutral to convection as realized in the model.

The principle equations of the model are as follows. Radial momentum is evolved by

$$\frac{du}{dt} - \left(f - \frac{v}{r}\right) v = -c_p \bar{\theta}_v \frac{\partial \pi}{\partial r} + D_u \tag{5.1}$$

where u is the radial velocity, v is the tangential velocity, f is the Coriolis parameter, θ_v is the virtual potential temperature, and the overbar refers to variables at the ambient initial base state which are a function of z only. The subgrid scale diffusive forcings are represented by D_u. The pressure perturbation variable π is defined by Klemp and Wilhelmson (1978) as

$$\pi + \bar{\Pi} = \Pi \tag{5.2}$$

where

$$\Pi = \left(\frac{p}{p_0}\right)^{R_d/c_p} = \left(\frac{R_d}{p_0}\rho\theta_v\right)^{R_d/c_p} = \frac{T}{\theta} \tag{5.3}$$

is the nondimensional pressure. The density is denoted by ρ and p_0 is a reference pressure (1000 mb). Temperature T is not evolved in the model but is diagnosed from (5.3). The tangential momentum equation is

$$\frac{dv}{dt} + \left(f + \frac{v}{r}\right) u = D_v \tag{5.4}$$

where D_v is the subgrid scale forcing of v. The vertical momentum equation is

$$\frac{dw}{dt} = -c_p \bar{\theta}_v \frac{\partial \pi}{\partial z} + D_w + g\left\{\frac{\theta - \bar{\theta}}{\bar{\theta}} + 0.61\left(q_v - \bar{q}_v\right) - q_l\right\} \tag{5.5}$$

TABLE 5.1: Default run settings.

number of radial v-points	$NR = 100$
number of vertical v-points	$NZ = 20$
outer boundary	$R_O = 1500$ km
upper boundary	$z_{top} = 25 \times 10^3$ m
radial grid spacing	$\Delta r = R_O/NR = 15$ km
vertical grid spacing	$\Delta z = z_{top}/NZ = 1250$ m
first sponge layer grid level	$I_{z_{spn}} = 16$
simulation run time	$t_{end} = 30$ days
time step (long)	$\Delta t = 20$ s
time step (short)	$\Delta t_s = \Delta t/5 = 4$ s
Coriolis parameter	$f = 5 \times 10^{-5}$ s^{-1}
coefficient of drag at $V = 0$	$C_{D_0} = 1.1 \times 10^{-3}$
ratio of coefficients of exchange	$\frac{C_k}{C_D} = 1.00$
"total" mixing length	$l = 200$ m
"horizontal" mixing length	$l_h = 0.2 \times \Delta r = 3$ km
initial V_{max}	15.0 m s^{-1}
initial radius of max winds	RMW$_i$ = 82.5 km
initial outer radius of vortex	$r_{o_i} = 412.5$ km
initial ocean potential temperature	$\theta_{s_i} = 298$ K
ambient surface pressure	$p_{amb} = 1015.1$ mb
ocean temperature	$T_s = 299.2$ K = 26.13 C

where θ is potential temperature, q_v is the vapor mixing ratio, and q_l is the liquid mixing ratio. The conservation of mass is

$$\frac{\partial \pi}{\partial t} + \frac{\bar{c}^2}{c_p \bar{\rho} \bar{\theta}_v^2} \left\{ \frac{1}{r} \frac{\partial r u \bar{\rho} \bar{\theta}_v}{\partial r} + \frac{\partial w \bar{\rho} \bar{\theta}_v}{\partial z} \right\} = 0 \tag{5.6}$$

where c here is the speed of sound. The thermodynamic relationship is

$$\frac{d\theta}{dt} = M_\theta + D_\theta + R \tag{5.7}$$

where M_θ is the microphysical source (sink) term for θ due to condensation (evaporation). The diffusion of heat occurs through D_θ, and R is the radiational term and is generally negative except when a grid point is cooler (in terms of θ) than the initial ambient sounding.

Model parameters used in the default run are summarized in Table 5.1. These are the same as Experiment A in RE87 except there the initial $V_{max} = 12$ m s^{-1}, the sea surface temperature (SST)

TABLE 5.2: Parameter changes with each doubling of resolution.

Manual Changes
$2 \times NR$
$2 \times NZ$
2× number of time steps to perform
$1/2 \times \Delta t$
$2 \times I_{z_{spn}}$
interpolate the ambient potential temperature sounding
interpolate the ambient moisture sounding
Automatic Changes
$1/2 \times \Delta r$
$1/2 \times \Delta z$
$1/2 \times \Delta t_s$
$1/2 \times l_h$

is 26.3 C. and the radiational cooling is uncapped.[1] Table 5.2 summarizes the changes in the model that occur for each doubling of the resolution. Simulations will be referred to as the "default run", "2x run", "4x run", and "8x run" with each doubling of radial, vertical, and temporal resolution. For the presentation of results, days (8.64×10^4 s) are used, with the simulations starting at day 0. Figure 5.1 shows that the 4x run produces a realistic hurricane vortex like Figure 5 of RE87, except that it is more structured and much more intense, possessing stronger updrafts.

5.1.1 A note on θ_e

Moist entropy is conserved under moist adiabatic ascent since phase changes represent reversible exchanges of energy between a latent potential of vapor and internal energy of the mixed gases of air. It is necessary for this chapter to use a form of equivalent potential temperature that the model conserves (RE87, p. 544)

$$\Theta_e = \theta + \frac{L}{c_p}\frac{\theta}{T}q_v. \tag{5.8}$$

[1] Note that the cooling used here is that found in Experiment J (2 K day^{-1}) of RE87. This experiment was found by RE87 to have overall structure similar to Experiment A (their control; unbounded cooling) and was 5 m s^{-1} more intense than Experiment A. RE87 found these intensity changes to be consistent with MPI theory because of changes in T_{out}.

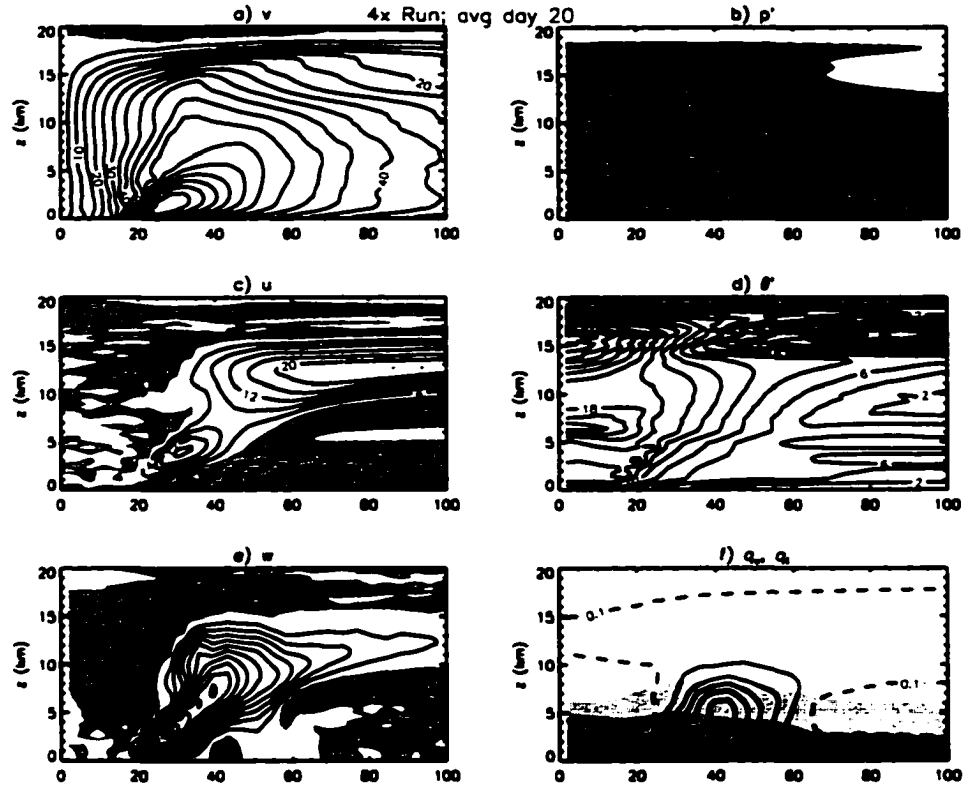

FIGURE 5.1: The 20.0-21.0 day average fields in the 4x run near the eyewall. All shaded regions indicate negative values of the field. (a) Tangential velocity, contour interval, 5 m s^{-1}; (b) dimensional pressure deviation from the outer boundary (at 1500 km radius), contour interval, 5 mb; (c) radial velocity, contour interval, 4 m s^{-1}; (d) potential temperature deviation from the initial state, contour interval, 2 K; (e) vertical velocity, contour interval, 0.5 m s^{-1}; (f) liquid water mixing ratio, contour interval, 1 g kg^{-1}; dashed line denotes the 0.1 g kg^{-1} contour, and water vapor mixing ratio; lightest shading indicates $3 < q_v < 8$ g kg^{-1}, darker shading indicates $8 < q_v < 13$ g kg^{-1}, and darkest shading indicates $q_v > 13$ g kg^{-1}.

This form of θ_e is used throughout this chapter where RE87 results are concerned, and underestimates the commonly used exponential form (e.g., Holton 1992)

$$\theta_e = \theta \exp\left(\frac{Lq_v}{c_p T}\right) \tag{5.9}$$

by up to 10% of the magnitude of the last term of (5.8), or to 5 K near the ocean surface due to large q_v.

5.2 "Superintensity"

The characteristic of axisymmetric hurricane models to simulate more intense storms with increasing model resolution was reviewed by Hausman (2001) and was supplemented by his own sim-

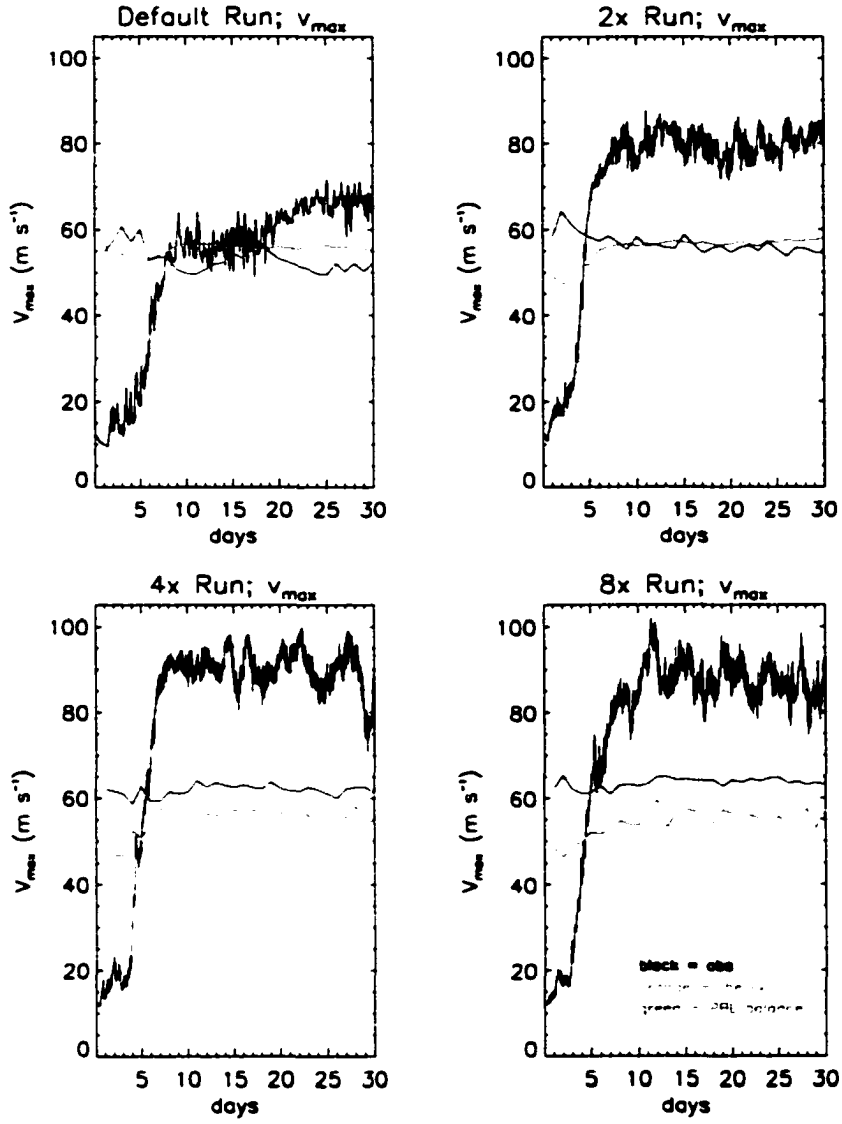

FIGURE 5.2: Time series of maximum tangential winds for the (a) default, (b) 2x, (c) 4x, and (d) 8x runs. Overlaid are theoretical predictions of maximum intensity using E-MPI (orange) from Eq. 3.2 (with a fixed 80% relative humidity) and using a boundary layer balance (green) from Eq. 3.6. The overlays are computed once daily using daily averaged model output.

ulations using a new thermodynamic formulation by Ooyama (2001). For a 28 C SST simulation at the highest resolution without ice physics, the intensity of the modeled hurricane reached 140 m s^{-1}. This sensitivity is confirmed here with the entirely different RE87 model (Fig. 5.2), and this modeled intensity greatly exceeds E-MPI. The tendency to greatly exceed E-MPI ($V_{max} - V_{E\text{-}MPI} \gg 0$) at high resolution will hereafter be referred to as "superintensity" and will be the focus for the remainder of this chapter. The 2x, 4x, and 8x runs appear to reach a steady state intensity by 10

TABLE 5.3: Summary statistics. V, R, P, and W represent samples of model output at 10-minute intervals. V is the sample of V_{max}. R is the sample radii where V_{max} occurs. P is the sample of minimum central surface pressures. W is the sample of maximum updraft speeds W_{max}. The other symbols are operators: MAX is the maximum of a sample; D is the daily running mean of a sample; MEDIAN is the median of a sample beyond day 10; MEAN is the mean of a sample beyond day 10; and MIN is the minimum of a sample.

run	default	2x	4x	8x
MAX(V) (m s^{-1})	71.77	87.74	100.20	101.90
MAX(D(V)) (m s^{-1})	67.81	83.75	95.96	96.79
MEDIAN(V) (m s^{-1})	62.04	80.21	90.42	87.51
MEAN(R) (km)	43.89	22.23	26.14	22.91
MIN(P) (mb)	935.0	906.5	894.2	901.8
MEDIAN(P) (mb)	952.9	917.7	910.1	922.9
MAX(W) (m s^{-1})	8.32	13.20	22.80	30.13
MAX(D(W)) (m s^{-1})	4.77	7.58	10.86	13.58

days, with generally stronger steady state intensities at higher resolution. The default case (Figure 5.2a) also appears to complete its initial spin up by day 10, but transitions to a second apparent steady state near 20 days.

Table 5.3 summarizes the output from each model run. From the first three rows we see evidence for convergence in the ultimate steady state intensity with increases in resolution by the 4x run. While MAX(V) and MAX(D(V)) continue to increase slightly for the 8x run, these can be attributed to short-lived events on the order of a day (Figure 5.2). MEDIAN(V) for the 8x run is actually smaller than for the 4x run. Hausman (2001) proposed that at higher resolution, a smaller radius of maximum winds (RMW) and thus a higher wind speed can be resolved. For both the default and 2x runs, MEAN(R) is about $3\Delta r$, but MEAN(R) appears to have converged to 22 km radius with the 2x run and the observed difference in steady-state intensity between the 2x and 4x runs cannot be explained by a change in RMW. Although the 4x run appears most intense in terms of central pressure, MEDIAN(P) seems also to have largely converged by the 2x run at about 915 mb. Both extreme updrafts, MAX(W), and the "smoothed" peak updrafts, MAX(D(W)), appear not to have converged with these simulations.

Overlaid on Figure 5.2 are estimates of E-MPI using daily averaged data. The green lines use the boundary layer balance (3.6), where χ_b is defined at the first vertical grid level and is evaluated

at the RMW. For the orange lines, (3.2) is used with a fixed $\mathcal{H}$ of 80%[2]. The outflow temperature should be computed following a parcel using (following RE87 with a reversed order of integration so that the direction of the integral is the same as the direction of the flow)

$$T_{out} = \frac{1}{\ln \frac{\theta_{e_a}}{\theta_e}} \int_{\ln \theta_e}^{\ln \theta_{e_a}} T d(\ln \theta_e). \tag{5.10}$$

In (5.10) the integration begins at the base of the updraft in the eyewall and terminates at an ambient value θ_{e_a} where the parcel comes in contact again with the boundary layer.[3] In practice this proved computationally expensive to compute and frequently the computed trajectories intersect the outer boundary making evaluation impossible. Thus the form of T_{out} used in Figure 5.2 is an outflow-weighted temperature evaluated at 150 km radius computed using daily-averaged fields

$$T_{out} = \left(\frac{1}{\int_{z=0}^{z_{top}} U^{(+)} dz} \right) \int_{z=0}^{z_{top}} U^{(+)} T dz \tag{5.11}$$

where

$$U^{(+)} = \begin{cases} 0 & \text{for } u < 0 \\ u & \text{for } u \geq 0 \end{cases} \tag{5.12}$$

Since the integral in (5.10) includes portions of the middle and lower troposphere which are not strongly weighted in (5.11), we should expect using simple lapse rate considerations (5.11) to give a somewhat cooler estimate of (5.10). For our cases it appears as a cool bias of 5-10 K. Supplying this bias into E-MPI provides for a 5 m s^{-1} strong bias in estimating V_{max}.

5.3 The Eye as a Latent Heat Reservoir

5.3.1 Phenomenology

The hypothesis of this paper is motivated by the behavior of the default run before and after 20 days, when the transition from one quasi-steady intensity to another occurs (Fig. 5.2a). Prior to this time there is a θ-anomaly in the boundary layer of the eye (RMW at the surface $\sim$ 40 km), but almost no temperature anomaly (Fig. 5.3). This is then followed by enhanced warming generally

---

[2]RE87 find $\mathcal{H}$ = 81.8% for their Experiment J. See Appendix C for more details.

[3]This represents the "cold" reservoir temperature of the Carnot cycle presented in Emanuel (1986) if ascent in the eyewall were to preserve its value of θ_e.

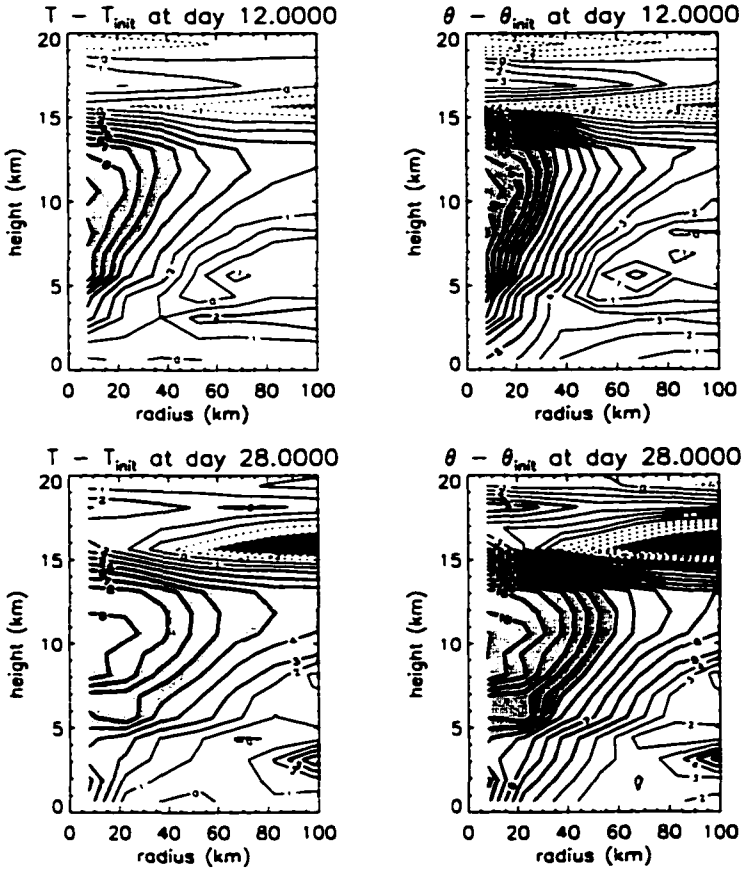

FIGURE 5.3: Temperature T and potential temperature θ (K) from the default run displayed as departures from the initial state for days 12 and 28. Dashed contours are negative. Blue shading denotes $T - T_{\text{init}} < -2$ K and $\theta - \theta_{\text{init}} < -4$ K. Yellow shading denotes $2 < T - T_{\text{init}} < 5$ K and $4 < \theta - \theta_{\text{init}} < 10$ K. Pink shading denotes $T - T_{\text{init}} > 5$ K and $\theta - \theta_{\text{init}} > 10$ K.

in the eye and specifically in the lower levels of the eye. The higher-resolution simulations show this fully-developed eye structure during the initial contraction of the vortex (before 10 days), and thus do not pass through multiple intensity states. Associated with this eye structure is an enhancement of Θ_e in low levels. In the case of the default run, the low-level eye Θ_e is enhanced over values in either the upper-level eye, eyewall, or ocean surface (Fig. 5.4, days 18 and 20). Since this enhancement of Θ_e, if introduced into the convectively-modified environment of the eyewall, can represent a source of local buoyancy, this feature can be referred to as a reservoir of potential buoyancy.

The establishment of the reservoir in our default run appears to occur in two steps. The first step involves the elimination of the initial middle level Θ_e minimum. By day 6 (Fig. 5.4), the

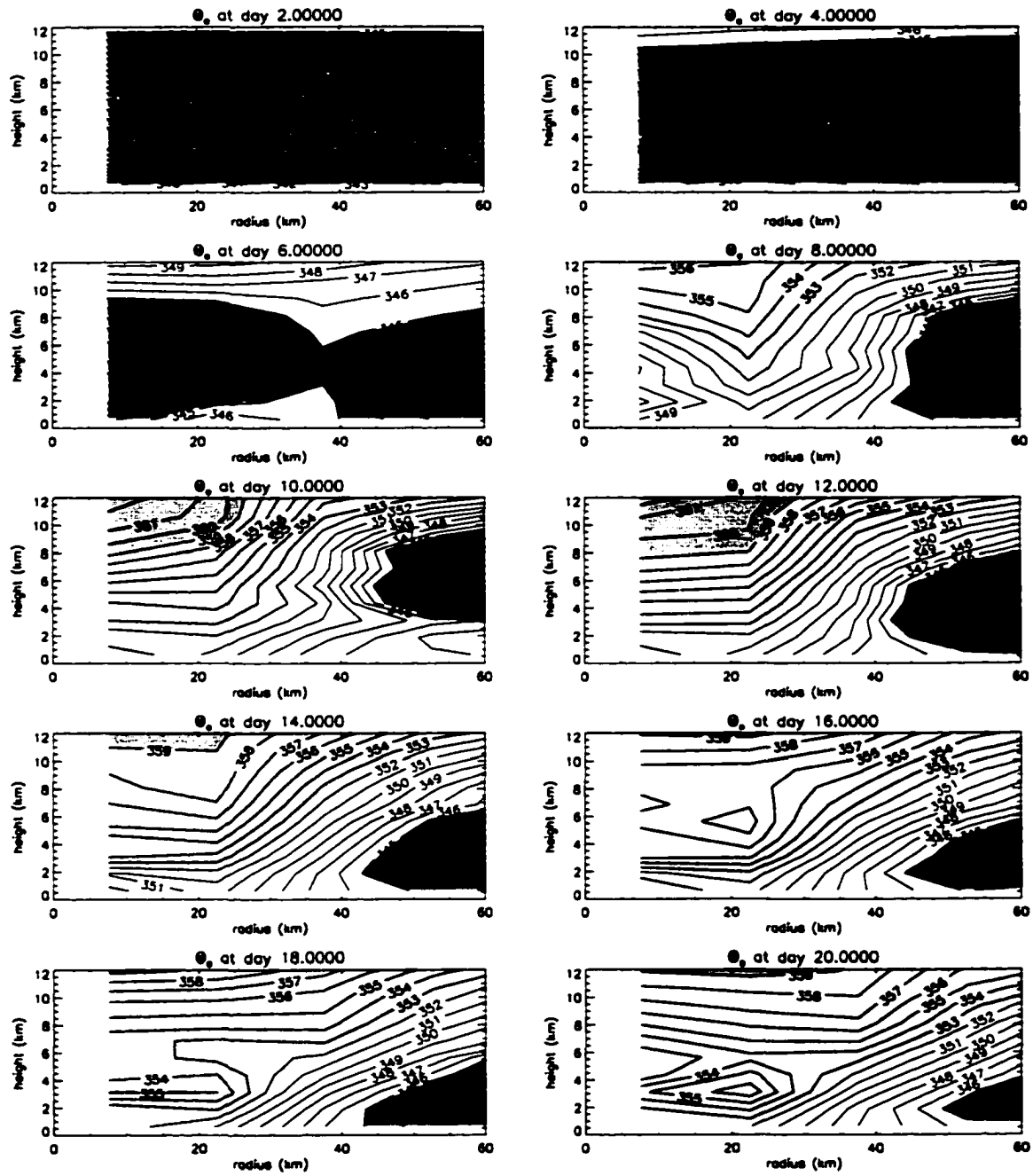

FIGURE 5.4: Equivalent potential temperature Θ_e (K) at a sequence of times in the default run. Purple shading denotes $\Theta_e < 338$ K. Blue shading denotes $338 < \Theta_e < 345$ K. White shading denotes $345 < \Theta_e < 352$ K. Yellow shading denotes $352 < \Theta_e < 359$ K. Pink shading denotes $\Theta_e > 359$ K.

minimum has been pinched in half with the development of persistent convection in the eyewall. This persistent convection equilibrates the eyewall close to a moist adiabat by day 8. After the convection is established, a secondary circulation is created in the eye that forces descent and

recirculation into the eyewall at low levels. This eye circulation advects the original Θ_e minimum to lower levels where it can come into contact with the top of the boundary layer, and thus into indirect contact with the ocean. The descent also advects down the high Θ_e that occurs with stabilization near the tropopause. This warms the eye.

At higher resolution, a multi-scale response of the eye can be resolved, with strong descent concentrated in a narrow column just interior to (i.e., at smaller radii than) the eyewall, with much weaker descent throughout the rest of the eye. Because of this, the original mid-level Θ_e minimum is never totally exhausted from the eye (Fig. 5.5). On the other hand, Θ_e is enhanced just interior to the eyewall, which results from a combination of dry descent and subgrid-scale inward mixing (which is locally non-conservative) of vapor from the saturated eyewall. The channel of warmest Θ_e at day 10 also is under weak saturated ascent, interior to the peak updraft. By day 10, the 360 K contour connected to the upper-troposphere descends down to 3 km. After this time this contour ascends and the lower-level reservoir appears to expand with the 360 K contour moving up to 5 km altitude. This occurs as a result of both an inward radial diffusion of vapor and vertical advection of heat and moisture from the eye boundary layer, which is enriched by interaction with the ocean. The default run (Δr = 15 km), which resolves the eye by one or two radial grid points, cannot represent this detailed multi-scale circulation.

The ultimate source of enhanced entropy for the low-level eye is an upward flux of moisture from the ocean surface at greatly reduced surface pressure (Fig. 5.6). The warming of the eye has lead to a reversal of the potential temperature gradient such that the eye is actually warming the ocean, but sub-saturation in the eye leads to a much greater flux of q_v into the atmosphere. The net effect is to positively force Θ_e. A negative flux removing moist entropy from the low-level eye is therefore necessary to maintain a steady-state. Smith (2002; submitted manuscript) presents an idealized boundary layer model for hurricane-like vortices and finds the boundary layer remains subsaturated. For his cases, the surface latent heat flux is maximized at the RMW, but also significantly positive beneath the eye like that found in Fig. 5.6.

5.3.2 Entropy budget

In Fig. 5.7, we present a Θ_e budget at pseudo-steady state of the eye/eyewall region (day 20), a higher dimensional extension of the analysis of section 4b of RE87. The budget is described there

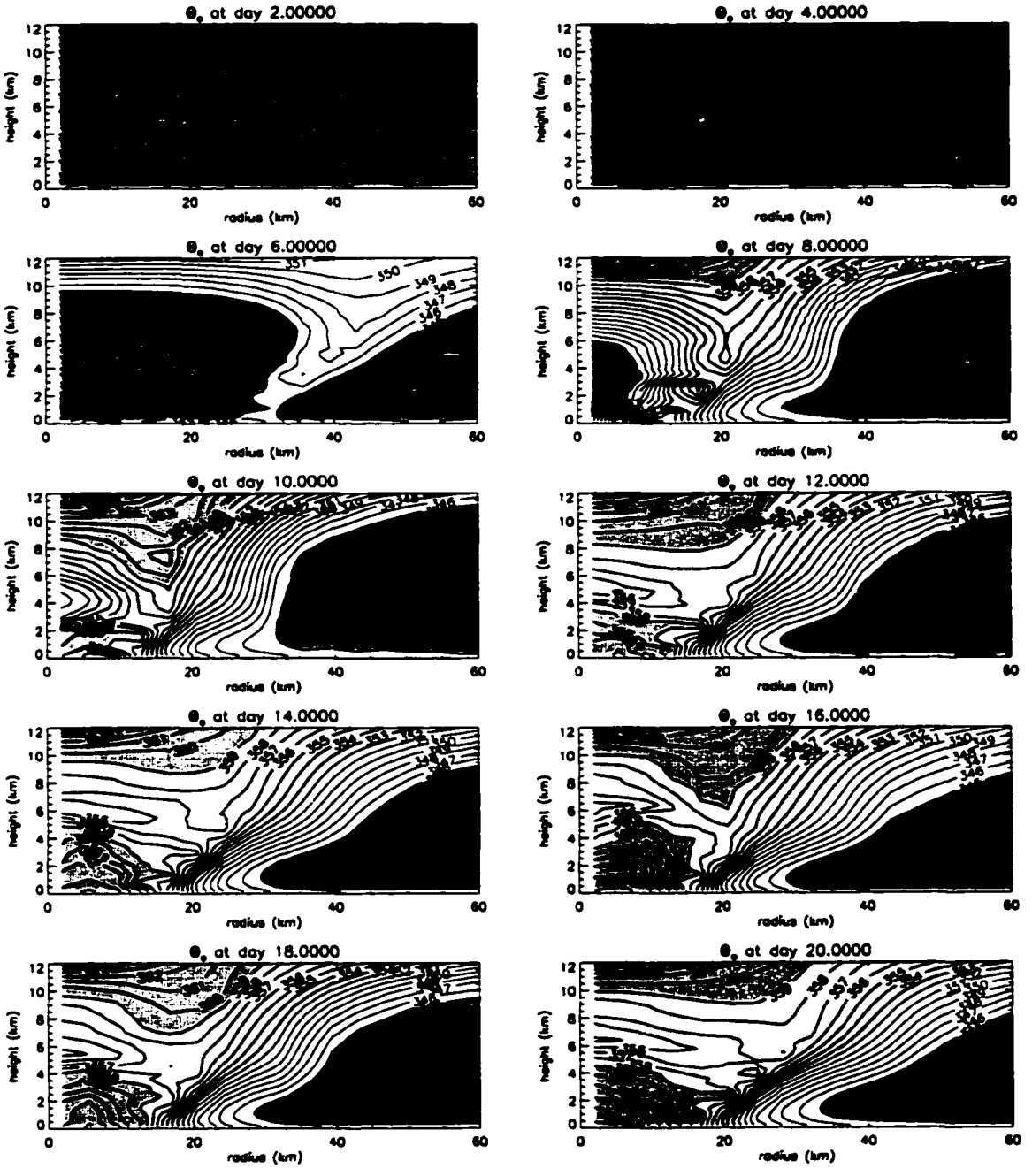

FIGURE 5.5: Time sequence of Θ_e (K) from the 4x run. Purple shading denotes $\Theta_e < 338$ K. Blue shading denotes $338 < \Theta_e < 345$ K. White shading denotes $345 < \Theta_e < 352$ K. Yellow shading denotes $352 < \Theta_e < 359$ K. Pink shading denotes $\Theta_e > 359$ K.

as approximate in terms of θ_e, but in terms of Θ_e it is more accurate. The pertinent Θ_e equation is

$$\frac{d\Theta_e}{dt} \simeq \frac{d\theta}{dt} + \frac{L\theta}{c_p T}\frac{dq_v}{dt} = D_\theta + \frac{L\theta}{c_p T} D_{q_v} + R \tag{5.13}$$

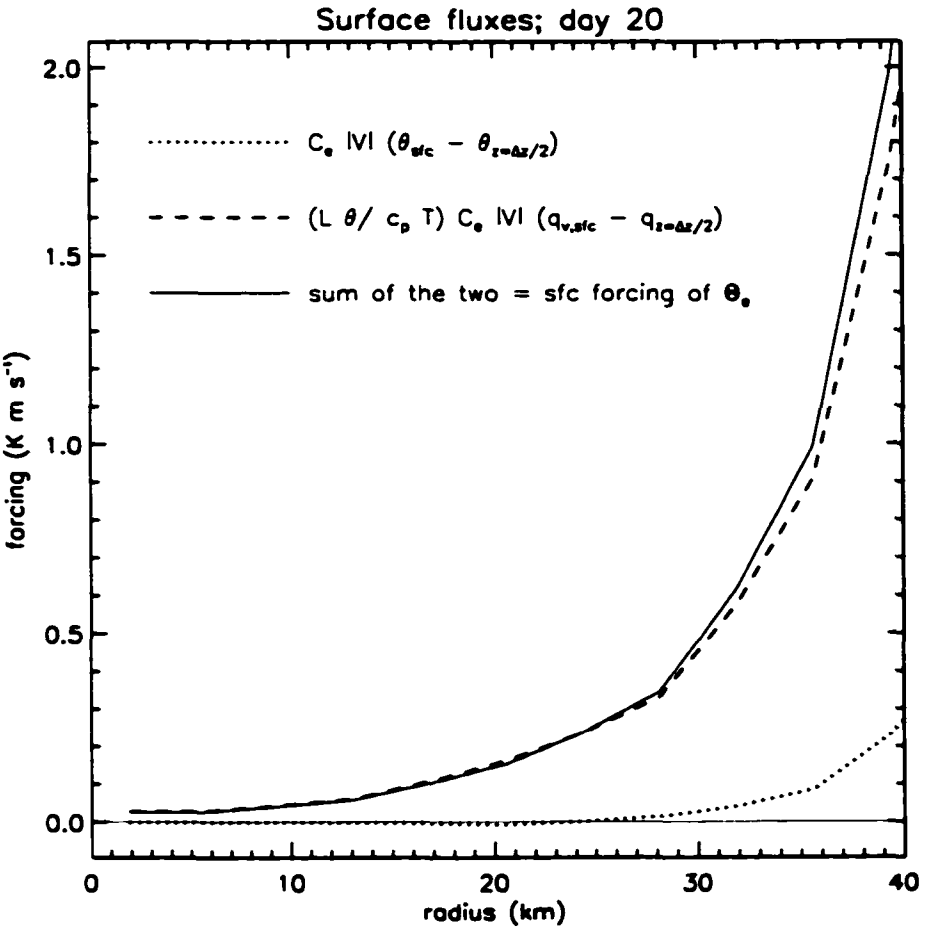

FIGURE 5.6: Surface forcing terms from the 4x run.

where D_θ and D_{q_v} are the diffusive forcing of θ and q_v, respectively, and R is the radiative forcing. Here we have assumed that

$$\frac{d}{dt}\left(\frac{\theta}{T}\right)\frac{L}{c_p}q_v << \frac{L\theta}{c_pT}\frac{dq_v}{dt}. \tag{5.14}$$

Using brackets to denote a day average and using the distributive property of the integral, the individual terms of the budget presented above are vertical advection (Fig. 5.7a)

$$-\left\langle w\frac{\partial \Theta_e}{\partial z}\right\rangle \doteq -\left\langle w\frac{\partial \theta}{\partial z}\right\rangle - \left\langle \frac{L\theta}{c_pT}w\frac{\partial q_v}{\partial z}\right\rangle, \tag{5.15}$$

radial advection (Fig. 5.7b)

$$-\left\langle u\frac{\partial \Theta_e}{\partial r}\right\rangle \doteq -\left\langle u\frac{\partial \theta}{\partial r}\right\rangle - \left\langle \frac{L\theta}{c_pT}u\frac{\partial q_v}{\partial r}\right\rangle, \tag{5.16}$$

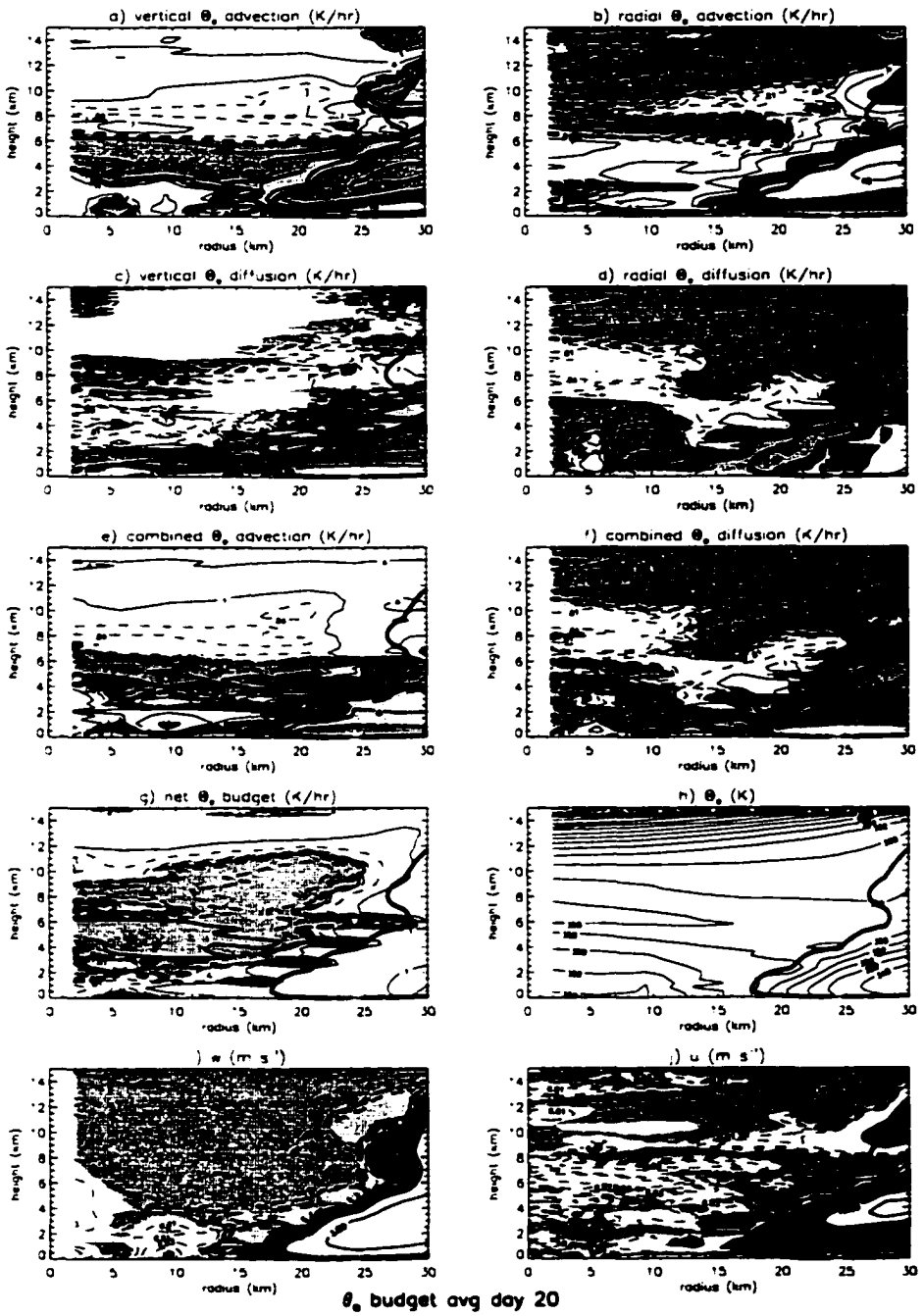

FIGURE 5.7: Budget of Θ_e averaged over day 20 of the 4x run in panels a-g. The heavy, solid black contour on each panel is the $w = 0.2$ m s^{-1} contour, and is provided as reference to roughly outline the eyewall updraft. Dashed contours are $\pm 0.001, 0.004, 0.01, 0.04$ K h^{-1}. The solid contours are $\pm 0.1, 0.4, 1, 4, 10, 40, 100, 400$ K h^{-1}. Panel h shows Θ_e with a contour interval of 2K; and panels i and j show w and u where the dashed contours are $\pm 0.01, 0.03, 0.1, 0.3$ m s^{-1} and the solid contours are $\pm 1, 3, 10, 30$ m s^{-1}. Green shading denotes forcings of Θ_e in panels a-g < -10 K hr^{-1}. Similarly for the other colors: $-10 <$ purple < -1; $-1 <$ light blue < 0; $0 <$ yellow < 1; $1 <$ orange < 10; and pink > 10 k hr^{-1}. For panel j, the shadings are the same except in terms of m s^{-1}. For panel i, the magnitudes of the shadings are the same as panel j, except reduced by an order of magnitude.

vertical diffusion (Fig. 5.7c)

$$-\left\langle \frac{\partial F_z^{\Theta_e}}{\partial z} \right\rangle \doteq -\left\langle \frac{\partial F_z^{\theta}}{\partial z} \right\rangle - \left\langle \frac{L\theta}{c_p T} \frac{\partial F_z^{q_v}}{\partial z} \right\rangle, \tag{5.17}$$

radial diffusion (Fig. 5.7d)

$$-\left\langle \frac{\partial F_r^{\Theta_e}}{\partial r} \right\rangle \doteq -\left\langle \frac{\partial F_r^{\theta}}{\partial r} \right\rangle - \left\langle \frac{L\theta}{c_p T} \frac{\partial F_r^{q_v}}{\partial r} \right\rangle, \tag{5.18}$$

and net tendency (Fig. 5.7g)

$$\left\langle \frac{\partial \Theta_e}{\partial t} \right\rangle \doteq \left\langle \frac{\partial \theta}{\partial t} \right\rangle + \left\langle \frac{L\theta}{c_p T} \frac{\partial q_v}{\partial t} \right\rangle. \tag{5.19}$$

The combined advection (Fig. 5.7e) is the sum of (5.15) and (5.16). The combined diffusion (Fig. 5.7f) is the sum of (5.17) and (5.18). The net budget (Fig. 5.7g) is the sum of the combined advection and diffusion terms and the radiative forcing. The storm is close to steady state and the *net* forcings are generally < 2 K d^{-1}, being much less than the exceptional magnitudes of each of the terms individually (≥ 800 K d^{-1}).

At pseudo steady-state, Θ_e of the inflow is a balance between negative forcing by radial advection (Fig. 5.7b) and positive forcing by vertical diffusion (Fig. 5.7c) and to a lesser extent upward advection (Fig. 5.7a). In the eyewall, positive outward advection (Fig. 5.7b) nearly balances negative upward advection (Fig. 5.7a), reflecting the largely slantwise ascent of the updraft. Under the assumption of moist neutral ascent, the sum of the radial and vertical advections (Fig. 5.7e) would vanish since isentropes are parallel to lines of constant angular momentum. For pseudo-steady state in the RE87 model, however, the radial advection of Θ_e exceeds in magnitude the vertical advection by 10 K hr^{-1} at the inner-edge of the eyewall (Fig. 5.7e), indicating an advective exchange between the eye and eyewall since generally $u > 0$ (Fig. 5.7j) in this region. This is compensated for in the lower portion of the eyewall by negative radial diffusion (Fig. 5.7b). The diffusion is redistributive and positive forcing of Θ_e occurs (Fig. 5.7b) due to radial diffusion in the lowest 3 km near the radius of peak updraft.

5.3.3 Trajectories

To confirm whether the eyewall updraft is being affected by warm air from the eye, forward/back Lagrangian trajectories bisecting the eyewall updraft are computed and displayed in

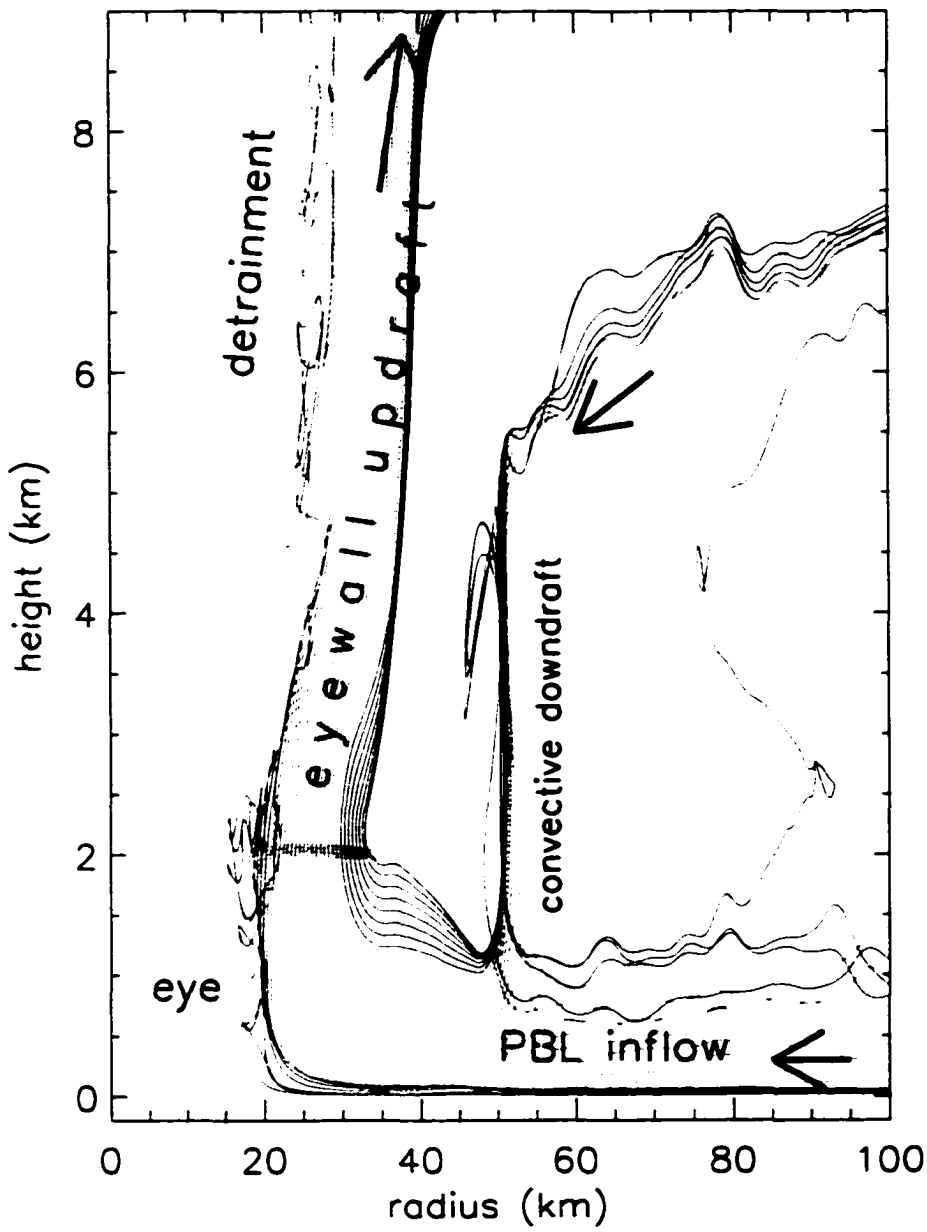

FIGURE 5.8: Half-day trajectories (when contained within the display domain) from the 4x run. These are forward/back trajectories "seeded" at 24.40 days at a height of 2 km bisecting the eyewall draft at equal spatial intervals. Trajectories are computed forward for 0.1 days and backward 0.4 days using the same seed points. Red trajectories enter the eyewall from the eye. Green trajectories enter the eyewall from the boundary layer inflow. Blue trajectories enter the eyewall from above the boundary layer. X's mark the seeding locations.

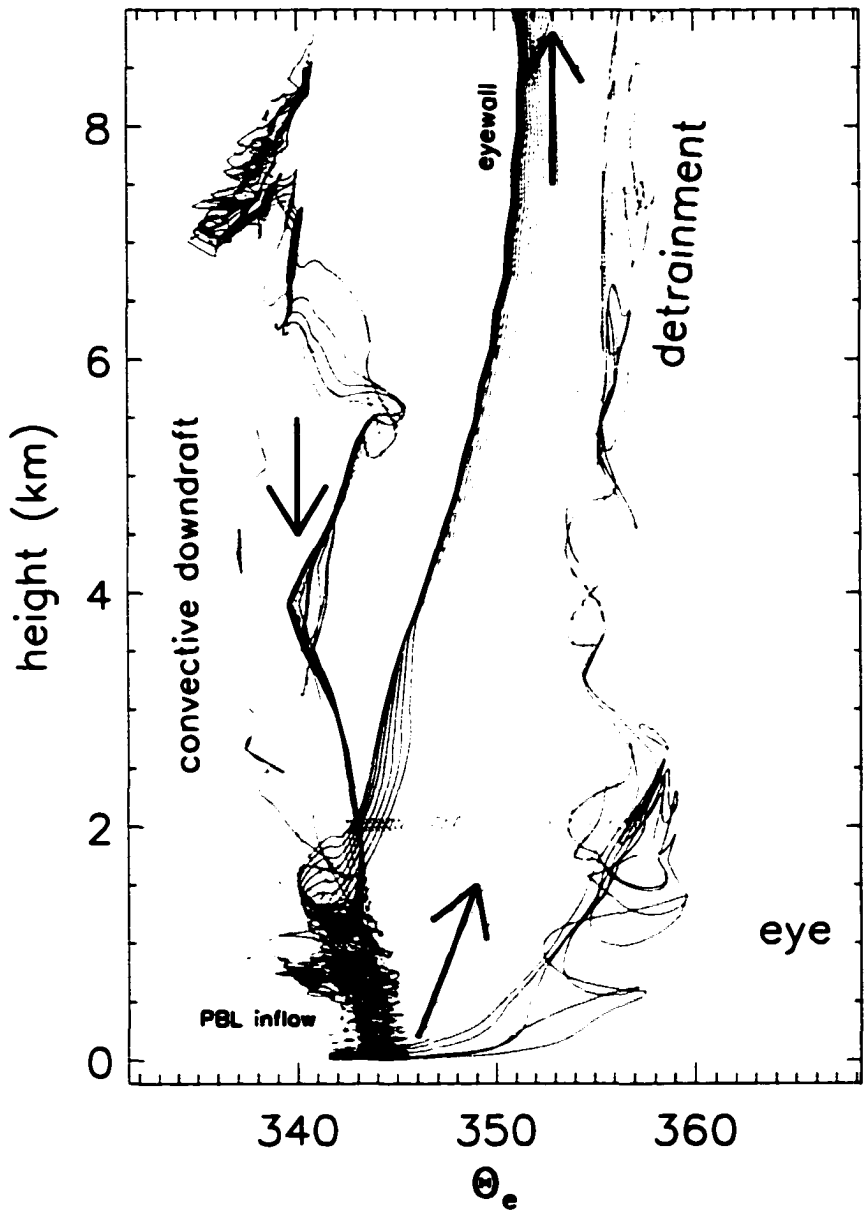

FIGURE 5.9: The same trajectories as Fig. 5.8, displayed as a function of Θ_e and height. Red trajectories enter the eyewall from the eye. Green trajectories enter the eyewall from the boundary layer inflow. Blue trajectories enter the eyewall from above the boundary layer. X's mark the seeding locations.

Figures 5.8 - 5.10. These are "seeded" at 24.4 d of the 4x run across the updraft at the 2 km height at equal radial spacing and are calculated forward for 0.1 d and backward for 0.4 d. Figure 5.8 shows that there are three sources for air upon introduction to the eyewall: 1) the boundary

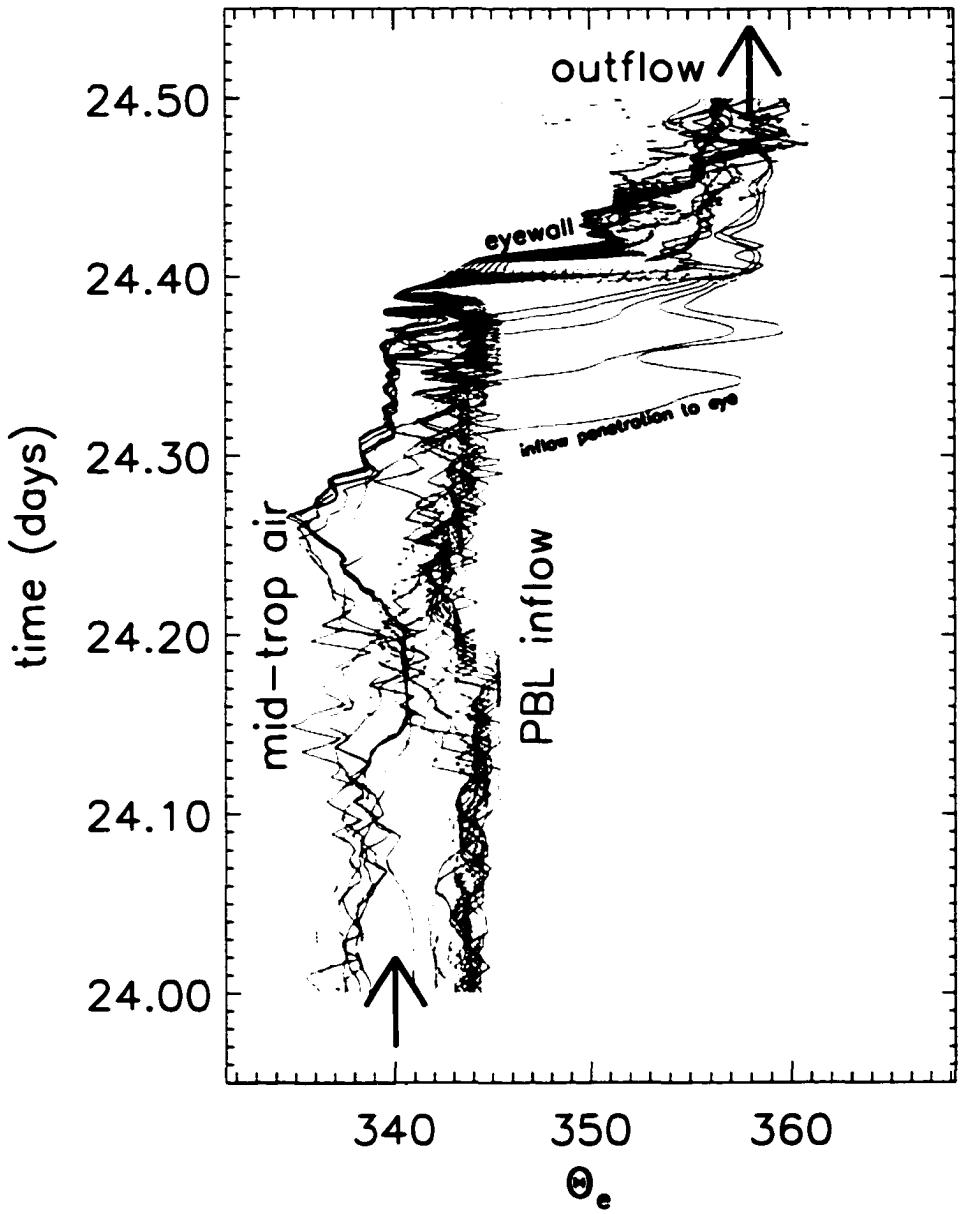

FIGURE 5.10: The same trajectories as Fig. 5.8, displayed as a function of Θ_e and time. Solid trajectories enter the eyewall from the eye. Dotted trajectories enter the eyewall from the boundary layer inflow. Dashed trajectories enter the eyewall from above the boundary layer. X's mark the seeding locations.

layer inflow (green), 2) low-level inflow above the boundary layer (blue), and 3) the eye (red). Selection of a higher seeding altitude can also expose a mid-level ($z \approx 5$ km) inflow (not shown). Of the inflow parcels shown here (Fig. 5.8; green and blue), some originate from a downdraft of a

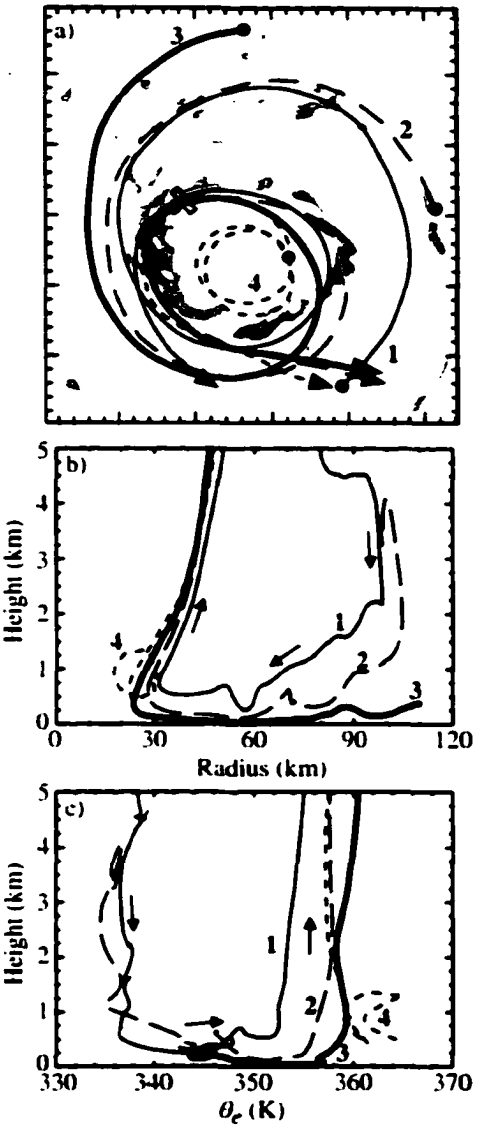

FIGURE 5.11: Figure 13 of Braun (2002), displaying trajectories from a three-dimensional simulation of Hurricane Bob using the MM5 model. The trajectories are "seeded" at a point of locally-enhanced ascent within the eyewall. (a) Horizontal projection of the trajectory paths in a reference from moving with the storm. Shading indicates simulated reflectivities greater than 40 dBZ at 66 h from initialization. Filled circles and arrow heads indicate the beginnings and ends, respectively, of the trajectories. The small rectangular box indicates where the trajectories were seeded. (b) Profiles of trajectory radius versus height. (c) Profiles of trajectory θ_e versus height. In (b) and (c), small arrows indicate the general direction of movement of the air parcels.

convective feature near $r = 45$ km and others from the boundary layer inflow from further radii. A similar feature was found by Braun (2002) using trajectories in a three-dimensional simulation of Hurricane Bob (1991) (reproduced here as Fig. 5.11).

Figure 5.9 shows that the entropy of the downdraft trajectories is indistinguishable from the other inflow trajectories (green and blue) by the time they encounter the eyewall updraft. The general nature of these trajectories (Fig. 5.9) are quite similar to trajectories shown by Braun (2002) in Fig. 5.11c. The Θ_e of the inflow trajectories is mostly a function of their originating height, and as they enter the eyewall, lower trajectories warm even more while penetrating to smaller radii (similar to Braun 2002). This is entirely consistent with a dominant ocean interaction. A handful of boundary layer inflow trajectories obtain much greater Θ_e values (355 K or more; lower-right part of Fig. 5.9, red) as they enter the base of the eye; typically the radial inflow weakly extends to the center of the storm due to the Ekman pumping in the weak positive vorticity regime of the eye. These penetrating inflow trajectories linger up to 2 hours in the eye (Fig 5.10) before being ejected into the eyewall. The left-to-right traces of trajectories in Figure 5.9 (red) indicate mixing of entropy with neighboring air. Boundary layer inflow trajectories increase in entropy as they ascend in the eyewall updraft to $z = 2.5$ km. Since much of this increase occurs above the boundary layer, an exchange of entropy must result from an additional source of warm Θ_e other than the ocean, namely the eye. Above $z = 2.5$ km, trajectories ascending in the outer portion of the eyewall continue to increase in Θ_e while those in the inner portion first decrease in Θ_e below $z = 4.5$ km (indicative of an exchange of entropy within the eyewall) and increase again above this level. Braun (2002) reached a similar conclusion with three-dimensional trajectories, suggesting that the result presented here is not peculiar to axisymmetric geometry. Parcels located near the inner edge of the eyewall detrain into the eye, where they increase in Θ_e, and frequently are reintroduced into the eyewall at a later time.

The evidence from sections 5.3.2 and 5.3.3 suggests that two related assumptions of E-MPI are violated in this model: the entropy exchange from the eye to the eyewall is non-trivial and the eyewall updraft is not moist-neutral.

5.3.4 Experimental suppression of the reservoir

To confirm that the low-level entropy source in the eye is crucial for maintaining the hurricane at superintensity, we might propose to eliminate the source through some artificial means. An experiment was performed where enhanced cooling by Newtonian relaxation (our surrogate for radiation) was applied in the lower eye after the 15th day of the 4x run. This leads to a rapid

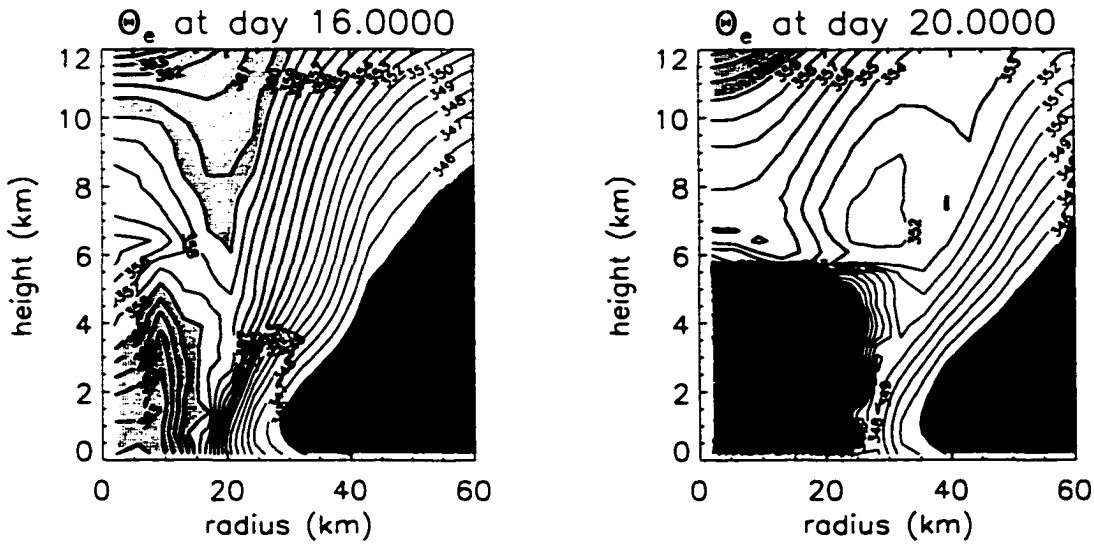

FIGURE 5.12: Θ_e (K) from the 4x run with an imposed artificial heat sink in the lower eye. Purple shading denotes $\Theta_e < 338$ K. Blue shading denotes $338 < \Theta_e < 345$ K. White shading denotes $345 < \Theta_e < 352$ K. Yellow shading denotes $352 < \Theta_e < 359$ K. Pink shading denotes $\Theta_e > 359$ K.

reduction of storm intensity from 90 to 75 m s^{-1} (not shown), but the intensity stabilized above E-MPI (55 m s^{-1}). This occurred because the RMW expanded from 20 to 30 km, thus placing 10 km of radial separation between the eyewall and our imposed forcing (Fig. 5.12). This experimental run produced a radial displacement of the latent heat reservoir centered on $r = 25$ km (compared to the control experiment where the reservoir is nominally centered at the origin). While E-MPI does not explicitly depend on the RMW, the expansion of the RMW could in part explain the weakening. On the other hand, the displaced entropy reservoir also experiences an enhanced heat sink due to its proximity to the imposed forcing, which also might in part explain the weaker storm.

5.4 Heat or buoyancy?

What remains is to establish the means by which the introduction of air with high entropy from the eye to the eyewall produces a stronger storm. The candidate phenomena come in two classes: those that necessarily invoke the non-hydrostatic properties of the RE87 model and those phenomena that can be well described with hydrostatic principles.

It is known that non-hydrostatic processes in tornadoes can drive wind speeds to more than twice the limit suggested by thermodynamic forcing of buoyancy in the environment of the tornado

(Bluestein et al. 1993; Fiedler and Rotunno 1986). Fielder (1994) shows that this can come about through either one of two phenomena: 1) an end-wall vortex, or 2) a drowned vortex jump. An end-wall vortex has its updraft directly at the axis of rotation which does not resemble our simulated hurricane, but the drowned vortex jump has its peak updraft at a non-zero radius and bears superficial similarities to a hurricane vortex. The drowned vortex jump is out of cyclostrophic balance and results from "nearly loss-free 'overshoot' of the radial inflow into nearly the lowest pressure of the core [of the tornado-like vortex]" (Fielder, 1994). Figure 5.1b suggests that the pressure perturbation force is downward directed and in part argues against a dynamic pressure force. The drowned vortex jump of Fielder (1994) shows a local pressure minimum near the radius of maximum low-level winds at the point where the inflow is stopped and directed upward that is different from Fig. 5.1b.

Eliassen's (1951) balanced vortex model, which assumes that the vortex evolves near a state of gradient and hydrostatic balance, can be used to further test the importance of non-hydrostatic effects in storm maintenance. The equation for the transverse streamfunction ψ under the Boussinesq approximation is given by

$$\frac{\partial}{\partial r}\left[\frac{N^2}{r}\frac{\partial \psi}{\partial r} - \frac{\xi}{r}\frac{\partial \bar{v}}{\partial z^*}\frac{\partial \psi}{\partial z^*}\right] + \frac{\partial}{\partial z^*}\left[\frac{\bar{\eta}\bar{\xi}}{r}\frac{\partial \psi}{\partial z^*} - \frac{\bar{\xi}}{r}\frac{\partial \bar{v}}{\partial z^*}\frac{\partial \psi}{\partial r}\right] = \frac{\partial \bar{Q}}{\partial r} - \frac{\partial}{\partial z^*}(\bar{\xi}\bar{F}) \tag{5.20}$$

where N is the Brunt-Väisälä frequency, F is the "external" (including eddy) forcing term for v, $(\theta_0 Q/g)$ is the "external" forcing term for potential temperature θ, and bars denote azimuthal means. Here

$$z^* = \left[1 - \left(\frac{p}{p_0}\right)^{\frac{\gamma-1}{\gamma}}\right]\frac{\gamma}{\gamma-1}\frac{p_0}{\rho_0 g} \tag{5.21}$$

is the pseudo-height (Hoskins and Bretherton 1972), where p_0 is a reference pressure, ρ_0 is a reference density for computing the scale height, and $\gamma = c_p/c_v$ is the ratio of the specific heats of dry air. In (5.20)

$$\eta = f + \frac{v}{r} + \frac{\partial v}{\partial r} \tag{5.22}$$

is the absolute vertical vorticity and

$$\xi = f + \frac{2v}{r} \tag{5.23}$$

is the modified Coriolis parameter. From (5.20), the secondary circulation of an axisymmetric mean vortex evolving near a state of gradient wind and hydrostatic balance can be solved for given known

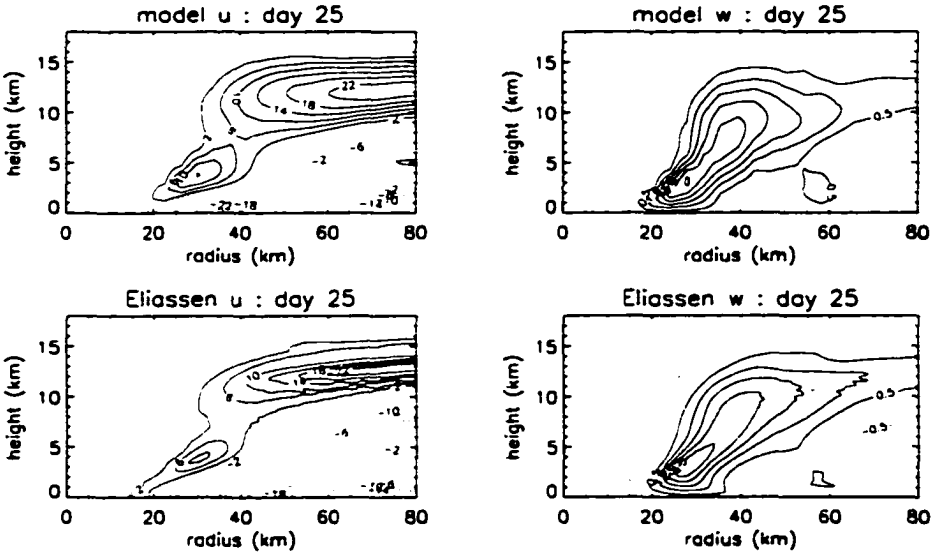

FIGURE 5.13: The secondary circulation (panels a and b) observed from the 4x run at day 25, and the same inferred from the Eliassen (1951) balanced vortex model using the observed axisymmetric structure and forcings at the same time.

momentum forcing F and heat forcing Q (Möller and Shapiro 2002 explain the methodology for regularizing the axisymmetric state in order to produce a solution; Chapter 2 also uses this technique). Since the forcings of momentum and heat can be derived from numerical output, our hypothesis is that if the resulting secondary circulation from (5.20) agrees closely with the secondary circulation output from the model, then the phenomenon described by the model is evolving primarily in gradient wind and hydrostatic balance. Figure 5.13 provides such a comparison, with the inflow and updraft of the storm well-represented in structure and intensity by the Eliassen balanced vortex model. Thus, it is believed that the model storm is evolves largely in a hydrostatic manner and non-hydrostatic effects do not need to be invoked to explain superintensity (Ockham's razor).

If we appeal to the conceptualization of E-MPI as a Carnot heat engine (Emanuel 1988), then the hurricane is a mechanism for producing work by processing heat. The measure of work performed ultimately is the dissipation of the system, and the rate of dissipation increases with the intensity of the storm. A stronger storm would thus require more heat addition to produce more work. This explanation of superintensity simply comes down to added heat in the eyewall, which in part motivates the section title. Heat addition is of course not inconsistent with the generation of local buoyancy (Braun 2002) and the stretching of vortex tubes, but the distinction here is that

if the storm intensity is a function of the addition of heat (in the spirit of E-MPI theory) the role of local buoyancy is secondary or simply consistent.

E-MPI assumes that all the addition of heat to the eyewall is through its base via exchange with the ocean. The evidence presented here suggests that there is additional heat provided from an interaction with the eye. E95b (Sec. 4, pp. 3973–3974) noted that this assumption represents a potential weakness of maximum intensity theory. The Carnot derivation of E-MPI (Emanuel 1988) takes the boundary layer inflow as the isothermal expansion step (see a standard physics text, e.g., Halliday and Resnick 1988) where heat is added; the eyewall updraft as the (moist) adiabatic expansion step; and the outflow and descent as a combined isothermal compression and adiabatic compression step.[4] The boundary layer inflow could be referred to as the *warming phase* of the cycle, and the outflow and descent as the *cooling phase*, although the definition of T_{out} provided by (5.10) includes implicitly the eyewall as part of the cooling phase. Under the ideal assumptions of E-MPI theory, though, inclusion of the eyewall would not impact T_{out}. We might propose to extend the warm phase to include the eyewall where heat addition is observed to occur. In this spirit one can consider warming of updraft parcels relative to a moist adiabat. At the top of the eyewall updraft, q_v is much less than that found near the surface, thus most of the augmentation of Θ_e must occur in changes in θ. Assuming that the surface is approximately 1000 mb, the changes in θ can be related directly to changes in SST, thus motivating the following *ad hoc* modification of E-MPI

$$\mathrm{SST}' = \mathrm{SST} + \Delta\Theta_e = \mathrm{SST} + (\Theta_{e,\mathrm{out}} - \Theta_{e,\mathrm{sfc}})\,. \tag{5.24}$$

Analysis generally shows $\Delta\Theta_e \approx 8$ K, which represents a significant augmentation of SST' from 26 to 34 C. E-MPI with this modification provides intensities of ≈ 83 m s^{-1}. Compared to the approximations of E-MPI summarized in Appendix C that do not provide such a close estimate of the observed model intensity (≈ 90 m s^{-1}), we believe that the violation of the related assumptions of vanishing heat exchange from the eye to the eyewall and moist neutral ascent are principally

[4]While it can be argued whether real storms actually complete the cycle, examination of recirculating trajectories here suggest that the cycle can occur in $\approx$ 14 days.

responsible for the observed superintensity.[5] As E-MPI is an estimate of the magnitude of the gradient wind, one can appeal to theoretically-based frictionally-induced enhancements of tangential wind speed of $\approx 7\%$ found in Shapiro (1983). Alternately one may note the 7 m s^{-1} underestimation of (3.6) by the complete E-MPI calculation (Fig. 5.2; green curve larger than the orange curve), which can be considered a measure of the error incurred in piecing the eyewall solution together with the environment. It should be noted that this modification of E-MPI is *ad hoc* and simply diagnostic since we do not know *a priori* the magnitude of the warming ($\Delta\Theta_e$) of the eyewall. An improved formulation of MPI from first principles to include this effect, whether as a modification of E-MPI or not, would seem to be of great scientific value.

5.5 Three-dimensional evidence for superintensity

Our explanation of superintensity in the RE87 model is that the eyewall is able to utilize a second source of heat available from the eye. Although reality rarely reaches or exceeds E-MPI (Emanuel 2000), this mechanism may play a role in boosting the intensity of observed hurricanes. Figure 5.14 shows results from an MM5 simulation of Hurricane Bob employing an unprecedented horizontal grid spacing of 1.3 km on the finest grid (Braun 2002). The RMW (dotted circle) at this time was at $r = 37$ km and the radius of peak updraft (not shown) is at $r = 41$ km. Equivalent potential temperature (exponential form) θ_e at the $z = 1135$ m level is enhanced in the eye relative to the eyewall. Positive anomalies in θ_e at the edge of the θ_e enhancement (the interface between the eye and the eyewall) are on the southeast (outward advecting) side of positive moist PV (MPV; Schubert et al. 2001)[6] anomalies. Fulton (2001) provides anecdotal evidence that when these θ_e anomalies encounter the eyewall, they are associated with localized enhancements in updraft speed.

---

[5] If we were to extend the analogy of the Carnot engine, the addition of heat could be thought of as a Carnot turbocharger, since warm eye air represents an untapped energy source just as the blow-down pressure of air exiting a normally-aspirated engine represents an untapped "free" energy source that can be used to power an air pump (i.e., a turbocharger; see a standard text such as Heisler 1995 for more details on automotive engines). The proposed impact of dissipational heating (Bister and Emanuel 1998, Businger and Businger 2001) can analogously be interpreted as a Carnot supercharger, since the energy for a supercharger is extracted directly from the useful work of the engine while dissipational heating is extracted directly from the kinetic energy field of the storm.

[6] See Fulton (2001) for a comparison of dry PV, MPV, and PV using θ_e as the thermodynamic variable. Dry PV is largely similar to MPV which includes the thermodynamic properties of dry and wet gas plus the liquid and ice mass.

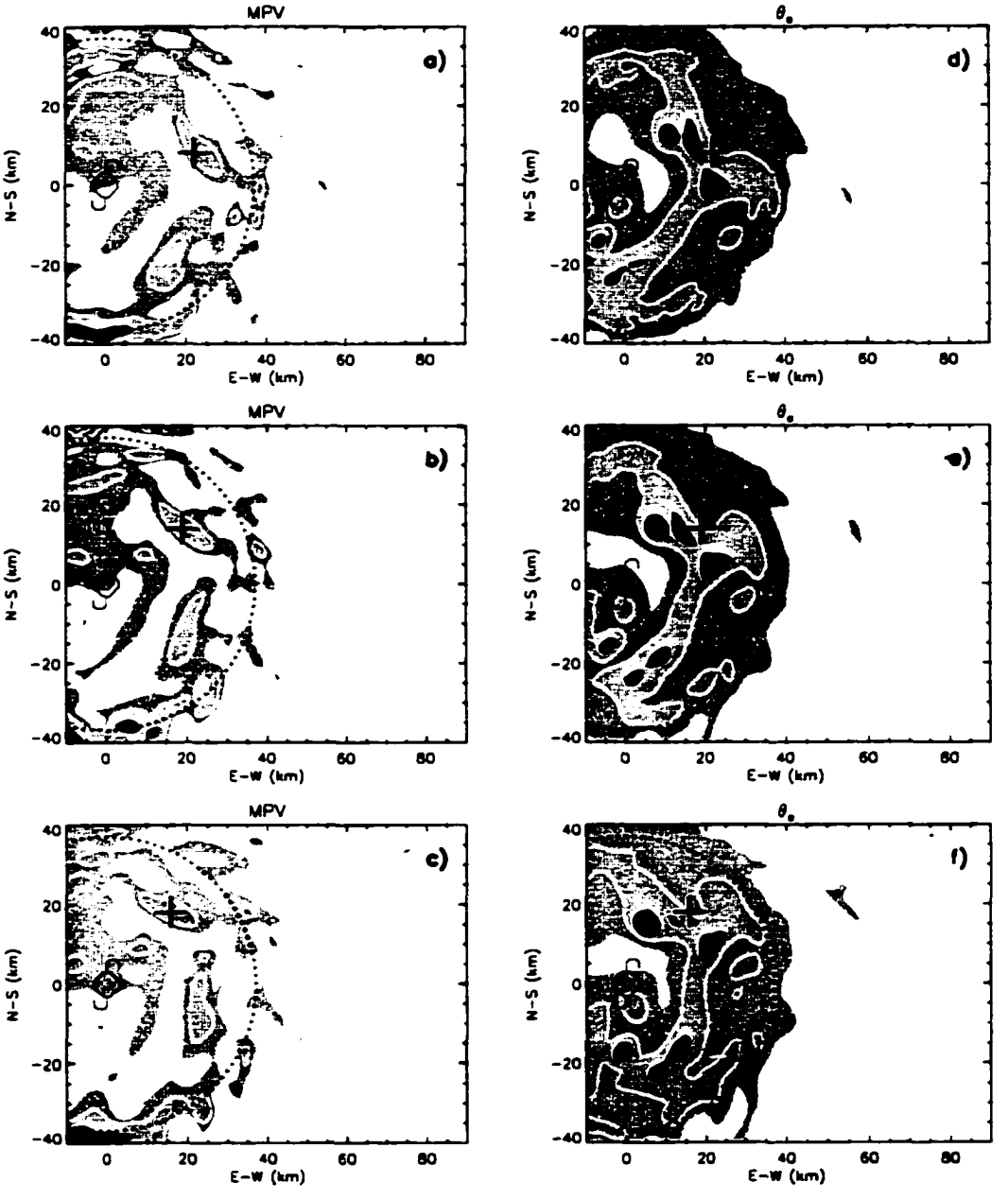

FIGURE 5.14: Moist potential vorticity (MPV) at $z = 1135$ m at (a) 268, (b) 272, and (c) 276 minutes into an MM5 simulation of Hurricane Bob, kindly provided by S. A. Braun, NASA/GSFC (see Braun 2002 for details). Data is reported at the 1.3 km grid spacing of the inner-most mesh. Equivalent potential temperature θ_e is displayed in panels (d-f) at respective times. The hurricane symbol denotes the storm center. Levels of shading in panels (a-c) denote: no shading, MPV < 0 PVUs; grey shading, $0 <$ MPV < 15 PVUs; blue shading, $15 <$ MPV < 30 PVUs; pink shading, $30 <$ MPV < 60 PVUs; red shading, MPV > 60 PVUs. Levels of shading in panels (d-f) denote: no shading, $\theta_e < 345$ K; grey shading, $345 < \theta_e < 351$ K; blue shading, $351 < \theta_e < 357$ K; pink shading, $357 < \theta_e < 363$ K; red shading, $\theta_e > 363$ K. The dotted circle is the radius of maximum winds, $r = 37$ km. The "+" is to mark the position of a typical enhancement of MPV interior to the RMW. Cyclonic motion around this MPV enhancement appears to advect high θ_e air radially outward to the RMW around the southeast side of the feature. Figure adapted from Fulton (2001).

Braun (2002) shows quantitatively that these "hot towers" carry the majority of the updraft mass flux of the eyewall. Braun (2002) has further shown that these "hot towers" are associated in this simulation of Hurricane Bob with the end points of a wavenumber 2 asymmetry that has an angular velocity that is well described by that of a barotropic vortex Rossby wave. There is an obvious suggestion then for a possible local generation of buoyancy, but Braun (2002) also shows that in contrast to Zhang et al. (2000) a dynamic pressure force does not drive hot tower ascent.

Frank and Ritchie (2001; their Fig. 16) show another MM5 simulation with peak wind speeds greater than 100 m s^{-1} for a simulated hurricane over 28.5 C SST for a case of low vertical shear. E-MPI, with an $\mathcal{H} = 80\%$ and reasonable selection of outflow temperature (-65 to -70 C), would be between 75 and 78 m s^{-1} (see Fig. 3.1), so E-MPI is exceeded for this three-dimensional simulation. Frank and Ritchie (2001; their Fig. 7b) also show a low-level enhancement of θ_e in the eye, but did not notice this as a superintense situation because they used minimum central pressure as the E-MPI metric rather than maximum tangential winds. As far as the derivation of E-MPI (E95b) is concerned, V_{max} is obtained first for a given thermodynamic environment. Central pressure is obtained with further assumption and approximations. We believe V_{max} is the more robust metric of E-MPI.

Three regimes for the radial profiles of θ_e across the eye derived from aircraft reconnaissance of hurricanes were described by Kossin and Eastin (2001) from flight-level data. In the first, associated with intensification, θ_e was a maximum in the eyewall. The second, associated with weakening, has a θ_e maximum at the center of the storm. These states were argued to be associated with cycles of barotropic instability generated by vorticity stretching by enhanced convection in the eyewall during intensification stages. Mentioned also by Kossin and Eastin (2001, Section 2d., pp. 1088-1089) was a third regime where intensification occurred with a θ_e maximum at the center of the storm, more closely resembling our RE87 model simulations and the MM5 Bob simulation. This regime occurred less frequently in the flight-level observations available than the first regime and occurred at nearly the same time as the first regime, but just in different azimuths of the storm (M. Eastin 2002, personal communication).

Willoughby (1998) provides independent observational evidence that the low-level eye at times (Fig. 5.15) may have the same entropy as the eyewall, and at times the eye can be greater (by more the 10 K). It is also interesting to note the θ_e of the eyewall (denoted by two large dots in Fig.

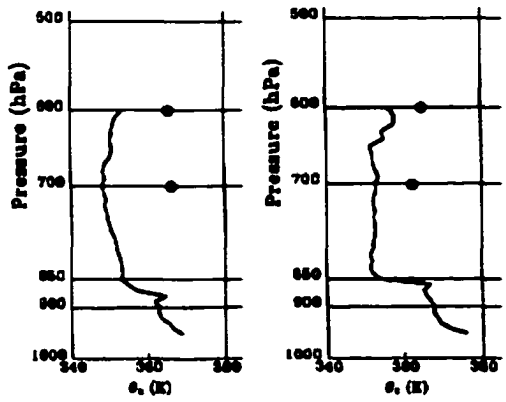

FIGURE 5.15: Dropsonde retrieval of θ_e from the eyes of (a) Hurricane Olivia (East Pacific, 2123 UTC 24 September 1994), and (b) Hurricane Jimena (East Pacific, 2058 UTC 23 September 1991) compared to θ_e measured on-board aircraft at the moment of eye penetration (large dots), defined by the last measurement of saturation. Figure adapted with kind permission from Willoughby (1998).

5.15b) increases in height when the low-level eye is warmer. From Willoughby (1998) we can also infer that aircraft flight-level data is not always indicative of the low-level eye entropy structure, depending on the altitude of the inversion level (Kossin and Eastin 2001). The boundary layer below the eye in the RE87 model is given 20 days to respond (Fig. 5.16) to the intensity and surface fluxes of the hurricane, while real hurricanes are hardly allowed to attain a steady-state for a period of many days. Thus the model eye sounding does not show a sharp inversion and Θ_e is minimized at mid-levels (400 mb) rather than remaining constant with height. LeeJoice (2000) with composite dropsondes shows that eye soundings at $z < 3000$ m average 5 to 10 K warmer than in the eyewall, which is confirmed for the RE87 model in Fig. 5.16.

5.6 Discussion

We have demonstrated that the RE87 model will produce a model storm of increasing intensity with increasing resolution. Convergence in the maximum tangential winds was found with sufficiently high resolution. Hausman (2001) suggested that the increase in storm intensity is due to decreases in the RMW at higher resolution; smaller RMW's simply were not resolvable at coarse resolution. Our finding with the RE87 model is that the RMW stabilizes by the 2x run, but increases in intensity further occur to the 4x run (Table 5.3).

Figure 5.17 summaries many of the important interactions associated with superintensity, where the abscissa is displayed as a function of absolute angular momentum ($M = rv + fr^2/2$).

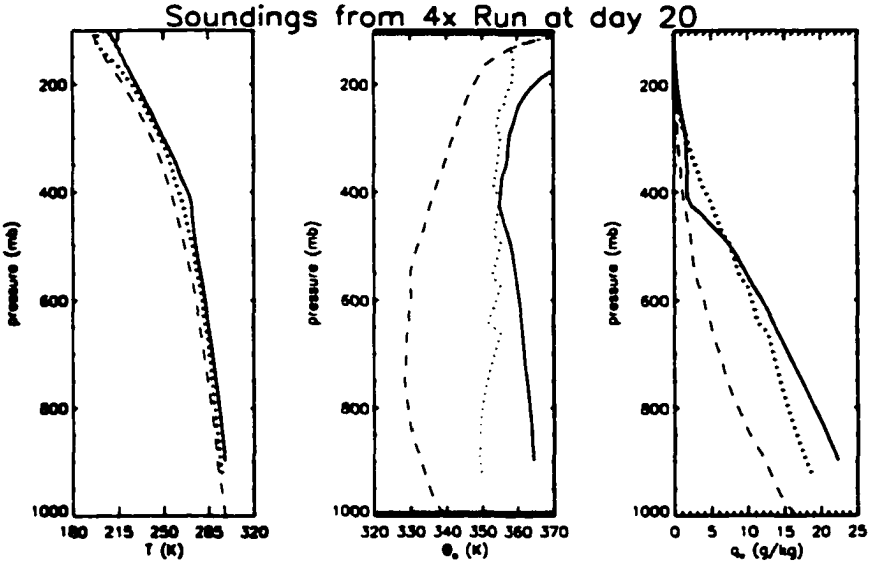

FIGURE 5.16: Soundings for the eye (solid; computed at $r = 0$ km), the eyewall (dotted; computed at the radius of peak updraft), and the environment (dashed; averaged over $r > 800$ km). The eyewall sounding shows jagged-ness because of the discrete outward jumps in radial grid steps of the peak updraft.

We have demonstrated a low-level entropy maximum in the eye (Fig. 5.17, red contours) that is associated with superintensity relative to E-MPI and an interaction between the warm eye and the eyewall (Fig. 5.17, streamlines near $M = 1 \times 10^6$ m^2 s^{-1}). After showing that the storm evolves largely in gradient and hydrostatic balance, the related assumptions of E-MPI theory that the eyewall is in slantwise, moist adiabatic ascent without interaction with the eye are violated (Fig. 5.17, noting through the vertical alignment of streamlines in the shaded, saturated eyewall region of the storm that angular momentum is better conserved than entropy). Through a simple addition of heat much of the superintensity of the modeled storm can be largely explained with an *ad hoc* modification of E-MPI.

We can interpret from the eddy features in the streamlines of Fig. 5.17 as the break down of an azimuthal vortex sheet and as the primary advecting mechanism between the eye and the eyewall. Associated with these eddy features is a tangential vorticity of $\approx -1 \times 10^{-2}$ s^{-1} (not shown). The internal redistribution of heat within the eyewall by diffusion raises the question whether the basic result presented here is a peculiarity of the diffusion scheme of the model. An experiment using greatly reduced diffusion (by a factor of 16) shows that role of diffusion is replaced by temporal eddies and the time series of V_{max} (not shown) has a short period variability of ≈ 4 m s^{-1} but

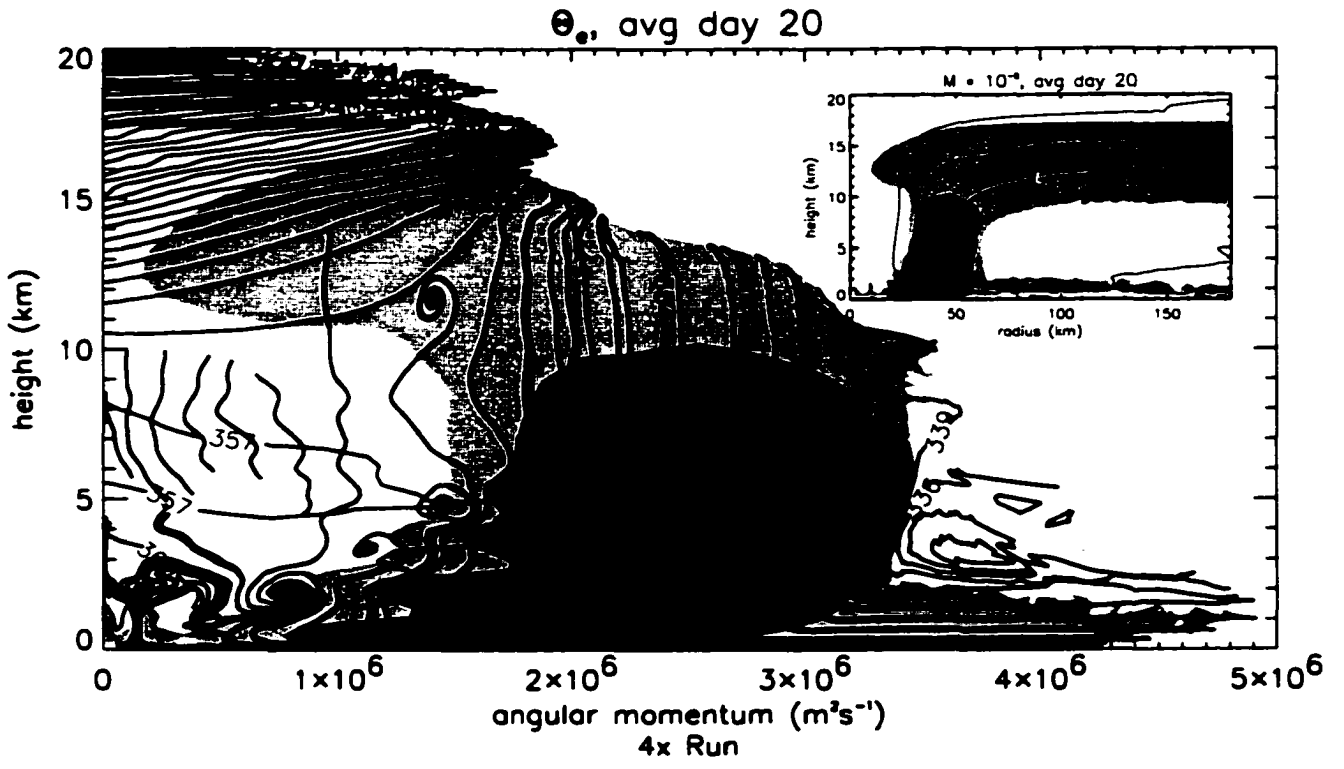

FIGURE 5.17: Equivalent potential temperature Θ_e (K; red; one day average) displayed as a function of absolute angular momentum and height at day 20 in the 4x run. Overlaid are two-dimensional streamlines of the daily-averaged secondary circulation (blue). Light green shading denotes $q_l > 0.3$ g kg^{-1}. Dark green shading denotes $q_l > 1$ g kg^{-1}. The inset figure repeats the shadings for q_l, displayed as a function of physical radius. The contours of absolute angular momentum (black) are provided for physical reference for the main figure.

still is superintense ($V_{max} \approx 90$ m s^{-1}). The energy non-conservation of the diffusion scheme may also in part aid superintensity (K. Emanuel, personal communication) and this will be a focus of future research, but the availability of at least one source of high entropy (the ocean beneath the eye) and the resolved scale breakdown of a transverse vortex sheet argue that some aspect of this superintensity mechanism may still be apparent in a variety of situations.

A proof is not known to the authors of whether a non-linear dynamical system prefers to exist in a state that maximizes the rate of entropy production, but Sawada (1981) provides a compelling argument for such a system bounded by two infinite thermal reservoirs. Under different conditions, different dynamical pathways are simply not available, which was used to describe, for example, different crystallization habits or convection modes between plates as states where pathways become available as geometric or thermodynamic constraints are relaxed. Different meteorological systems

have been demonstrated to exist in or relax toward states of maximum entropy or maximum rate of entropy production (e.g., Stephens and O'Brien 1993; O'Brien 1997; Ozawa and Ohmura 1997; Jin and Dubin 1998; Schubert et al. 1999; Schecter et al. 1999; Paltridge 2001; Lorenz et al. 2001). The superintense behavior of the RE87 model at high resolutions may simply be the heat engine existing in a more effective dynamical pathway. What remains as future work is to explain why superintense behavior of axisymmetric hurricane models may be a preferred pathway and to discover the constraints on accessing this pathway.

Sensitivity studies with the horizontal subgrid-scale parameterization in the RE87 model (not shown) indicate that a more diffusive simulation will produce a weaker (yet still superintense) storm. Since the eyewall warming ($\Delta\Theta_e$) observed in these experiments is likewise reduced, we believe the picture presented here is still consistent. Diffusion in the axisymmetric model not only models the effect of turbulence, but more prominently serves as a surrogate for the impact of large scale asymmetries. Barotropic instability (Michalke and Timme 1967; Schubert et al. 1999) naturally results from a ring of convection (an ideal eyewall) due to vortex tube stretching, which would lead to the growth of vortex Rossby waves and eventually non-linear, coherent structures (Kossin and Schubert 2001; Montgomery et al. 2002). The radial structure of axisymmetric mean vorticity in a steady-state three-dimensional storm would be a balance between sources due to convection and losses due to redistribution and friction. In a similar manner the low-level entropy reservoir is a balance between an ocean source and loss to the eyewall (and to a less extent radiation). In a steady-state view, a slower mixing rate (less vigorous waves and mesovortices) allows the entropy reservoir to build to greater levels and potentially allow for more eyewall warming ($\Delta\Theta_e$). In a more realistic, time-varying hurricane, the existence of more vigorous mixing may promote the short-term intensification of the hurricane and a temporary exhaustion of the heat reservoir. What remains as a question for future research is the role of vortex Rossby waves and mesoscale vortices (Montgomery et al. 2002) in the eye in mixing thermodynamic properties and their impact on maximum possible intensity ("MPI").

Many mechanisms have been proposed that would provide a storm intensity that would be weaker than E-MPI. Adverse vertical wind shear disrupts the thermal maximum of the upper-level eye, providing for a weaker central pressure (Gray 1968; DeMaria 1996; Frank and Ritchie 1999, 2001). Secondary eyewalls are found in very intense hurricanes (Willoughby 1998) that interrupt

TABLE 5.4: Comparison of modeled intensities using the RE87 model. (BE98 refers to Bister and Emanuel 1998.)

Experiment	resolution radial	resolution vertical	approx. $\langle V_{max} \rangle$ (m s^{-1})
RE87 control unbounded cooling	1x	1x	46
RE87 Experiment J (2K max cooling)	1x	1x	51
BE98 no dissipational heating	2x	1x	67
BE98 dissipational heating	2x	1x	80
1x run before day 15	1x	1x	55
1x run after day 15	1x	1x	62
2x run	2x	2x	80
4x run	4x	4x	90
4x run ($l_h \times 4$)	4x	4x	65
4x run ($l_h/4$ and $l/4$)	4x	4x	85
4x run (SST = 28C)	4x	4x	102
4x run (SST = 28C. CAPE > 0)	4x	4x	105

the radial inflow of environmental angular momentum (Camp and Montgomery 2001); intensity fluctuations are found with eyewall replacement cycles. DeCosmo et al. (1996) suggest that the ratio of C_k/C_D becomes less than unity at high wind speeds, although Andreas and Emanuel (2001) present an argument that an accounting of the entropy flux due to reentrant sea spray could lead to a positive flux of entropy that nearly cancels the anticipated reduction of V_{max} from changes in C_k/C_D. Drag with the ocean surface generates mixing currents in the ocean that bring cool, deep ocean water to the surface, thus decreasing the effective surface temperature that the hurricane is in contact with (Shay et al. 1998; Bender and Ginis 2000; Jacob et al 2000). In the face of these negative influences on intensity, the hurricane may take advantage of dissipational heating of the boundary layer (Bister and Emanuel 1998; Businger and Businger 2001) as a secondary heat source for the storm. Bister and Emanuel (1998) ran a version of the RE87 model that includes dissipational heating as a forcing term. This showed a 15 m s^{-1} increase in intensity with the inclusion of dissipation heating (Table 5.4). This compares to the 35 m s^{-1} increase due to realization of the eye entropy reservoir. Thus, eyewall heating may be as important or more important to storm intensity as dissipational heating.

5.7 Conclusions

The RE87 hurricane model produces storms that greatly exceed their E-MPI at high spatial and temporal resolution. The cause of "superintensity" is the presence of high-entropy air in the low-level eye, which is entrained to the eyewall and represents a source of latent heat for the eyewall of the storm. Evidence points to the existence of this mechanism in observational data and in three-dimensional numerical models. Because the superintense state is well captured by Eliassen's (1951) balanced vortex model, it is believed that the storm evolves close to a state of gradient and hydrostatic balance. The introduction of heat from the eye leads to a modified Carnot cycle that allows for a stronger storm.

It is proposed that a new MPI may be formulated from first principles that can incorporate this effect, whether as a novel approach to the problem or as a modification of E-MPI. It is proposed that further analysis of the thermodynamic structure of both idealized and realistic simulations of hurricanes be conducted in three-dimensions. Additional observations are needed to document the thermodynamic structure of the low-level eye, especially its potential temporal variability in association with short-period intensity changes, that might allow a full entropy budget of storms. We also propose that the described mechanism can make the hypercane regime described by Emanuel (1988) more accessible with small perturbations of presently observed thermodynamic characteristics of the atmosphere (Knutson and Tuleya 1999).

Chapter 6

CONCLUSIONS

Chapters 2 and 5 have argued for thermodynamic interpretations of hurricane intensification and intensity, respectively. The results of Chapter 4 also appeared to be attracted to solutions anticipated by thermodynamic considerations. On the other hand, Chapters 2 and 4 provide a strong cautionary message in how the details of intensification can be flavored by environmental and numerical considerations, respectively, suggesting that prediction of intensification remains a difficult problem.

While hurricane intensity may be strongly attracted to thermodynamic solutions, the endorsement of E-MPI at this time has to be strongly qualified by the observed capability of idealized, axisymmetric models to exceed E-MPI. A new thermodynamic solution (MPI), that can be applied to both the results of the RE87 model and to reality is desirable. This supposes that the superintensity mechanism is available in three-dimensional geometry. There may be a hint of this in the Opal simulation, showing an association between greater intensification rate and lowered, more intense, and more localized convection in the Hurricane Opal simulation (Figs. 2.20 and 2.2), which is a possible response to an enhanced, localized flux of air from the eye to the eyewall. The case at this point is only suggestive, but it does motivate the effort to extend the superintensity mechanism to reality and reality-based simulations. A proposed line of study to examine this is as follows:

- Examine the superintensity mechanism in high resolution, idealized, three-dimensional hurricane simulations where superintensity is being realized, such as the Frank and Ritchie (2001) simulation. This will be needed to determine what structures produce superintensity in three dimensions and whether the problem is still governed essentially by thermodynamic considerations.

- Given the knowledge of how the superintensity mechanism expresses itself in idealized, three-dimensional models, examine realistic hurricane simulations and observations, where hurricane intensity is generally much less than E-MPI. Reality finds many ways to frustrate hurricane intensity through vertical shear, ocean cooling, secondary eyewalls, etc. (see Section 5.6). Either short-lived expressions of the superintensity mechanism or those confined to only a small azimuthal region may partially act against these negative influences.

- This research then opens up the possibility of coming up with an extension of any proposed superintensity theory as not just a steady-state intensity theory, but to propose a superintensity theory for intensification as well.

Appendix A

A SIMULATION OF A HYPERCANE

The hypercane (introduced by Emanuel 1988; E88) is a hypothesized state for hurricane behavior suggested by the theoretical model where "falling pressure leads to a heat input that is more than sufficient to drive further pressure falls" (E88, p. 1149). Such a hurricane, which has not been observed, would result from this theory if the SST were warm enough and the outflow temperature were cold enough. One simulation is performed (*Hypercane*, see Table 4.3) that satisfies the conditions for a hypercane theorized by E88.[1] The results of this simulation are presented in Figs. A.1 and A.2. The initial smooth contraction of the vortex is finished by day 6, achieving a maximum

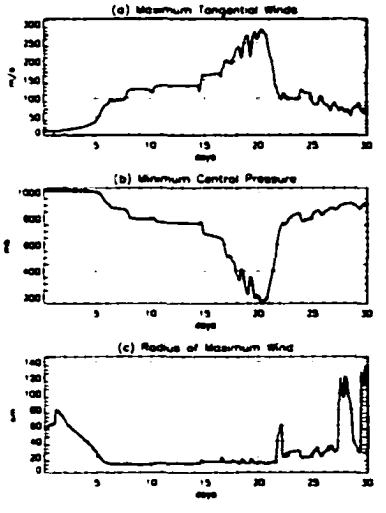

FIGURE A.1: (a) Peak tangential winds, (b) minimum central pressure, and (c) radius of peak winds as a function of time for Simulation *Hypercane*.

tangential wind of 80 m s^{-1} and central pressure of about 860 mb. Between this time and day 15, the storm intensifies through a sequence of three events that are similar to the "anomalies"

[1]The input parameters are the same as those presented for the hypercane in Camp and Montgomery (2001).

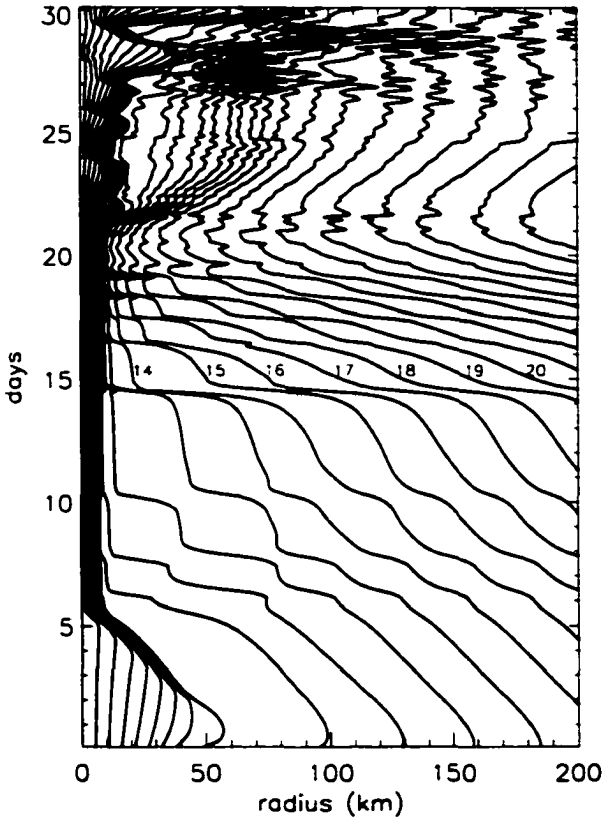

FIGURE A.2: Surface radial positions of each model grid point (R-coordinate, i.e. contours of constant angular momentum) as a function of time for Simulation *Hypercane*. Numbers within the plot label well-spaced grid points by index number, with the zeroth index being the invariant boundary grid point at $r = 0$.

for the smoothly evolving Simulation *Default* (Fig. 4.2) in that a single environmental grid point is newly absorbed into the eyewall bundle. One important distinction is that the environmental grid points far way from the eyewall (for example, grid point 13) continue to contract toward the center of the storm, rather than assuming a constant radius for a finite period. On day 15, multiple environmental grid points are newly absorbed into the eyewall bundle, followed by a sequence of four events similar to smoothly evolving "anomalies", with the same caveat noted above. This sequence of events appears to occur at increasingly shorter intervals of time. After this sequence, the storm has attained up to 270 m s^{-1} tangential winds and about a 210 mb central pressure, which justifies calling this a "hypercane."

Appendix B

INTRODUCTION OF SECONDARY EYEWALLS INTO THE E95A MODEL

As shown in Section 4.3.1, a secondary wind maximum can be realized in the E95 model if two adjacent grid points (outside of the eyewall) are in close proximity to each other (see Eq. 4.1). Table 4.3 lists two experiments performed where a secondary eyewall is imposed during the intensification phase of the simulation, replicating the experiment of Camp and Montgomery (2001). If a secondary eyewall is constructed using pairs of grid points (although the use of three or more grid points is certainly possible) then there are three possible methods for performing the experiment: 1) move the exterior grid point in, 2) move the interior grid point out, or 3) move both grid points to some other radial location (provided that monotonicity of the radii of all grid points is maintained). The first two possibilities are explored here. Note that the angular momentum and circulation of the vortex is only changed locally through this experiment, because each grid point represents a fixed value of angular momentum. If the radial position of any grid point is unchanged, then the tangential wind at that grid point and the circulation interior to that grid point are also unchanged. Moving a grid point out decreases the vorticity in the annulus between that grid point and the next interior grid point, and increases vorticity in the exterior annulus. The opposite occurs when moving a grid point in.

For Simulation *SecEyewall1*, grid point 9 is moved out in a single simulation time step and a secondary eyewall is created at $r = 140$ km. In Simulation *SecEyewall2*, grid point 10 is moved inward in a single time step and a secondary eyewall is created at $r = 112$ km. The adjustments that occur in the tangential wind and vorticity profiles are shown in Fig. B.1. The intensification of the vortex is delayed by the introduction of a secondary eyewall (Fig. B.2) by approximately a day, and the eventual steady-state maximum tangential winds are more intense by about 4 m s^{-1}. The secondary eyewall contracts until convection in the original eyewall is suppressed, and an eyewall replacement occurs. The new eyewall then completes contraction to a radius only slightly exterior

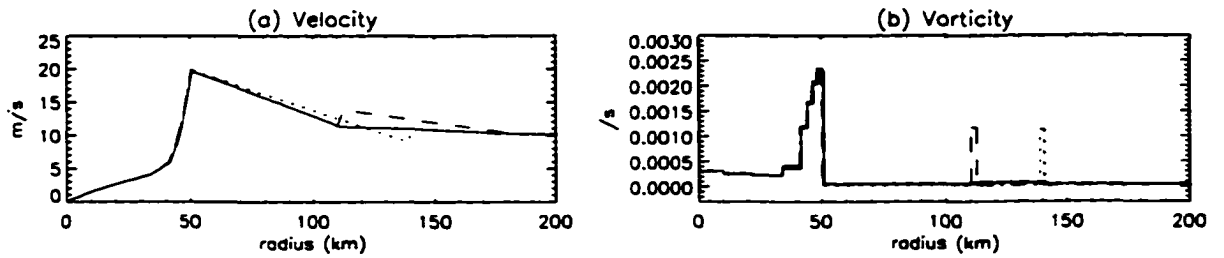

FIGURE B.1: Profiles of (a) tangential wind and (b) vorticity before (solid) and after the introduction of the secondary eyewall in Simulations *SecEyewall1* (dotted) and *SecEyewall2* (dashed).

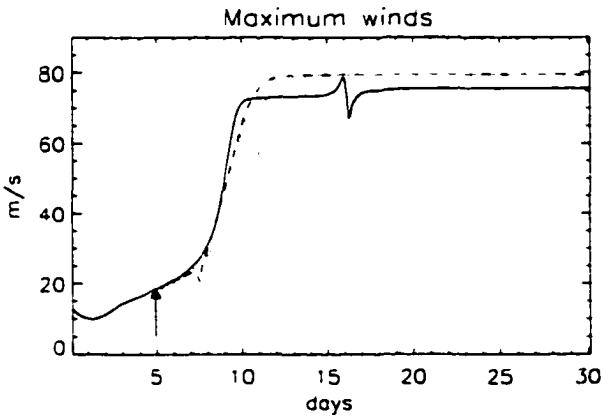

FIGURE B.2: Maximum tangential winds for Simulations *Default* (solid), *SecEyewall1* (dotted), and *SecEyewall2* (dashed). The arrow notes the time of introduction of the secondary eyewalls.

(by 3 km) to the undisturbed Simulation *Default*. A greater amount of angular momentum is now incorporated into the eyewall, yet the eyewall occurs at a very similar radius, thus the maximum winds speeds must increase. The controlling factor is the ultimate radius of the eventual eyewall, since experience has shown that once an important convecting feature occurs within the model at a given grid point, the convection does not "migrate" to another grid point.

Appendix C

AN ASSESSMENT OF THE ASSUMPTIONS AND APPROXIMATIONS OF E-MPI.

This appendix discusses some sensitivities and approximations in E-MPI that can potentially impact the estimate of intensity, but whose sensitivities are generally too small to explain the superintensity shown in high resolution simulations of the RE87 model (see Fig. 5.2).

C.1 Balance of entropy and angular momentum

The accuracy of the combined balance of entropy and angular momentum that is central to E-MPI can be tested by comparing the left and right hand sides of Eq. 11 of E95b (in non-dimensional terms)

$$\frac{1}{2\tilde{R}}\left(\tilde{R}^2 - \tilde{r}_b^2\right)\frac{\partial \tilde{\chi}_b}{\partial \tilde{R}} = -\frac{C_k}{C_D}\left(\tilde{\chi}_s^* - \tilde{\chi}_b\right) \tag{C.1}$$

where R is the potential radius. Each term is within 30% in magnitude of the other in the vicinity of the eyewall, where the vertical gradient term (RHS) is generally of less magnitude because of saturation at the eyewall of the first grid level. Outside the eyewall, the radial gradient term (LHS) nearly vanishes where transfers of low entropy air from the middle levels is the more important loss term.

C.2 Relative humidity

Noted in Sec. 3.2, (3.6) does not satisfy the requirements of an MPI theory since χ_s^* and χ_b cannot be known prior to formation of the storm. E95b provides a closure assumption that $\mathcal{H}$ at the eyewall can be known. For this, E95b needs to assume two things. First, that $\mathcal{H}$ has the same value at the eyewall as in the environment; this assumption permits E95b to derive an expression

for central pressure and RMW. Second, and more relevant to the estimation of V_{max} is that χ_b and χ_s^* can be approximately related to each other by Eq. 15 of E95b (here in dimensional form)

$$\chi_b = \mathcal{H}(\chi_s^* - \chi_{si}^*). \tag{C.2}$$

Implicitly, this equation again makes the first approximation that $\mathcal{H}$ has the same value at the eyewall and the environment, but (C.2) is admittedly approximate (E95b). The relative error incurred by invoking approximation (C.2) to estimate χ_b is about $(1 - \mathcal{H})$, or 20% error at 80% relative humidity. One can track the error through the derivation by augmenting χ_b by a multiplicative constant α with a value near unity (i.e., $\alpha = \mathcal{H}$ or $2 - \mathcal{H}$). The modification of (3.2) appears inside the factor γ^* (3.4), giving

$$\gamma^* = A\frac{1 - \mathcal{H}\alpha}{1 - \mathcal{H}A}. \tag{C.3}$$

The relative error in the estimate of V_{max}^2 is much smaller (4% for $\alpha = 0.8$), for V_{max} smaller still (typical error of 1 m s^{-1} for a 57 m s^{-1} E-MPI and $\alpha = 0.8$). The impact of having radial structure in $\mathcal{H}$ on theory is still an open question.

Another difficulty with applying $\mathcal{H}$ to the numerical model data is that this value strictly speaking does not exist in the RE87 model. What exists in the model is a value of q_v, and thus relative humidity at the first grid level (generally found to be saturated at the eyewall) and an assumption of exchange with a saturated surface layer in contact with the ocean. Then $\mathcal{H}$ should be thought of as the relative humidity just above the surface layer, on the order of several meters. This is just a conceptualization which the bulk aerodynamic formula may or may not recognize. Proceeding with this conceptualization and accepting the observation that the first grid level under the eyewall is saturated, then as resolution is increased, the saturated first grid level approaches the sea surface. If a well-mixed boundary layer is assumed, the value of $\mathcal{H}$ would become more saturated, which would provide for a slower estimate of V_{max} using (3.2), which is contrary to the observed behavior of the model with increasing resolution. For all of these reasons, examination of (3.6) is more robust for comparison with model output, rather than (3.2).

C.3 Boundary layer height

According to E95a, the top of the boundary layer is the proper reference for evaluating χ_b. In this paper, when χ_b has been evaluated, it has been at the first grid level, the level of saturation

at the eyewall. At low spatial resolution (the default run), this level ($z = 625$ m) is also saturated in the near environment of the eyewall extending to $r \sim 80$ km, except where downdrafts are occurring. As resolution is increased, the level of saturation in the near environment is generally found at $z = 400$ m. Selecting this level in computation of χ_b leads to only a small increase in estimating V_{max} using (3.6) at higher resolutions (4x and 8x runs) of 5 to 10 m s^{-1}, which is insufficient to explain the observed degree of superintensity.

C.4 Gradient wind balance

While the sensitivity of E-MPI to violation of gradient wind approximation is difficult to track through the theory, we can test the degree to which these model runs conform to gradient wind balance

$$V_{\text{gradient}} = -\frac{fr}{2} + \left(\frac{f^2 r^2}{4} + \frac{r}{\rho} \frac{\partial p}{\partial r} \right)^{1/2} \tag{C.4}$$

by testing

$$\frac{V_{\text{model}} - V_{\text{gradient}}}{V_{\text{model}}} \tag{C.5}$$

from the model output (Fig. C.1). Model winds are slow in the planetary boundary layer by about 15% and too strong in the updraft by the same amount. Slowing of the winds in the boundary layer can be anticipated from local force balance considerations. Willoughby (1990) shows a slight tendency for supergradient winds at flight-level (850 mb) of more intense storms. Elsewhere Willoughby (1990) found flight-level winds show no bias relative to gradient winds in many storms. These magnitudes of the relative "errors" (Fig. C.1d) are approximately the same in the default run (not shown) and the 4x run and therefore gradient wind imbalance cannot be invoked to explain the emergence of superintensity at higher resolution. Further, these results are in general agreement with a small degree of supergradient winds found in Shapiro (1983). See Section 5.6 for more.

C.5 Thermal wind balance

One intriguing aspect of the E95b derivation of E-MPI is the origin of the "thermal wind" equation (valid at the top of the boundary layer, and by the moist neutral assumption through

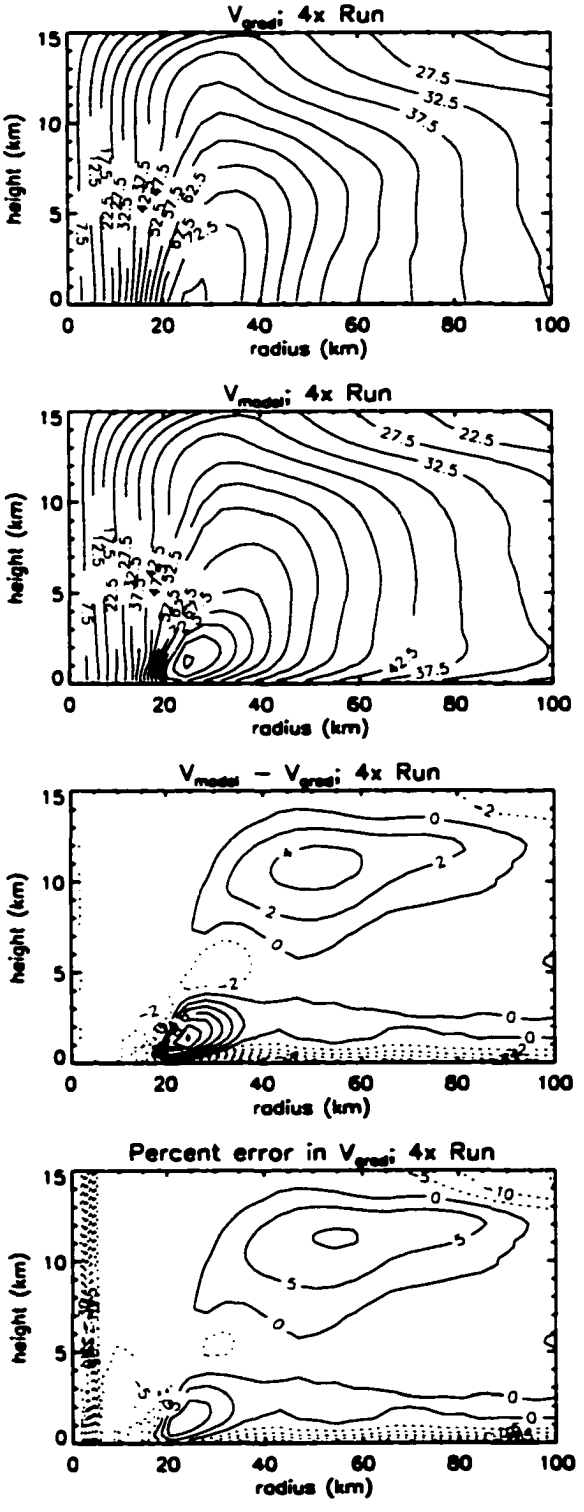

FIGURE C.1: The gradient wind, the model tangential wind, the difference between the two, and the relative error (m s^{-1}) averaged from the last 15 days of the 4x run.

all the troposphere except the boundary layer), repeated here as in E95b in non-dimensional form (using tildes to denote non-dimensional quantities)

$$\frac{1}{\tilde{r}_b^2} = -\frac{2}{\tilde{R}^3}\frac{\partial \tilde{\chi}_b}{\partial \tilde{R}}. \tag{C.6}$$

At one point in the derivation it becomes necessary to assume that the eyewall and the near environment is neutral to moist ascent along surfaces of constant absolute angular momentum M and that rising parcels travel along such M-surfaces. A consequence of this assumption is that the moist entropy is constant on M-surfaces. If the atmosphere in this area is under persistent saturated ascent, as in a hurricane, then saturated entropy s^* is also constant on M-surfaces above the boundary layer (assumed to be the same as the lifted condensation level). Because of this, the thermal structure of the atmosphere can simply be described as a function of M, which is the key to interpreting (C.6) as a thermal wind relationship. Under these assumptions, the derivative $\partial s^*/\partial M)_p$ is a simple function of M and is independent of height since s^* has a one-to-one relationship to M. An integral dp along M-surfaces is then performed to collapse the vertical structure of the atmosphere and to describe the troposphere in terms of quantities at the boundary-layer top, a guiding philosophy of E-MPI. Under the moist neutral assumption, when this integral is taken, $\partial s^*/\partial M$ is simply a constant that comes out of the integral.

We can relax the moist neutral assumption in one specific way such that (C.6) would still be valid (subject to other assumptions of the derivation like gradient wind balance, hydrostatic balance, and active convection, for example). Specifically we can relax the assumption that $\partial s^*/\partial M)_p$ is a constant along M-surfaces, which would permit some moist static stability so long as that stabilization has more or less the same vertical structure on different M-surfaces.

Relaxing the assumption that $\partial s^*/\partial M)_p$ is constant along M-surfaces, the problem then becomes: to what degree does

$$\frac{\partial s_b^*}{\partial M}\Big)_p \tag{C.7}$$

approximate the average

$$\left\langle \frac{\partial s^*}{\partial M}\Big)_p \right\rangle \equiv \frac{1}{p_{out} - p_b}\int_{p_b}^{p_{out}} \frac{\partial s^*}{\partial M}\Big)_p dp \tag{C.8}$$

using path integrals along an M-surface to define a tropospheric average. Estimating the error in using (C.7) with a multiplicative factor α_1 (where $\alpha_1 = 1$ would imply no error)

$$\left\langle \frac{\partial s^*}{\partial M}\Big)_p \right\rangle = \alpha_1 \frac{\partial s_b^*}{\partial M}\Big)_p \tag{C.9}$$

where brackets denote the average defined above. This error then modifies the thermal wind relation (C.6) as follows:

$$\frac{1}{r_b^2} = \frac{-2\alpha_1}{R^3}\frac{\partial \chi_b^*}{\partial R} \tag{C.10}$$

which can be carried through to modify the boundary layer balance estimate of V_{max} (3.6) to become

$$V_{max}^2 = \alpha_1 \frac{C_k}{C_D}(\chi_s^* - \chi_b)\,. \tag{C.11}$$

The dependence of V_{max} on the magnitude of this error then becomes significantly reduced because of the square root dependence of V_{max} on α_1. Motivated by the presence of a low-level entropy enhancement (like Fig. 5.17 where Θ_e^* strongly tracks Θ_e) that visibly distorts the radial gradient of saturated entropy above that found at PBL top, we computed α_1 for many cases but never found this value to greatly exceed 1.1.

Thus, although the approximations used in deriving (C.6) can be somewhat relaxed with values found in our model runs, they are incapable of explaining superintensity.

C.6 Outflow temperature

From (C.8), it is clear that the meaning of T_{out} should be at the end point of the integral defined above. This would appear to permit different values of T_{out} as a function of radius. Also T_{out} would be defined at a point, rather than as an average as defined by (5.10), and would be generally colder than (5.10). There is no reason to anticipate that this definition of T_{out} would be greatly different than that defined by (5.11), used elsewhere in this paper. In any case, no value of T_{out} supplied into E-MPI theory can explain the degree of superintensity observed in our model runs since (3.2) breaks down as $T_{out} \to 0$ K.

REFERENCES

AMS Council, 2000: Policy statement: Hurricane research and forecasting. *Bull. Amer. Meteor. Soc.*, **81**, 1341–1346.

Andreas, E. L., and K. A. Emanuel, 2001: Effects of sea spray on tropical cyclone intensity. *J. Atmos. Sci.*, **58**, 3741–3751.

Bender, M. A., 1997: The effect of relative flow on the asymmetric structure in the interior of hurricanes. *J. Atmos. Sci.*, **54**, 703–724.

Bender, M. A., and I. Ginis, 2000: Real-case simulations of hurricane-ocean interaction using a high-resolution coupled model: effects on hurricane intensity. *Mon. Wea. Rev.*, **128**, 917–946.

Bengtsson, L., 2001: Hurricane threats. *Science*, **293**, 440–441.

Bister, M., and K. A. Emanuel, 1998: Dissipative heating and hurricane intensity. *Meteorol. Atmos. Phys.* , **65** , 233–240.

Black, M. L., and J. L. Franklin, 2000: GPS dropsonde observations of the wind structure in convective and non-convective regions of the hurricane eyewall. Preprints. *24th Conf. on Hurricanes and Trop. Meteorology*, 448–449.

Bluestein, H. B., J. G. Ladue, H. Stein, D. Speheger, and W. P. Unruh, 1993: Doppler radar wind spectra of supercell tornadoes. *Mon. Wea. Rev.*, **121**, 2200–2221.

Bosart, L., and J. Bartlo, 1991: Tropical storm formation in a baroclinic environment. *Mon. Wea. Rev.*, **119**, 1979–2013.

Bosart, L. F., C. S. Velden, W. E. Bracken, J. Molinari, and P. G. Black, 2000: Environmental influences on the rapid intensification of Hurricane Opal (1995) over the Gulf of Mexico. *Mon. Wea. Rev.*, **128**, 322–352.

Braun, S. A., 2002: A cloud-resolving simulation of Hurricane Bob (1991): Storm structure and eyewall buoyancy. *Mon. Wea. Rev.*, **??**, submitted.

Braun, S. A., and W.-K. Tao, 2000: Sensitivity of high-resolution simulations of Hurricane Bob (1991) to planetary boundary layer parameterizations. *Mon. Wea. Rev.*, in press.

Businger, S., and J. A. Businger, 2001: Viscous dissipation of turbulent kinetic energy in storms. *J. Atmos. Sci.*, **58**, 3793–3796.

Camp, J. P., 1999: *Hurricane Maximum Intensity: Past and Present.* M. Sc. Thesis. Colorado State University. 147 pp.

Camp, J. P., and M. T. Montgomery, 2001: Hurricane maximum intensity: Past and present. *Mon. Wea. Rev.*, **129**, 1704–1717.

Carr, L. E. III, and R. T. Williams, 1989: Barotropic vortex stability to perturbations from axisymmetry. *J. Atmos. Sci.*, **46**, 3177-3191.

Challa, M., and R. L. Pfeffer, 1990: Formation of Atlantic hurricanes from cloud clusters and depressions. *J. Atmos. Sci.*, **47**, 909–927.

Charney, J. G., 1948: On the scale of atmospheric motions. *Geophys. Publ.*, **17**, 1–17.

Charney, J. G., 1962: Integration of the primitive and balance equations. *Proc. Int. Symp. Numerical Weather Prediction*, Tokyo, Meteor. Soc. Japan, 131–152.

Chen, Y., and M. K. Yau, 2001: Spiral bands in a simulated hurricane. Part I: Vortex Rossby wave verification. *J. Atmos. Sci.*, **58**, 2128–2145.

DeCosmo, J., K. B. Katsaros, S. D. Smith, R. J. Anderson, W. A. Oost, K. Bumke, and H. Chadwick, 1996: Air-sea exchange of water vapor and sensible heat: The humidity exchange over the sea (HEXOS) results. *J. Geophys. Res.*, **101**, 12 001–12 016.

DeMaria, M., 1996: The effect of vertical shear on tropical cyclone intensity change. *J. Atmos. Sci.*, **53**, 2076–2087.

DeMaria, M., and J. Kaplan, 1994a: Sea surface temperature and the maximum intensity of Atlantic tropical cyclones. *J. Climate*, **7**, 1324–1334.

DeMaria, M. and J. Kaplan, 1994b: A statistical hurricane intensity prediction scheme (SHIPS) for the Atlantic basin. *Wea. Forecasting*, **9**, 209–220.

DeMaria, M. and J. Kaplan, 1999: An updated statistical hurricane intensity prediction scheme (SHIPS) for the Atlantic and Easter Pacific Basins. *Weather and Forecasting*, **14**, 326–337.

Eliassen, A., 1951: Slow thermally or frictionally controlled meridional circulation in a circular vortex. *Astrophys. Norv.*, **5**, 19–60.

Emanuel, K. A., 1986: An air-sea interaction theory for tropical cyclones. Part I: Steady-state maintenance. *J. Atmos. Sci.*, **43**, 585–604.

Emanuel, K. A., 1988: The maximum intensity of hurricanes. *J. Atmos. Sci.*, **45**, 1143–1155.

Emanuel, K. A., 1989: The finite-amplitude nature of tropical cyclogenesis. *J. Atmos. Sci.*, **46**, 3431–3456.

Emanuel, K. A., 1995a: The behavior of a simple hurricane model using a convective scheme based on subcloud-layer entropy equilibrium. *J. Atmos. Sci.*, **52**, 3960–3968.

Emanuel, K. A., 1995b: Sensitivity of tropical cyclones to surface exchange coefficients and a revised steady-state model incorporating eye dynamics. *J. Atmos. Sci.*, **52**, 3969–3976.

Emanuel, K. A., 1997: Some aspects of hurricane inner-core dynamics and energetics. *J. Atmos. Sci.*, **54**, 1014–1026.

Emanuel, K. A., 1999: Thermodynamic control of hurricane intensity. *Nature*, **401**, 665–669.

Emanuel, K. A., 2000: A statistical analysis of tropical cyclone intensity. *Mon. Wea. Rev.*, **128**, 1139–1152.

Emanuel, K. A., M. Fantini, and A. J. Thorpe, 1987: Baroclinic instability in an environment of small stability to slantwise moist convection. Part I: Two-dimensional models. *J. Atmos. Sci.*, **44**, 1559–1573.

Fairall, C. W., J. D. Kepert, and G. J. Holland, 1994: The effect of sea spray on surface energy transports over the ocean. *Global Atmos. Ocean Syst.*, **2**, 121–142.

Fiedler, B. H., 1994: The thermodynamic speed limit and its violation in axisymmetric numerical simulations of tornado-like vortices. *Atmos.-Ocean*, **32**, 335–359.

Fiedler, B. H., 1998: Wind-speed limits in numerically simulated tornadoes with suction vortices. *Quart. J. Roy. Meteor. Soc.*, **124**, 2377–2392.

Fiedler, B. H., and R. Rotunno, 1986: A theory for the maximum windspeeds in tornado-like vortices. *J. Atmos. Sci.*, **43**, 2328–2340.

Frank, W. M., and E. A. Ritchie, 1999: Effect of environmental flow upon tropical cyclone structure. *Mon. Wea. Rev.*, **127**, 2044–2061.

Frank, W. M., and E. A. Ritchie, 2001: Effects of vertical wind shear on the intensity and structure of numerically simulation hurricanes. *Mon. Wea. Rev.*, **129**, 2249–2269.

Frankin, J. L., M. L. Black, and K. Valde, 2000: Eyewall wind profiles in hurricanes determined by GPS dropwindsondes. Preprint. *24th Conf. on Hurricanes and Tropical Meteorology*, 446–447.

Fulton, J. D., 2001: *Insights into the Hurricane Vortex Using a High Resolution Numeric an Simulation of Hurricane Bob (1991).* M. S. Thesis. Colorado State University, 84 pp.

Fujita, T. T., 1971: Proposed mechanism for suction spots accompanied by tornadoes. *Preprints 7th Conf. Severe Local Storms*, Kansas City, Amer. Meteor. Soc., 208–213.

Gray, W. M., 1968: Global view of the origin of tropical disturbances and storms. *Mon. Wea. Rev.*, **96**, 669–700.

Halliday, D., and R. Resnick, 1988: *Fundamentals of Physics.* 3rd Ed. John Wiley & Sons, 977 pp.

Hausman, S. A., 2001: Formulation and sensitivity analysis of a nonhydrostatic, axisymmetric tropical cyclone model. Atmospheric Science Paper No. 701, Dept. of Atmospheric Science, Colorado State University, 210 pp.

Heisler, H., 1995: *Advanced Engine Technology.* Arnold, 794 pp.

Holland, G. J., 1997: The maximum potential intensity of tropical cyclones. *J. Atmos. Sci.*, **54**, 2519–2541.

Holton, J. R. , 1992: *An Introduction to Dynamic Meteorology. Third Edition.* Academic Press. 511 pp.

Hoskins, B. J., and F. P. Bretherton, 1972: Atmospheric frontogenesis models: Mathematical formulation and solution. *J. Atmos. Sci.*, **29**, 11–37.

Jacob, S. D., L. K. Shay, A. J. Mariano, and P. G. Black, 2000: The 3D oceanic mixed layer response to Hurricane Gilbert. *J. Phys. Ocean.*, **30**, 1407–1429.

Jin, D. Z., and D. H. E. Dubin, 1998: Regional maximum entropy theory for vortex crystal formation. *Phys. Rev. Lett.*, **80**, 4434–4437.

Jones, S. C., 1995: The evolution of vortices in vertical shear. Part I: Initially barotropic vorticies. *Quart. J. Roy. Meteor. Soc.*, **121**, 2760–2780.

Jordan, C. L., 1958: Mean soundings for the West Indies area. *J. Meteor.*, **15**, 91–97.

Kleinschmidt, E., 1951: Grundlagen einer Theorie der Tropischen Zyklonen (Basic principles for a theory of tropical cyclones.) *Arch. Meteorol. Geophys. Bioklimatol.*,, **A4**, 53–72.

Klemp, J. B., and R. B. Wilhelmson, 1978: The simulation of three-dimensional convective storm dynamics. *J. Atmos. Sci.*, **35**, 1070–1096.

Knutson, T. R., and R. E. Tuleya, 1999: Increase hurricane intensities with CO_2-induced warming as simulated using the GFDL hurricane prediction system. *Climate Dyn.*, **15**, 503–519.

Kossin, J. P., and M. D. Eastin, 2001: Two distinct regimes in the kinematic and thermodynamic structure of the hurricane eye and eyewall. *J. Atmos. Sci.*, **58**, 1079–1090.

Kossin, J. P., and W. H. Schubert, 2001: Mesovortices, polygonal flow patterns, and rapid pressure falls in hurricane-like vortices. *J. Atmos. Sci.*, **58**, 2196–2209.

Krishnamurti, T. N., W. Han, B. Jha, and H. S. Bedi, 1998: Numerical prediction of Hurricane Opal. *Mon. Wea. Rev.*, **126**, 1347-1363.

Kurihara, Y., and R. E. Tuleya, 1974: Structure of a tropical cyclone developed in a three-dimensional numerical simulation model. *J. Atmos. Sci.*, **31**, 893–919.

Kurihara, Y., M. A. Bender, and R. J. Ross, 1993: An initialization scheme of hurricane models by vortex specification. *Mon. Wea. Rev.*, **121**, 2030–2045.

Kurihara, Y., M. A. Bender, R. E. Tuleya, and R. J. Ross, 1995: Improvements in the GFDL hurricane prediction system. *Mon. Wea. Rev.*, **123**, 2791–2801.

Kurihara, Y., R. E. Tuleya, and M. A. Bender, 1998: The GFDL hurricane prediction system and it performance in the 1995 hurricane season. *Mon. Wea. Rev.*, **126**, 1306–1322.

Landsea, C. W., 1993: A climatology of intense (or major) Atlantic hurricanes. *Mon. Wea. Rev.*, **121**, 1703–1713.

LeeJoice, R. N., 2000: Hurricane inner-core structure as revealed by GPS dropwindsondes. M. S. Thesis, Colorado State University, 56 pp.

Leith, C. E., 1980: Nonlinear normal mode initialization and quasi-geostrophic theory. *J. Atmos. Sci.*, **37**, 958–968.

Lilly, D. K., 1962: On the numerical simulation of buoyant convection. *Tellus,*, **14,** 148–172.

Liu, Y., D.-L. Zhang, M. K. Yau, 1997: A multiscale numerical study of Hurricane Andrew (1992). Part I. Explicit simulation and verification. *Mon. Wea. Rev.*, **125**, 3073–3093.

Liu, Y., D.-L. Zhang, M. K. Yau, 1999: A multiscale numerical study of Hurricane Andrew (1992). Part II. Kinematics and inner-core structure. *Mon. Wea. Rev.*, **127**, 2597–1616.

Lorenz, E. N., 1960: Energy and numerical weather prediction. *Tellus*, **12,** 364–373.

Lorenz, R. D., J. I. Lunine, P. G. Withers, and C. P. McKay, 2001: Titan, Mars and Earth: Entropy production by latitudinal heat transport. *Geophys. Res. Lett.*, **28,** 415–418.

Marks, F. D., L. K. Shay, and the Fifth Prospectus Development Team, 1998: Landfalling tropical cyclones: Forecast problems and associated research opportunities. *Bull. Amer. Met. Soc.*, **79**, 305–323.

Merrill, R. T., 1988: Environmental influences on hurricane intensification. *J. Atmos. Sci.*, **45**, 1678–1687.

Michalke, A., and A. Timme, 1967: On the inviscid instability of certain two-dimensional vortex-type flows. *J. Fluid Mech.*, **29**, 647-666.

Miller, B. I., 1958: On the maximum intensity of hurricanes. *J. Met.*,, **15,** 184–195.

Möller, J. D., and S. C. Jones, 1998: Potential vorticity inversion for tropical cyclones using the asymmetric balance theory. *J. Atmos. Sci.*, **55**, 259–282.

Möller, J. D., and L. S. Shapiro, 2002: Balanced contributions to the intensification of Hurricane Opal as diagnosed from a GFDL model forecast. *Mon. Wea. Rev.*, , in press.

Molinari, J. and D. Vollaro, 1989: External influences on hurricane intensity. Part I: Outflow layer eddy angular momentum fluxes. *J. Atmos. Sci.*, **46**, 1093–1105.

Molinari, J. and D. Vollaro, 1990: External influences on hurricane intensity. Part II: Vertical structure and response of the hurricane vortex. *J. Atmos. Sci.*, **47**, 1902–1918.

Molinari, J., S. Skubis, D. Vollaro, F. Alsheimer, and H. E. Willoughby, 1998: Potential vorticity analysis of tropical cyclone intensification. *J. Atmos. Sci.*, **55**, 2632–2644.

Montgomery, M. T., and B. Farrell, 1993: Tropical cyclone formation. *J. Atmos. Sci.*, **50**, 285–310.

Montgomery, M. T., and J. Enagonio, 1998: Tropical cyclogenesis via convectively forced vortex Rossby waves in a three-dimensional quasigeostrophic model. *J. Atmos. Sci.*, **55**, 3176–3207.

Montgomery, M. T., and R. J. Kallenbach, 1997: A theory for vortex Rossby waves and its application to spiral bands and intensity changes in hurricanes. *Quart. J. Roy. Meteor. Soc.*, **123**, 435–465.

Montgomery, M. T., V. A. Vladimirov, and P. V. Denissenko, 2002: An experimental study on hurricane mesovortices. *J. Fluid Mech.*, accepted.

O'Brien, D. M., 1997: A yardstick for global entropy-flux. *Quart. J. Roy. Meteor. Soc.*, **123**, 243–260.

Ooyama, K., 1969: Numerical simulation of the life cycle of tropical cyclones. *J. Atmos. Sci.*, **26**, 3–39.

Ooyama, K. V., 2001: A dynamic and thermodynamic foundation for modeling the moist atmosphere with parameterized microphysics. *J. Atmos. Sci.*, **58**, 2073–2102.

Ozawa, A., and H. Ohmura, 1997: Thermodynamics of a global-mean state of the atmosphere: A state of maximum entropy increase. *J. Climate*, **10**, 441-445.

Paltridge, G. W., 2001. A physical basis for a maximum thermodynamic dissipation of the climate system. *Quart. J. Roy. Meteor. Soc.*, **572**, 305–314.

Persing, J., M. T. Montgomery, and R. E. Tuleya, 2002: Environmental interactions in the GFDL hurricane model for Hurricane Opal. *Mon. Wea. Rev.*, **130**, 298–317.

Reasor, P. D., M. T. Montgomery, F. D. Marks, and J. F. Gamache, 2000: Low-wavenumber structure and evolution of the hurricane inner core observed by airborne dual-doppler radar. *Mon. Wea. Rev.*, **128**, 1653–1680.

Roll, H. V., 1965: *Physics of the Marine Atmosphere*. Academic Press, 426 pp.

Rotunno, R., and K. A. Emanuel, 1987: An air-sea interaction theory for tropical cyclones. Part II: Evolutionary study using a nonhydrostatic axisymmetric numerical model. *J. Atmos. Sci.*, **44**, 542–561.

Sawada, Y., 1981: A thermodynamic variational principle in nonlinear non-equilibrium phenomena. *Prog. Theor. Phys.*, **66**, 68–76.

Schade, L. R., and K. A. Emanuel, 1999: The ocean's effect on the intensity of tropical cyclones: Results from a simple coupled atmosphere-ocean model. *J. Atmos. Sci.*, **56**, 642–651.

Schecter, D. A., D. H. E. Dubin, K. S. Fine, and C. F. Driscoll, 1999: Vortex crystals from 2D Euler flow: Experiment and simulation. *Phys. Fluids*, **11**, 905–914.

Schubert, W. H., S. A. Hausman, M. Garcia, K. V. Ooyama, and H.-C. Kuo, 2001: Potential vorticity in a moist atmosphere. *J. Atmos. Sci.*, **58**, 3148–3157.

Schubert, W. H., M. T. Montgomery, R. K. Taft, T. A. Guinn, S. R. Fulton, J. P. Kossin, and J. P. Edwards, 1999: Polygonal eyewalls, asymmetric eye contraction, and potential vorticity mixing in hurricanes. *J. Atmos. Sci.*, **56**, 1197–1223.

Shapiro, L. J., 1983: The asymmetric boundary layer flow under a translating hurricane. *J. Atmos. Sci.*, **40**, 1984–1998.

Shapiro, L. J., and M. T. Montgomery, 1993: A three-dimensional balance theory for rapidly rotating vortices. *J. Atmos. Sci.*, **50**, 3322–3335.

Shapiro, L. J., and H. E. Willoughby, 1982: The response of balanced hurricanes to local sources of heat and momentum. *J. Atmos. Sci.*, **39**, 378–394.

Shay, L. K., A. J. Mariano, S. D. Jacob, and E. H. Ryan, 1998: Mean and near-inertial ocean current response to Hurricane Gilbert. *J. Phys. Ocean.*, **28**, 858–889.

Simpson, R. H., 1952: Exploring eye of Typhoon "Marge," 1951. *Bull. Amer. Meteo. Soc.*, **33**, 286–198.

Smagorinsky, J., 1963: General circulation experiments with the primitive equations. I: The basic experiment. *Mon. Wea. Rev.*, **91**, 99–164.

Stephens, G. L., and D. M. O'Brien, 1993: Entropy and climate. I: ERBE observations of the entropy production of the earth. *Quart. J. Roy. Meteor. Soc.*, **119**, 121–152.

Titley, D. W., and R. L. Elsberry, 1999: Rapid intensification of tropical cyclones: A case study of Supertyphoon Flo during TCM-90. Preprints. *23rd Conf. on Hurricanes and Trop. Meteorology*, **2**, 588–591.

Wang, Y., 2002a: Vortex Rossby waves in a numerically simulated tropical cyclone. Part I: Overall structure, potential vorticity, and kinetic energy budgets. *J. Atmos. Sci.*, in press.

Wang, Y., 2002b: Vortex Rossby waves in a numerically simulated tropical cyclone. Part II: The role in tropical cyclone structure and intensity changes. *J. Atmos. Sci.*, in press.

Willoughby, H. E., 1979: Forced secondary circulations in hurricane. *J. Geophys. Res.*, **84**, 3173–3183.

Willoughby, H. E., 1990: Gradient balance in tropical cyclones. *J. Atmos. Sci.*, **47**, 265–274.

Willoughby, H. E., 1998: Tropical cyclone eye thermodynamics. *Mon. Wea. Rev.*, **126**, 1653–1680.

Wu, C.-C., and H.-J. Cheng, 1999: An observational study of environmental influences on the intensity changes of Typhoons Flo (1990) and Gene (1990). *Mon. Wea. Rev.*, **127**, 3003–3031.

Zhang, D.-L., Y. Liu, and M. K. Yau, 2000: A multiscale numerical study of Hurricane Andrew (1992). Part III: Dynamically induced vertical motion. *Mon. Wea. Rev.*, **128**, 3772–3788.